Detection of Inter-turn Winding Fault in Single-phase Transformers Using a Terminal Measurement Based Modeling Technique

By

Shantanav Bhowmick

B. Tech., West Bengal University of Technology, India – 2010

A Thesis Submitted in Partial Fulfillment of the Requirements for the Degree of

MASTER OF APPLIED SCIENCE

In the Department of Electrical and Computer Engineering

University of Victoria

Supervisory Committee

Detection of Inter-turn Winding Fault in Single-phase Transformers Using a Terminal Measurement Based Modeling Technique

By

Shantanav Bhowmick

B. Tech., West Bengal University of Technology, India – 2010

Supervisory Committee

Dr. Subhasis Nandi

Supervisor (Department of Electrical and Computer Engineering)

Dr. A. K. S. Bhat

Department Member (Department of Electrical and Computer Engineering)

Abstract

Supervisory Committee

Dr. Subhasis Nandi

Supervisor (Department of Electrical and Computer Engineering)

Dr. A. K. S. Bhat

Department Member (Department of Electrical and Computer Engineering)

Transformers form a very important part of the power transmissions and distribution network; as they are responsible for the transfer of electrical energy from the power generation sites onto the transmission lines and finally to the distribution stage. Dry-type and oil-filled single-phase transformers, either alone or as a part of three-phase banks, are used extensively in the power distribution network, ultimately providing power to the domestic consumers. Any faults in the single-phase transformers leading to power outages or catastrophic power systems failures cause huge loss of capital, property and in some cases even human casualties. Gradual deterioration of the electrical winding insulation ultimately leads to inter-turn winding short circuit faults; which account for a significant proportion of all transformer failures. Incipient stages of inter-turn winding faults have negligible impact on the terminal voltages and currents of transformers; thus these faults often go undetected by the traditional differential relay based protection mechanisms. By the time, the faults manifest themselves into severe winding short-circuit faults consequently forcing the differential relays to operate for tripping the circuit breakers; a significant part of the transformer windings and core may get extensively damaged. Over the years, various techniques have been developed for detecting and studying inter-turn winding faults; however their practical implementation involves quite a few challenges such as high cost, lack of reliability, low

accuracy and need for mounting additional equipment inside the transformer casing. Additionally, none of the existing techniques are suitable for online and real-time condition monitoring of the transformers. This absence of any proven technique to detect incipient levels of inter-turn winding faults in single-phase transformers has motivated the research of this thesis.

In the thesis, firstly, a non-invasive technique for modeling single-phase transformers has been developed which is based solely on the terminal measurements of voltages and currents. The effects of transformer core saturation, non-linearity, hysteresis are incorporated in the model by considering a time-varying magnetizing inductance comprising of any desired number of harmonic components. The coefficients of the magnetizing inductance are computed from the instantaneous values of flux linkage and magnetizing current over one complete cycle. The model is found to replicate the behaviour of the single-phase transformer with an extremely high level of accuracy, under any load conditions for healthy as well as faulty operations. Detailed simulation and experiment based studies have been performed for corroborating the effectiveness of the proposed terminal measurement based modeling technique not only in detecting incipient stages of inter-turn winding faults (involving less than 1% of the turns) but also in estimating fault severity.

Also, a non-invasive, online and real-time implementation of the proposed inter-turn winding fault detection technique for continuous monitoring of the transformer health has been suggested. Firstly, with the experimentally acquired primary line voltage and line current data of the healthy transformer, a healthy no-load model of the transformer is generated. Next, a healthy estimated indicator value, computed from this model under the given input voltage condition, is compared with the actual indicator value for detecting the presence of an inter-turn winding fault. It involves minimum hardware (only two current sensors and one voltage sensor), low memory requirements and low computational complexity and thus holds a good promise for practical applications. Further discussion is made on the possible challenges for realizing the proposed fault diagnostic technique in the industry and suitable recommendations have been made for further improvement.

Table of Contents

List of Tables

List of Figures

List of Abbreviations

AC	Alternating Current
ANN	Artificial Neural Network
CAD	Computer Aided Design
CI	Confidence Interval
DC	Direct Current
DGA	Dissolved Gas Analysis
FEM	Finite Element Model
FFT	Fast Fourier Transform
FRA	Frequency Response Analysis
HBM	Harmonic Balance Method
HF	High Frequency
MMF	Magneto Motive Force
PF	Power Factor
PWM	Pulse Width Modulation
RIFL	Ratio of Increment of Flux Linkage
RMS	Root Mean Square
RTHPC	Real-Time High Performance Computing
SMPS	Switched Mode Power Supply
SPICE	Simulation Program with Integrated Circuit Emphasis
STC	Saturable Transformer Component
THD	Total Harmonic Distortion

List of Symbols

A	Cross-sectional area
C_L	Load capacitance
D_1 , D_2	Difference terms for fault detection
f	Frequency
h	Harmonic number
i_C	Core loss current of single-phase transformer
i_D	D-axis component of Park's Vector
i_E	Exciting current of single-phase transformer
$(I_E)_1$, $(I_E)_2$	
$(I_E)_3$ …	RMS values of harmonic components of exciting current
i_F	Current in the short-circuited faulty winding
i_L	Primary line current of single-phase transformer
i_{L1} , i_{L2} , i_{L3}	Primary line currents of three-phase transformer
i_{L4} , i_{L5} , i_{L6}	Secondary line currents of three-phase transformer
i_M	Magnetizing current of single-phase transformer
$(i_M)_1$	Fundamental component of magnetizing current of single-phase transformer under healthy state
$[\,(i_M)_1]_{fS}$	Fundamental component of magnetizing current of single-phase transformer under inter-turn winding fault on secondary side
$[\,(i_M)_1]_{fP}$	Fundamental component of magnetizing current of single-phase

	transformer under inter-turn winding fault on primary side
I_{MAX}	Peak value of rated input current
i_P	Primary winding current of single-phase transformer
i_{P1} , i_{P2} , i_{P3}	Primary phase currents of three-phase transformer
i_{PX}	Current in healthy part of primary winding of single-phase transformer
i_Q	Q-axis component of Park's Vector
i_S	Secondary winding current of single-phase transformer
i_{SX}	Current in healthy part of secondary winding of single-phase transformer
K	Fault indicator
K_H	Fault indicator value under healthy operation
$(K_H)_{mean}$	Average of the fault indicator values under healthy operation
K_F	Fault indicator value under faulty operation
$(K_F)_{mean}$	Average of the fault indicator values under faulty operation
L_L	Load inductance
L_{lF}	Leakage inductance of short-circuited faulty winding
L_{lP}	Leakage inductance of primary winding
L_{lPX}	Leakage inductance of healthy part of primary winding
L_{lS}	Leakage inductance of secondary winding
L_{lSX}	Leakage inductance of healthy part of secondary winding
L_{MF}	Magnetizing inductance corresponding to short-circuited faulty winding
L_{MP}	Magnetizing inductance corresponding to primary winding
$(L_{MP})_0$, $(L_{MP})_2$, $(L_{MP})_4$, $(L_{MP})_6$ …	Coefficients of primary side's magnetizing inductance

L_{MPX}	Magnetizing inductance corresponding to healthy part of primary winding
L_{MS}	Magnetizing inductance corresponding to secondary winding
L_{MSX}	Magnetizing inductance corresponding to healthy part of secondary winding
L_P	Self inductance corresponding to primary winding
$(L_P)_0$, $(L_P)_2$, $(L_P)_4$, $(L_P)_6$ …	Coefficients of primary side's self inductance
l	Length
m	Number of data-acquisition tests conducted as part of a single experiment
N_F	Number of turns shorted
N_P	Number of turns in primary winding
N_{PX}	Number of turns in healthy part of primary winding
N_S	Number of turns in secondary winding
N_{SX}	Number of turns in healthy part of secondary winding
$\mathcal{P}$	Magnetic permeance
P_1 , P_2 , P_3	Phases on primary side of three-phase transformer
P_4 , P_5 , P_6	Phases on secondary side of three-phase transformer
$\mathcal{P}_c$	Time-invariant permeance term
$\mathcal{P}_m$	Coefficient of co-sinusoidal permeance term
$\mathcal{R}$	Magnetic reluctance
R_C	Core loss resistance
R_F	Resistance of short-circuited faulty winding
R_L	Load resistance

R_P	Resistance of primary winding
R_{PX}	Resistance of healthy part of primary winding
R_S	Resistance of secondary winding
R_{SX}	Resistance of healthy part of secondary winding
$(V_{IN})_1$, $(V_{IN})_2$, $(V_{IN})_3$ ...	RMS values of harmonic components of primary line voltage
V_P	Nominal RMS value of primary line voltage
V_S	Nominal RMS value of secondary line voltage
v_{C_L}	Voltage drop across load capacitance
v_{IN}	Primary line voltage
v_{OC}	Open circuit voltage
v_X	Voltage drop across primary winding's self inductance
λ_P	Flux linkage referred to primary side
ω	Angular frequency
φ_1 , φ_2 , φ_3 ...	Initial phase angles of harmonic components of primary line voltage
$[\varphi_1]_N$, $[\varphi_2]_N$, $[\varphi_3]_N$ ...	Normalized phase angles of harmonic components of primary line voltage
μ	Magnetic permeability
μ_c	Time-invariant permeability term
μ_m	Coefficient of co-sinusoidal permeability term
μ_o	Permeability of free space
μ_r	Relative permeability
σ	Standard Deviation

Acknowledgements

I would like to acknowledge and extend my deep sense of gratitude to my supervisor Dr. Subhasis Nandi for his valuable time and constant guidance during this thesis work. He has always inspired and encouraged me for meeting high standards of quality and timely completion of the thesis; hence I am highly indebted to him.

I would like to thank the other members of my supervisory committee Dr. A.K.S. Bhat for his valuable time and beneficial comments and suggestions in my thesis preparation.

I would also like to thank all my fellow graduate students and friends for their constant encouragements. My special thanks go to Mr. Kevin Jones and Mr. Rob Fichtner from the Department of Electrical and Computer Engineering for their kind cooperation and help to setup arrangements to conduct many important simulations and experiments.

Finally I would like to thank my parents and wife, who have devoted all they can do to support me in finishing this work and has been a constant source of encouragement.

Dedication

Dedicated to my beloved parents, Mr. Arun C. Bhowmick and Mrs. Anjana Bhowmick

Chapter 1

Introduction to Inter-turn Winding Faults in Transformers

1.1 Importance of transformers in electric power systems and need for transformer fault diagnosis

Rapid growth in the electrical power systems has taken place all over the world since the late nineteenth century. With the rise in consumer demand and development of renewable energy-based power generation, this growth in power systems will continue for years to come. The transformer is the most important part of the power systems network; as it is responsible for transfer of electrical energy from the power generation stage to the transmission stage and finally onto the distribution stage. A typical structure of an electric power systems network [1] is shown in Figure 1.1. Three-phase transformers are used for voltage step-up at the generating sites and voltage step-down at the distribution stations. Single-phase transformers are also used extensively as part of the power distribution networks, ultimately providing power to the domestic consumers.

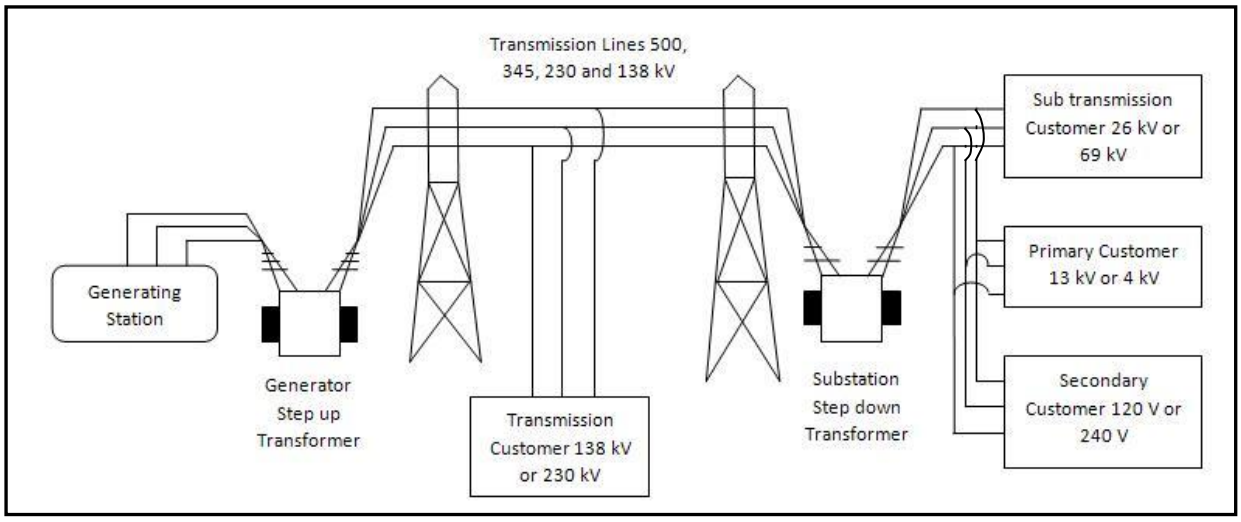

Figure 1.1 Schematic of a typical power systems network [1]

Increased utilisation of equipment deferred capital expenditures and reduced maintenance expenses have become part of today's strategies for transformer operators. To make matters worse, world power consumption is increasing; hence the load on each aging transformer continues to grow [2]. Any faults in transformers leading to power outages or catastrophic power systems failures cause huge loss of capital, property and in some cases even human casualties. In [2], a survey report based on a group of utility companies in USA shows that the total capital losses incurred over a 5-year period 1997-2001 due to transformer failures was $ 286,628,811. Out of this, total property damage was estimated to be $ 163,239,089; while total business interruption was equivalent to $ 123,389,722. Such statistical data emphasizes on the fact that operation of transformers needs to be constantly monitored and diagnostic techniques should be implemented for detecting any faults in them.

1.2 Introduction to transformer inter-turn winding faults

During operation of transformer, the electrical windings and the magnetic core get subjected to a variety of mechanical forces [3], such as:

- Expansion and contraction due to thermal cycling
- Mechanical vibrations
- Localized hot spots due to magnetic flux and current
- Excessive heating due to overloading and/or inefficient cooling
- Impact forces due to through-fault current

Cumulative effects of these forces over a span of time result in gradual deterioration of the electrical winding insulation. Winding faults due to such insulation failures has led to the majority of transformer damages over the years. According to statistics, winding faults led to 51%, 55% and 37% of transformer damages during 1955-1965, 1975-1982 and 1983-1988 respectively [3]. A more recent survey in USA during the period 1997-2001 [2] shows that the winding insulation failures accounted for 25.52% of transformer damages thereby contributing to 52.32% of the total loss of capital (see Table 1.1). Most inter-turn winding short circuit faults

initially start as single turn faults [4, 5, 6] due to insulation breakdown that can happen at any time during the operation of the transformers.

Causes of failures	Number	Capital losses (in USD)
Insulation Failures	24	149,967,277
Design/Material/Workmanship	22	64,696,051
Unknown	15	29,776,245
Oil Contamination	4	11,836,367
Overloading	5	8,568,768
Fire/Explosion	3	8,045,771
Line Surge	4	4,959,691
Improper Maintenance/Operation	5	3,518,783
Flood	2	2,240,198
Loose Connection	6	2,186,725
Lightning	3	657,935
Moisture	1	175,000
Total	94	286,628,811

Table 1.1 Different causes for transformer failures and their capital losses [2]

Incipient stages of an inter-turn insulation failure such as a single turn short circuit fault have negligible impact on the transformer's performance [7]. The changes in the primary and secondary side line currents and voltages are extremely small. Thus, the traditional differential relays [8, 9] which are extensively used for the protection of transformers, cannot detect these

faults at an incipient stage to operate the circuit breakers [4, 10]. However, during such incipient faults the circulating current induced in the shorted turns can be quite high, as the fault current is opposed only by the resistance and the leakage reactance of the shorted turns of the affected winding, which are very small. This phenomenon leads to a localized thermal overloading in the defective part of the winding; thereby causing hot spots. Over some period of time, the generated heat causes the fault to increase in size thereby resulting in the shorting of multiple turns. By the time, the fault manifests itself into a severe phase-to-ground fault and the differential relays operate to trip the circuit breakers; a significant part of the transformer winding already gets permanently damaged. Even time to time monitoring of the insulation resistance of the transformers cannot reliably predict such faults. In order to visualize the shorted turn loop on the star-connected primary side of a three-phase star-delta transformer, Figure 1.2 has been provided. The line currents on the primary side are i_{L1}, i_{L2} and i_{L3} whereas the ones on the secondary side are i_{L4}, i_{L5} and i_{L6}. A winding inter-turns short has been shown in winding '*P1*' on the primary side, where i_F is the fault current. Accordingly, it is advantageous to detect inter-turn fault in its earliest stage for preventing serious transformer damage; and reduce repair costs and outage time.

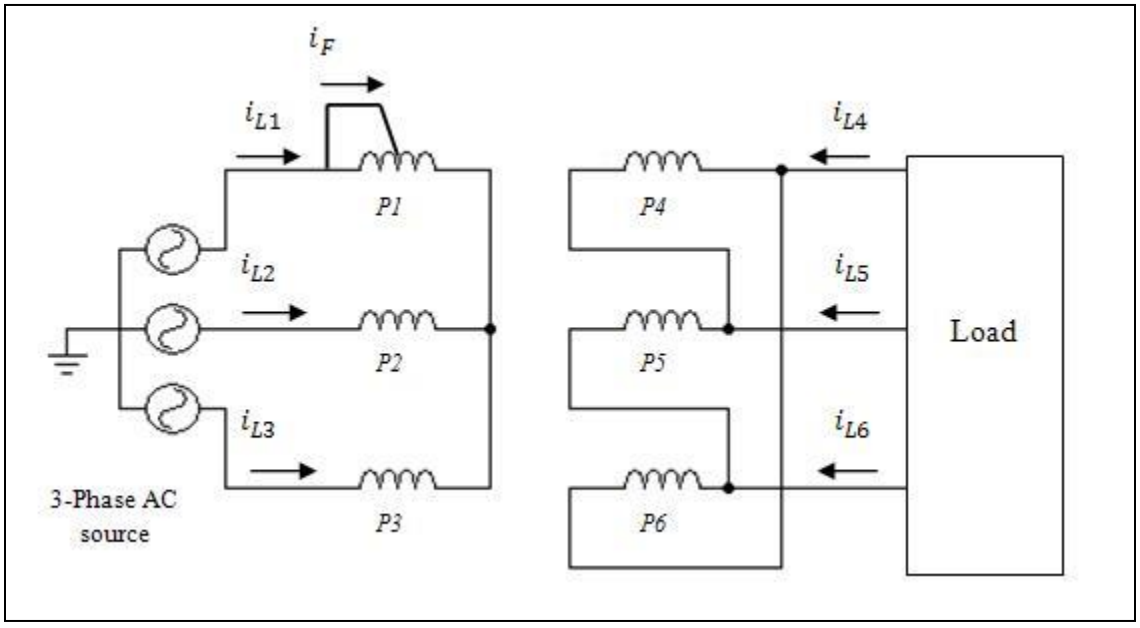

Figure 1.2 Schematic of inter-turn winding fault in three-phase transformer

1.3 Introduction to inter-turn winding fault diagnosis

Transformer manufacturers and operators over the years have employed different tests and methods to detect inter-turn winding faults in transformers [11, 12]. Contemporary researchers have also been involved in rigorous research to come up with more efficient and sensitive inter-turn winding faults detection schemes [13, 14]. Brief descriptions of the various techniques for inter-turn winding fault diagnosis are provided below:

1.3.1 Conventional techniques

- **Magnetic Balance Test –** It is performed on three-phase transformers by energizing only one of the three phases with a lower than rated voltage and keeping all other phases open-circuited. When the middle phase (say 'y') is energized, voltages induced in the other two phases (say 'r' and 'b') for a healthy transformer, are in the range of 40-60% of the applied voltage [11]. However when the phase 'r' (or 'b') is energized, then under healthy condition the voltage induced in the 'y' phase can be as high as 90% of the applied voltage with the remaining voltage induced in phase 'b' (or 'r'). If an inter-turn winding fault exists in a particular winding, then it does not allow any flow of flux in the magnetic path around which it is wound. Due to this an extremely low voltage is induced in the faulty winding. However, this test cannot be conducted on-line as it requires the transformer to be isolated from the load.

- **Buchholz Relay operation –** The Buchholz relay is present in oil-filled transformers [8, 9, 12]. It comprises of two float switches immersed in the transformer oil contained inside the tank. During an incipient fault, gases are formed due to excessive heating and subsequent ionization of the transformer oil. These gases push the oil level down and operate the top float switch which sets an alarm signal. However in case of more severe faults, such as phase-to-phase or phase-to-earth faults, the gas production becomes more prodigious, causing a further lowering of the transformer oil level. This causes even the bottom float switch to operate, sending out a trip signal to the circuit breaker. However, this technique cannot be used for fault detection in dry-type transformers.

- **Dissolved Gas Analysis (DGA) –** It is one of the most primitive methods used for detecting the health of transformers. Under the influence of electrical and thermal stresses, the insulation deteriorates, resulting in formation of different gases, part of which end up dissolving in the transformer oil. Healthy state of a transformer corresponds to a total amount of dissolved gases of 0-500 ppm (parts per million) in the transformer oil. The type and severity of winding faults can be detected by analyzing the relative concentrations of Hydrogen (H_2), Carbon Monoxide (CO), Methane (CH_4), Acetylene (C_2H_2), Ethylene (C_2H_4) etc; as per the Doernenburg Ratios Method and the Roger's Ratio Method [13]. With the aid of gas chromatography instrument, DGA can be performed online [14], however the instrument is very expensive and may not be affordable for some manufacturers and users.

- **No-load test –** After performing the impulse voltage test on a transformer if a particular winding is suspected to have an inter-turn short circuit; then a no-load test is performed to confirm that [11]. No-load loss value shoots up in-case of an inter-turn winding fault. However, a slight increase of about a few % in the no-load loss is sometimes observed after the impulse tests due to partial breakdown of inter-laminar insulation resulting in higher eddy current loss [15]. Also with aging, the no-load losses will increase due to slackness of the core assembly, deterioration of the magnetic property of the core material etc. These facts question the reliability of the no-load test especially for detecting incipient winding faults, where the increase in the no-load loss is quite small in itself.

- **Ratiometer test –** The ratiometer is designed to give a measurement accuracy of 0.1 %, over a ratio range of up to 1110:1 [11]. The ratiometer is used in a ‘bridge’ circuit where the voltages of the windings of the transformer under test are balanced against the voltages developed across the fixed and variable resistors of the ratiometer. Figure 1.3 shows a typical ratiometer set-up for detecting inter-turn fault in transformer TX1 [16]. For a three-phase transformer the other two phases are left disconnected. However, the set-up requires sensitive adjustments and phase shift corrections between the primary and secondary sides, by using ‘T_{adjust}’. It is also essential for the bridge resistors to have low tolerances.

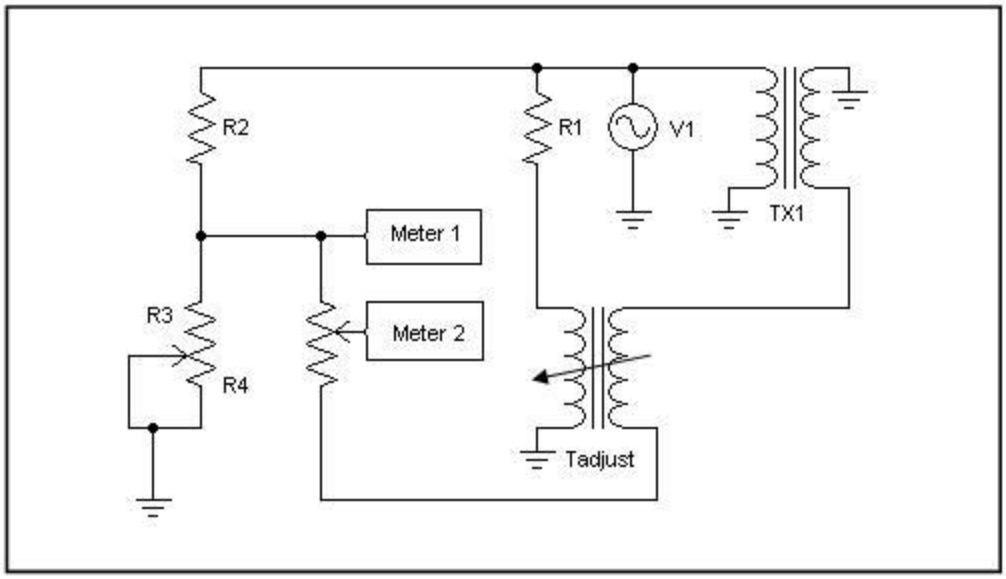

Figure 1.3 Ratiometer test set-up for inter-turn fault detection [16]

1.3.2 Modern techniques – still under research

- **Park's Vector Approach –** An online, non-invasive technique for diagnosing three-phase transformers' winding inter-turn faults has been presented in [4]; which is based on the Park's Vector Transformation of the primary and secondary phase currents. The d-axis (i_D) and q-axis (i_Q) components of the Park's Vector can be derived from the primary side phase currents, following (1.1.a) and (1.1.b) respectively. Under healthy condition of the transformer, the d-axis and q-axis components satisfy (1.2), where I_M is the maximum value of supply current and ω is the angular frequency [4]. The corresponding representation is a circular locus centered at the origin of the coordinates.

$$i_D = \left(\sqrt{2}/\sqrt{3}\right) i_{P1} - \left(1/\sqrt{6}\right) i_{P2} - \left(1/\sqrt{6}\right) i_{P3} \qquad (1.1.\text{a})$$

$$i_Q = \left(1/\sqrt{2}\right) i_{P2} - \left(1/\sqrt{2}\right) i_{P3} \qquad (1.1.\text{b})$$

$$i_D = \left(\sqrt{6}/_2\right) i_{MAX} \sin(\omega t) \quad ; \quad i_Q = \left(\sqrt{6}/_2\right) I_{MAX} \sin\left(\omega t - \frac{\pi}{2}\right) \tag{1.2}$$

In case of a winding inter-turn fault, (1.2) is no more valid and representation of the locus appears more elliptical than that under healthy condition. Detection of the fault is based on identifying the appearance of such an elliptical pattern in the primary side phase current's Park's Vector representation, whose ellipticity increases with the severity of the fault and whose major axis orientation is indicative of the faulty phase. However, this technique was unable to discriminate between unbalanced loads and winding faults [17]. Thus, Park's Vector Transformation of the transformer's exciting current was suggested as superior alternative [17, 18] since the exciting current is independent of the load. Although this technique gives relatively accurate results, it can only be applied to three-phase transformers, which is a major limitation.

- **Wavelet Transform –** Wavelet transform is a mathematical tool for the analysis of a signal. It is the extension of Fourier analysis and can determine the exact time at which a particular frequency occurs in a signal [14]. Shifting (in time) of the peaks of the neutral current waveform of three-phase transformers between reduced and full voltage impulse tests have been employed as a tool for detecting winding inter-turn faults in [19, 20] using the Shannon and Morlet wavelets respectively. In [19], the inherent noise component in the neutral current signal was isolated effectively from the original signal using a biorthogonal wavelet and the signals were reconstructed after de-noising. This improved the performance of the fault detection scheme. A shift in the neutral current peak from 6.45 μsec to 6.6 μsec under the influence of a winding fault was reported in [19]. Further research has been done in [21], using the wavelet transforms coefficients to distinguish a winding inter-turn fault from the magnetizing inrush current phenomena. However, the shifting in the current peaks in time domain is generally very minimal and incipient winding faults can easily get unnoticed.

- **Artificial Neural Networks (ANN)** – In recent times, Artificial Neural Networks have emerged as an advanced tool for pattern classification, function approximation and system identification [14]. Multi-layer, feed-forward, back-propagation based ANNs can

be first trained for the various differences in transformer characteristics during a fault; then it can act as a decision making tool to identify and even locate the fault online. For instance, in [22, 23] winding transfer admittance function and winding transfer voltage function were computed for a variety of fault cases and then used for training an ANN algorithm for fault detection. In [24], an ANN was successfully developed to predict incipient fault in oil-filled power transformers using three ratios of dissolved gases – Acetylene (C_2H_2) to Ethylene (C_2H_4) ratio, Methane (CH_4) to Hydrogen (H_2) ratio and Ethylene (C_2H_4) to Ethane (C_2H_6) ratio; as shown in Figure 1.5. Similar results have been provided in [25, 26]. However, ANN methods of fault detection suffer from some major limitations such as the need for a large number of training cases, high memory requirement and computational complexity.

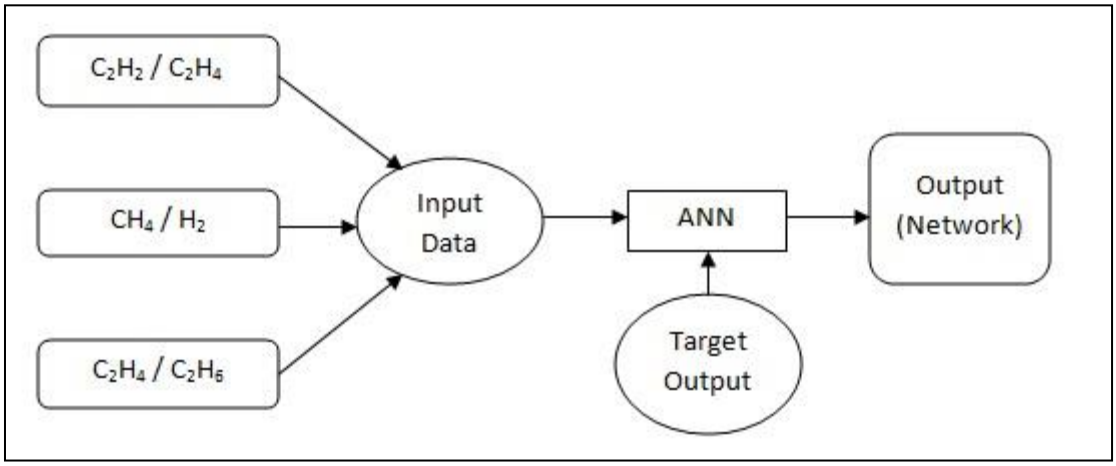

Figure 1.4 Block diagram of the ANN based fault detection scheme [24]

- **Frequency Response Analysis (FRA) –** This technique mainly involves measuring the impedance of the windings of a transformer with a low voltage sine-wave input varying in a wide frequency range [14]. The measurements taken for a healthy transformer are used as a reference; any deviation from this reference set of results indicates the occurrence of a fault. Earliest studies in FRA based transformer fault detection were done in [27]. In recent times, FRA technique has been employed to detect a variety of faults in

transformers such as inter-turn fault, failure of transformer oil and axial and/or radial winding displacements [28]. However, a detailed study on the sensitivity of the FRA technique [29] shows that the detection of an inter-turn fault is possible only for shorting resistances having the upper limit values ten thousand times higher than the resistance of a single turn shorted. Also the instrument necessary to carry out the FRA analysis is very expensive and hence it is economically viable only for large transformers rated for few MVAs. These facts impose limitations on the large-scale use of the FRA technique for winding faults detection in transformers of different ratings.

- **Other methods –** An online technique for detecting incipient inter-turn winding faults has been demonstrated in [10]; which is based on the ratio of the negative sequence components of the primary and secondary line currents. The ratio is equal to the turns ratio of the transformer during healthy condition as well as during external faults, supply and load imbalances; while it differs from the turns ratio when inter-turn winding faults occur. In [30], the nature of the zero-sequence current in the delta winding of a three-phase transformer is studied under pre-fault and post-fault conditions, for developing a fault detection mechanism.

  A novel differential voltage relaying scheme for inter-turn winding fault protection of transformers based on the Midpoint-Technique has been suggested in [31]. Relays are connected between the two terminals of each phase winding and their midpoints. Under healthy condition, the voltages in both halves of the windings were same. Even a one volt difference in the two voltages during an inter-turn fault, was found to be high enough to energize the voltage relay and isolate the machine. Figure 1.5 demonstrates this fault detection scheme as applied to any winding ‘AB’ of a transformer having the center of the winding at ‘M’. However, practical implementation of this technique is difficult as it needs the manufacturers to construct additional midpoint terminals in every winding of a transformer.

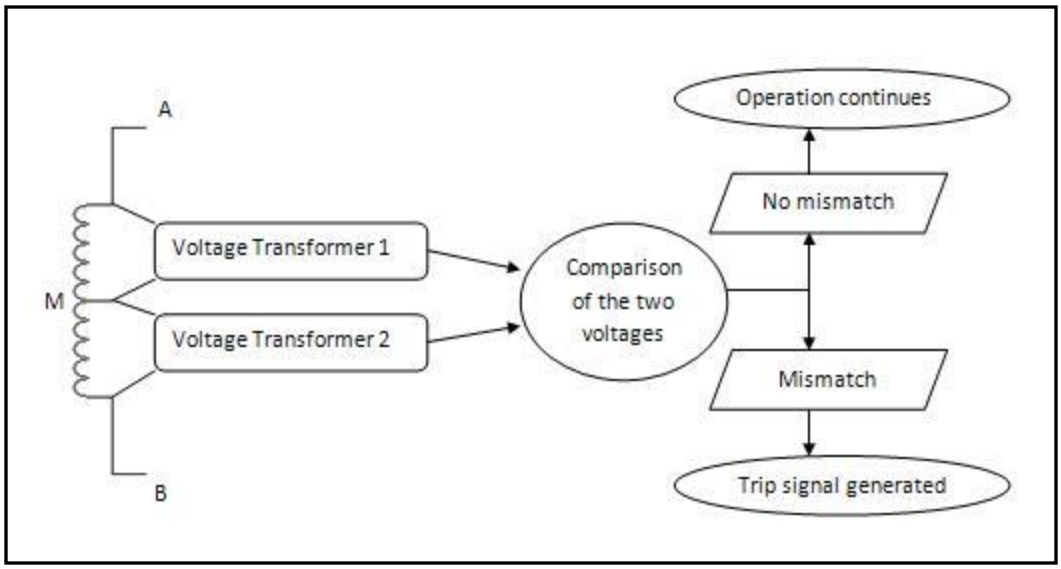

Figure 1.5 Block diagram of the midpoint technique based fault detection [31]

The variation in the leakage flux of the concentric-type and disc-type windings of power transformers under inter-turn faults was investigated in [32, 33]. The variation in the leakage flux was found to be a good indication of the presence of a fault. However, this technique requires air-core coils to be inserted around the primary and secondary windings for accurate measurements of the leakage flux. This makes the leakage-flux measurement based fault detection method invasive and hence, limits its practical implementation.

In [34], a fault-detection algorithm based on the Ratio of the Increments of the primary and secondary winding Flux Linkages (RIFL) has been developed. RIFL is equal to the turn ratio during normal operating conditions, magnetizing inrush and over-excitation; whereas it differs from the turns ratio during an internal winding fault. This technique has been further improved and implemented in a digital signal processor in [35], for inter-turn fault detection and identification of the faulted phase and winding.

In [36], the Cartesian relationship between the differential line voltage (difference of the primary and secondary line voltages) and the primary line current of a single-phase transformer was found to represent an ellipse. The changes in the eccentricity, angle of

rotation and minor and/or major axes lengths of this elliptical locus, under the influence of various mechanical faults were studied. A block diagram of the proposed fault detection methodology is represented in Figure 1.6. Simulation results were provided for various mechanical faults corresponding to 80 % and 5 % of the overall discs in the transformer model. It was evident that for a severe inter-disc fault (equivalent to an inter-turn fault for a disc-type winding) the elliptical locus increased in its area and also showed significant clockwise rotation. However, for incipient faults such as a single-turn short circuit fault, the variation in the shape and structure of the elliptical locus is negligible. This shows that the proposed methodology is not reliable enough for the detection of incipient winding faults. Also, for a transformer having a unity turns ratio such as an isolation transformer, this technique cannot be used.

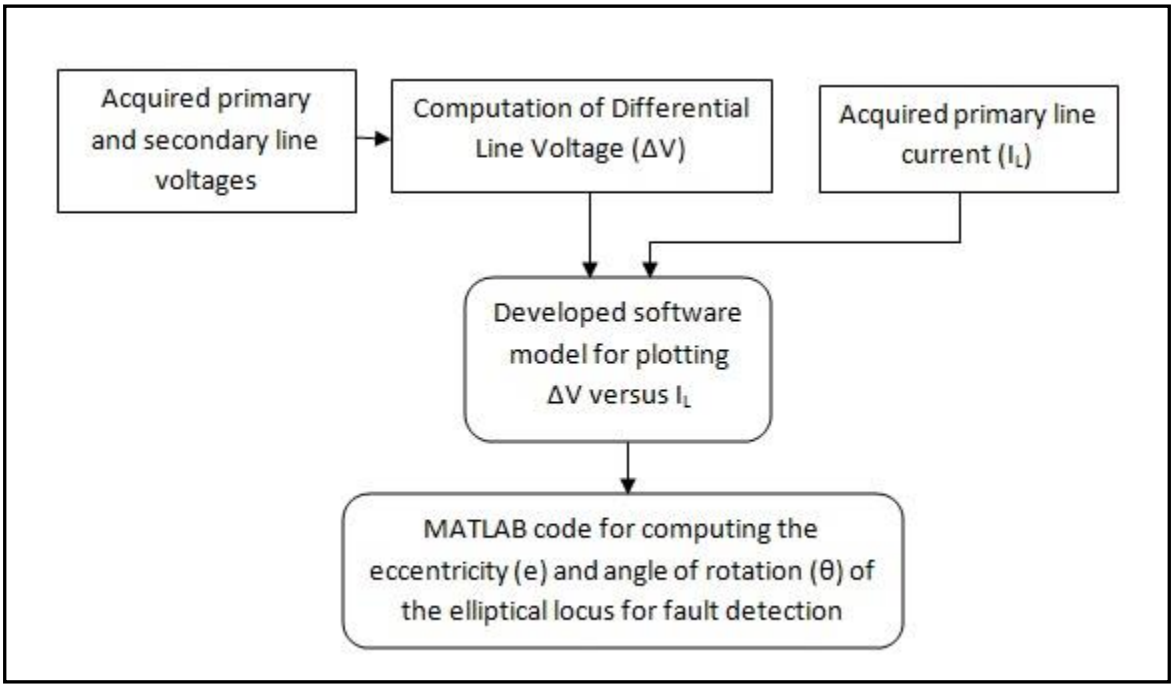

Figure 1.6 Block diagram of the Differential Line Voltage versus Line Current based fault detection scheme [36]

Three new algorithms for online and non-invasive detection of inter-turn faults have been developed in [37] based on the differential equations representing the equivalent circuit of the transformer. The criterion signal used for fault detection in all the three algorithms, was a voltage signal proportional to the fault current. Promising results were obtained from the algorithms employing the use of zero sequence voltages and currents, with or without additional information from a current transformer in the delta winding.

A frequency-domain based analysis of the transformer's exciting current for the detection of inter-turn winding faults has been introduced in [16]. First, the odd triplen harmonics were identified as the fault specific frequency components in the exciting current. Then these frequency components were monitored for diagnosing inter-turn winding faults. The scheme was shown to reliably detect incipient faults as low as a single-turn short circuit fault, in a three-phase transformer made from a bank of three individual single-phase transformers working at no-load. However, for a single-phase stand alone transformer, the odd triplen harmonics showed no signs of increase even in case of a five turns short circuit fault; thus highlighting the short-coming of the frequency-domain based fault detection scheme under this specific condition. Some other researchers have also identified the harmonic content in the exciting currents as a good indicator of the current state of transformer's operation and its magnetic core condition [38, 39].

1.4 Motivation and Objective of Present Work

From the above facts, it can be clearly felt that the existing techniques of condition monitoring of transformers suffer from some limitations. Some of the tests for detecting the integrity of transformer windings need to be carried out away from the transformer's installation site, in specialized test facilities. Also some other fault detection schemes are invasive in nature and require the incorporation of special sensors and/or coils inside the transformer tank. Additionally, none of the existing techniques were found to be sensitive enough for reliable detection of a single-turn winding short circuit fault. Hence, this research area needs special attention.

In this work, an attempt has been made to develop a diagnostic technique that is capable of detecting the incipient stages of inter-turn short circuit faults in transformer windings. The developed technique can be used for fault detection on single-phase transformers, either dry-type or oil-filled-type. Also, the technique has been demonstrated to detect such incipient faults under no-load as well as on-load conditions including different levels and types of load such as a resistive (R) type, a resistive-inductive (RL) type and a resistive-capacitive (RC) type load.

Firstly, a non-invasive modeling technique for transformers has been developed which is based solely on the terminal measurements of the voltages and currents. Also, the effects of transformer core non-linearity and saturation effects have been incorporated in the model. Secondly, incipient single-turn winding faults have been simulated (using the proposed modeling technique) and experimentally created on the primary and secondary windings of a single-phase transformer under different load conditions. Finally, a novel fault detection parameter, based on the Total Harmonic Distortions (THDs) of the transformer exciting current and input voltage, has been developed for reliably detecting incipient winding faults. The effectiveness of the fault detection parameter in diagnosing more severe faults (up to five-turn faults) has been demonstrated as well through simulation and experimental results.

1.5 Thesis Outline

The thesis has been structured as follows. In Chapter 1, a general discussion has been presented on the major causes for transformer failures. From that, the necessity for condition monitoring of transformers in the power transmission and distribution networks has been highlighted. Finally, a literature survey of some of the existing inter-turn winding fault detection techniques has been listed and discussed. The short-comings of the previous research have also been discussed briefly.

In Chapter 2, a literature review of the different transformer models used for condition monitoring, has been provided. Then, the proposed terminal measurements based modeling of a single-phase transformer has been presented. Firstly, the magnetizing inductance profile of the transformer has been computed from the terminal voltage and current data, which were acquired

using a data acquisition system. Then, coupled inductance based state-space model for the transformer under healthy condition has been simulated incorporating the computed magnetizing inductances.

In Chapter 3, detection of inter-turn winding fault in a single-phase transformer has been presented. Detailed mathematical modeling has been provided to represent the single-phase transformer under faulty state. Then various simulation results have been provided to demonstrate the efficiency of the proposed technique in diagnosing incipient as well as severe inter-turn winding faults on both primary and secondary windings, under different levels and types of load.

Chapter 4 provides detailed experimental results for demonstrating the performance of the fault-detection scheme in a real-life setting. Experiments have been carried out on a custom-made single-phase transformer provided with a number of tapping-points for artificially creating inter-turn faults in the laboratory. Results for incipient as well as severe inter-turn winding faults on both primary and secondary windings, under different levels and types of loads have been provided. A practical implementation of the proposed technique has been also described for online, real-time monitoring of the transformer health.

Based on the simulation and experimental results, a methodology for practical implementation of the fault detection scheme has been discussed in Chapter 5. Also, recommendations have been made as a future scope for conducting further research on the proposed method for inter-turn winding fault detection in transformers. Finally, contributions of this research work and conclusions have been described in Chapter 6.

Chapter 2

Terminal Measurements Based Modeling of Single-Phase Transformers under Healthy State

In this chapter, a literature review of the various modeling techniques used for condition monitoring and fault diagnosis of transformers has been presented and the short-comings of the existing models are highlighted. This is followed by a detailed description of the proposed terminal measurements based modeling technique. A single-phase transformer has been modeled using this methodology and all necessary mathematical derivations have been provided. Finally, these results have been validated with experimental results.

2.1. Need for modeling of electric machines for fault detection

The computer models of the electric machines are required for two major reasons:

- **Study of faults and their characteristics** – The first step to fault detection in electric machines is to develop a clear idea about the nature of the fault and its impact on the electrical and magnetic circuits of the machines. Since, artificially inducing these faults in electric machines for study purposes can be very expensive and dangerous; computer models are used as a suitable alternative. Simulation of various electrical and mechanical faults in the computer models gives a good estimation of the real-life behaviour of the electric machines under the faults.

- **Development of fault detection schemes** – Computer models are also essential to conduct extensive research needed for pointing out various fault-specific physical parameters in the electric machines. These parameters can then be monitored real-time and/or online as an indication of the occurrence of a fault.

2.2 Introduction to modeling of transformers

Some of the important elements needed to be considered while modeling transformers are – representation of the windings and iron core, impact of skin effect and proximity effect in the current-carrying conductors, rise in operating temperature, magnetic core non-linearity and saturation. Skin effect is the tendency of AC current to get distributed within a conductor such that the current density is maximum near the conductor surface. Proximity effect on the other hand, is the phenomena of increase in the concentration of AC current in the areas of a conductor furthest away from other nearby conductors carrying current in the same direction. Skin effect and proximity effect play important roles in High Frequency (HF) transformers used in pulse width modulated (PWM) power converters and switched mode power supplies (SMPSs) as they cause additional winding losses due to harmonics [68]. However, in transformers operating at low-to-mid frequencies, these effects are negligible. The effective series winding resistance of transformers comprise mainly of metal resistance (resistance of the copper with which the windings are manufactured) at low-to-mid frequencies of operation [69]. Thus, an increase in the effective winding resistance occurs with rise in the operating temperature of the transformer. The B-H curve of commonly used materials for manufacturing the transformer core is non-linear. This results in hysteresis and saturation effects which are very essential to consider in the transformer models. So broadly speaking, the two major elements of a transformer model are the representation of the windings which is linear and representation of the iron core which is non-linear [40]. The interpretation of the modeling of these two elements varies depending on the application of the transformer model. For instance, in power-systems and load-flow studies accurate representation of the core magnetics is generally not considered whereas in condition monitoring and fault diagnosis, the core forms an integral part of the overall transformer model. The three generic types of transformers models as described in [40] are the Impedance/Admittance matrix based models, Saturable Transformer Component (STC) based models and Transformer Topology based models.

In case of internal faults of transformers such as inter-turn winding faults, the flux distribution gets altered around the affected area of the magnetic core. Thus, models used for the study of such faults need to incorporate an accurate representation of the core characteristics. In other

words, the models should represent the saturation of the core, non-linearity of the B-H curve of the core material, any inherent abnormalities in the core caused at the time of manufacturing or developed later due to aging etc. Such a representation of the iron core is very important. However, it is the most challenging part of the modeling procedure because both the magnetizing inductance and core losses (generally represented by the equivalent core-loss resistance) are non-linear and frequency-dependent [41]. Some of the different models of transformers for such condition monitoring purposes described in the literature, have been reviewed below:

- **Inductance based models** – One of the earliest transformer models ideally suited for the study and analysis of winding faults has been suggested in [42]. In [42], for a three-phase transformer with windings '1', '3' and '5' on the primary side and corresponding secondary winding being '2', '4' and '6'; the model computes the Resistance Matrix 'R' and the Inductance Matrix 'L' and employs them to solve the electric circuit equations. However, computation of the leakage and mutual inductances between the windings involves rigorous mathematical calculations for determining the coefficients of coupling and leakage factors. Furthermore, these calculations require precise information about the number of turns, permeability of the core material and core geometry. Similar inductance based models have been developed in [16, 43, 44] but they all have the same limitation i.e. they all need transformer core details.

- **Reluctance based models** – These models essentially comprise of two stages. In the first stage the magnetic equivalent circuit of the transformer is developed in terms of the magneto-motive force (MMF) sources, magnetic flux and the permeances or reluctances in different limbs and yoke segments [18, 45]. In the second stage, the coupled magnetic circuit differential equations are arranged in state-space models and solved for obtaining various electrical parameters such as flux linkages, currents etc [46]. Computation of the magnetic permeances and reluctances of various core sections is based on (2.1), where '$\mathcal{P}$', '$\mathcal{R}$', 'A' and 'l' represent permeance, reluctance, cross-sectional area and length of the core section respectively [47]. The permeability of free space and relative magnetic permeability of the core material are given by 'μ_o' and 'μ_r' respectively.

$$\mathcal{P} = \frac{\mu_o \mu_r A}{l} \quad ; \quad \mathcal{R} = {}^{1}/_{\mathcal{P}} \tag{2.1}$$

In [48], this modeling strategy has been implemented for computation of transformer inrush currents, whereas a three-phase transformer with three legs under DC bias have been accurately modeled and simulated in [49] using similar methodology. Additional research also has been done to accurately incorporate hysteresis losses in such transformer models [50]. Although these models have been found to portray the internal magnetic behavior of the transformer core up to a high degree of accuracy, they suffer from a major disadvantage – the models require information about the cross-sectional area, lengths and core material's permeability values are required.

- **Finite-element models (FEMs)** – One of the earliest studies in transformer modeling using FEM is reported in [51]. The main advantages with FEMs are: high accuracy, availability of computer-aided-design (CAD) based modeling interface, provision for developing 2D and/or 3D designs, integration with SPICE based electric circuit-design platforms etc. Due to these positives, the FEM based technique has been used for accurately modeling the non-linearity of the iron core of transformers [52]. In [53], a 2D model for E-core type transformers has been developed using FEM, incorporating the effects of fringing flux for gapped core legs. Also, anisotropy and air gaps in core joints have been accurately modeled in [54] using FEM, which were not possible in reluctance-based or inductance-based mathematical models. Even the stray losses in power transformers have been estimated accurately using 3D FEMs [55-57], which are otherwise hard to compute physically. Moreover, FEMs have been extensively used for computing the eddy current losses of transformers [58-60]. Even the eddy current losses encountered in the transformer tank walls have been investigated in [61] using a 3D FEM. However, the FEM-based modeling involves high computation power, large memory requirements and long simulation times. Due to such disadvantages, they are not suitable for on-line and real-time implementation for transformer fault diagnosis.

- **Other developed models** – A piece-wise linearization technique has been employed for developing the excitation curve (excitation current versus magnetic flux) of a transformer

in [62]. The hysteresis effect has been incorporated by representing the excitation current as the sum total of two flux-dependent current quantities and the various harmonics in the exciting current have been computed accurately using the Harmonic Balance Method (HBM). Frequency-domain and time-domain modeling of the non-linear characteristic of the transformer core has also been presented in [63]. Several relationships have been developed between the magnetizing current (i_M) and flux linkage (λ). According to the first method, the magnetizing current versus flux linkage curve for the first quadrant, has been represented by a polynomial function as given in (2.2). In the second method, the entire hysteresis curve has been divided into four different segments and the relationship between these two quantities for each segment has been determined. This is shown in (2.3).

$$i_M = A_O + A_1\lambda + A_2\lambda^2 + A_3\lambda^3 + \ldots \tag{2.2}$$

$$\begin{aligned} i_M &= A + Be^{C\lambda} \quad \ldots\ldots \quad for\ segment\ I \\ i_M &= D + Ee^{F\lambda} \quad \ldots\ldots \quad for\ segment\ II \\ i_M &= -D - Ee^{-F\lambda} \quad \ldots\ldots \quad for\ segment\ III \\ i_M &= -A - Be^{-C\lambda} \quad \ldots\ldots \quad for\ segment\ IV \end{aligned} \tag{2.3}$$

The application of look-up tables have been explored for accurately representing the magnetizing inductance and core-loss resistance of a transformer in [41]. An open-circuit voltage versus core-loss current based look-up table has been developed to estimate the core-loss resistance; while a magnetic flux linkage versus magnetizing current based look-up table has been developed to estimate the magnetizing inductance. The open circuit voltage and exciting current were acquired by probes and then fed to a computer for data processing. Flux linkage was obtained by rescaling the acquired voltage using (2.4) where v_{OC} represents the open circuit voltage. The technique showed good promise in terms of accuracy in modeling and also involved measurement of only terminal quantities.

$$\lambda = \int v_{OC}\,(t)dt \tag{2.4}$$

In [16], additional attention has been given in modeling the saturation effect in the transformer core. Variation of the permeability in the transformer core and hence, a variation in the core permeance is caused due to the flow of the magnetizing current [64]. These variations in permeability and permeance have been modeled as per (2.5) and (2.6), to incorporate the effect of core saturation. 'μ_c' and '$\mathcal{P}_c$' are the time-invariant terms in the expressions for '$\mu(t)$' and '$\mathcal{P}(t)$'; whereas 'μ_m' and '$\mathcal{P}_m$' are the peaks of the co-sinusoidal terms in these expressions respectively.

$$\mu(t) = \mu_c + \mu_m \cos(2\omega t) \tag{2.5}$$

$$\mathcal{P}(t) = \mathcal{P}_c + \mathcal{P}_m \cos(2\omega t) \tag{2.6}$$

2.3 Proposed terminal measurement based modeling technique

From the above facts, it is clear that a non-invasive method for modeling of transformers which is independent of the magnetic core specifications and design data needs to be developed. This can then be utilized for the study and diagnosis of different internal faults in transformers such as inter-turn winding faults.

In this section, a technique for transformer modeling using only the terminal measurements of line current(s) and voltage(s) has been discussed. Firstly, the voltage and current waveforms are captured through Hall-effect sensors and the flux linkage is computed by integrating the voltage. Then the instantaneous values of the magnetizing inductance are determined from the corresponding instantaneous flux linkage and magnetizing current values for a number of instances along the flux linkage cycle. The magnetizing inductance is represented as a sum of various higher order, co-sinusoidal harmonic terms. The instantaneous values of magnetizing inductance are equated to this trigonometric representation, thereby forming algebraic equations corresponding to each of these instances. By solving these simultaneous linear equations, the various coefficients of the magnetizing inductance are computed. Finally the computed magnetizing inductance is used in a coupled inductive circuit based state space transformer model, to obtain its dynamic performance characteristics. The implementation of this modeling

technique is simple, non-invasive and cost-effective. Additionally, the generation of the magnetizing inductance profile is based on real current and voltage data. Thus factors like non-linearity of the core material's B-H curve, saturation effects or any other core imperfections like degradation, looseness of laminations, aging etc are automatically accounted for. Large power transformers suffer from excessive stray losses, which comprise of 20-25 % of their load losses [55]. However, smaller distribution class transformers do not have this issue. As the proposed modeling technique does not account for any stray losses, it is more suitable for modeling such low rating single-phase and three-phase distribution transformers. Models for larger transformers with high voltage (hundreds of kilovolts) rating may also need modifications for incorporating the large inter-turn capacitances associated with large windings.

2.3.1 Modeling of single-phase transformer under healthy state

Data obtained from the terminal measurements of a 150 VA, 60 Hz, 120/120 V, single-phase, shell-type transformer have been used for the modeling. In this subsection, the transformer modeling procedure is described in three simple steps.

Step 1 – Data Acquisition:

Running the transformer under no-load condition, the input voltage and the exciting current were acquired for 10s at a sampling frequency of 18 kHz using a 100 kS/sec data acquisition system [65] and Hall-effect sensors. To eliminate high frequency noise the data were then filtered using a 6^{th} order low-pass Butterworth digital filter of 1 kHz cut-off frequency using the MATLAB Filter Design Toolbox [66]. For performing zero phase digital filtering, the 'filtfilt' command in MATLAB was used as it processed the input data in forward as well as reverse directions [72]. Hence, the features in the filtered waveforms were preserved exactly at the instances of time where they occurred in the unfiltered waveform and any possible phase shift errors in the filtered waveforms were prevented. Figures 2.1 and 2.2 show the acquired input voltage and exciting current respectively. It is clearly evident that the input voltage obtained from the laboratory's power supply is distorted and contains higher order harmonics.

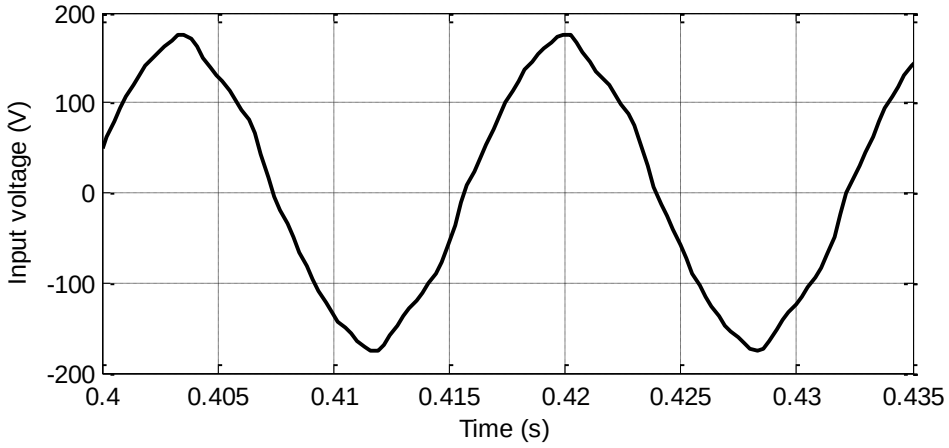

Figure 2.1 Acquired input voltage

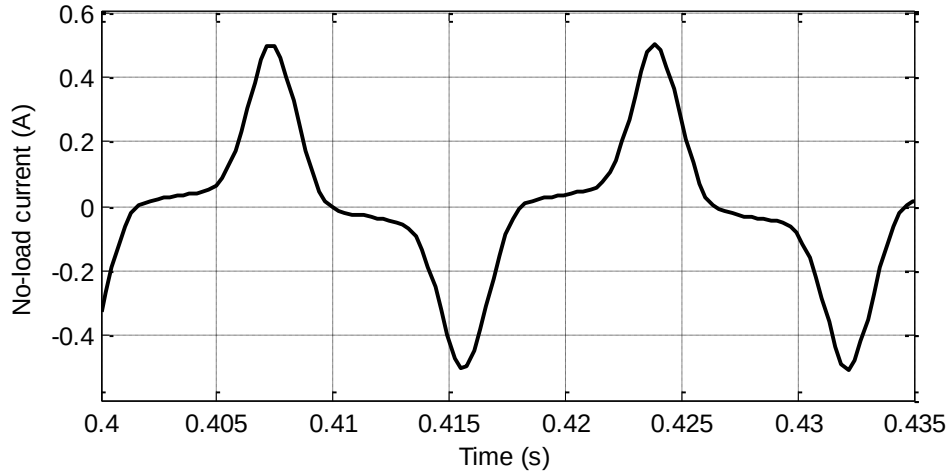

Figure 2.2 Acquired exciting current

The acquired waveforms were then down-sampled using a 3.6 kHz sampling frequency in order to remove any local minima and/or maxima undesirably present in the exciting current waveform (especially along the low-slope regions near its zero-crossing points). These local minima and maxima points were possibly present in the acquired current waveform due to the lack of sensitivity of the used Hall-effect current sensor; because the exciting current itself was in the order of milli-amperes and the instantaneous current values corresponding to the low-slope regions were even smaller.

Step 2 – Generation of magnetizing current and flux linkage profiles:

The equivalent circuit of a single-phase transformer operating under no-load condition is shown in Figure 2.3 [67]. R_P and L_{lP} are the primary winding resistance and leakage inductance respectively, while R_C represents the equivalent core-loss resistance. L_{MP} represents the magnetizing inductance corresponding to the primary winding. Equation 2.7 represents the magnetizing inductance branch where L_P is the primary winding's self inductance which is equal to the sum of L_{MP} and L_{lP} as in (2.8). Substituting (2.8) into (2.7) yields (2.9), which represents the magnetizing inductance branch in terms of L_{MP} and L_{lP}. It will be seen in the subsequent subsection, that (2.9) is used for representing the primary side of the transformer under no-load condition in order to simulate the transformer.

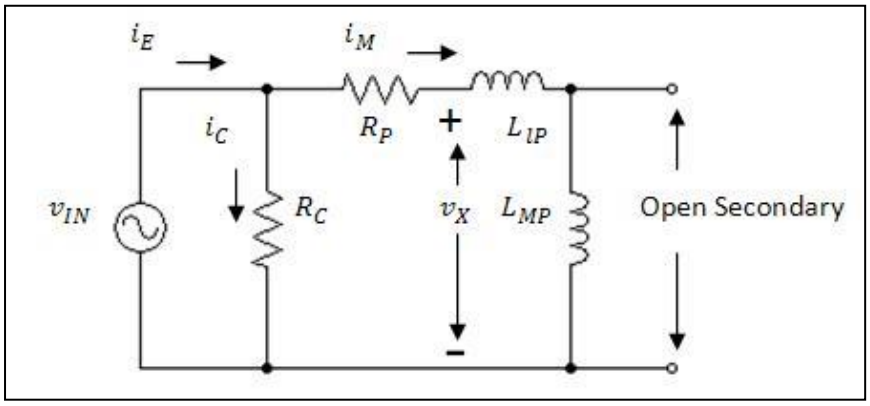

Figure 2.3 Equivalent circuit of single-phase transformer under no-load operation

$$v_{IN} = i_M R_P + \frac{d}{dt}(i_M L_P) \tag{2.7}$$

$$L_P = L_{MP} + L_{lP} \tag{2.8}$$

$$v_{IN} = i_M R_P + \frac{d}{dt}(i_M[\, L_{MP} + L_{lP}\,])$$

$$\therefore \quad v_{IN} = (i_M R_P) + L_{lP}\left(\frac{di_M}{dt}\right) + i_M\left(\frac{dL_{MP}}{dt}\right) + L_{MP}\left(\frac{di_M}{dt}\right) \tag{2.9}$$

Next, the magnetizing current (i_M) is obtained from the exciting current (i_E) and the core-loss current (i_C) using (2.10). Under no-load operation, the exciting current is equal to the no-load current of the transformer.

$$i_M = i_E - i_C \quad ; \qquad \text{where} \qquad i_C = {}^{v_{IN}}/_{R_C} \tag{2.10}$$

Short circuit and DC resistance tests were performed on the 150 VA single-phase laboratory transformer to obtain the values of R_P and L_{lP} as 2.36 Ω and 3.35 mH (assumed to be half of the total leakage inductance measured using the short circuit test) respectively. R_C was also determined to be 3356.56 Ω from the open circuit test. Usually for transformers these data can be obtained from the manufacturer, thus these tests need not be repeated on-site unless the transformer has been in operation for a long period of time. Even otherwise, these are routine tests which can be performed very easily.

Using the known value of R_C the core-loss current i_C was computed first and then, the magnetizing current i_M was generated. The various currents are shown in Figure 2.4.

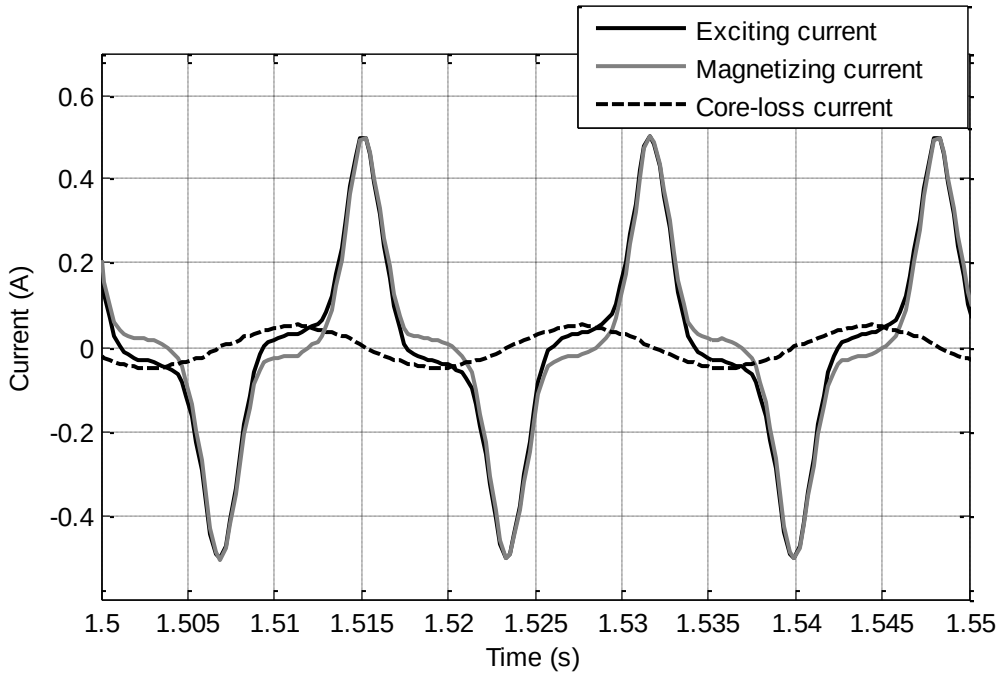

Figure 2.4 Magnetizing current profile generated from the exciting and core-loss currents

The voltage drop across the primary winding's self inductance (v_X) can be derived from (2.7) and is given by (2.11).

$$v_{IN} - i_M R_P = \frac{d}{dt}(i_M L_P) = v_X \tag{2.11}$$

Using the known value of R_P the voltage drop across the primary winding resistance is computed first and then it is subtracted from the input voltage to obtain v_X . The voltage drops across the primary winding resistance and self inductance are shown in Figures 2.5 and 2.6 respectively.

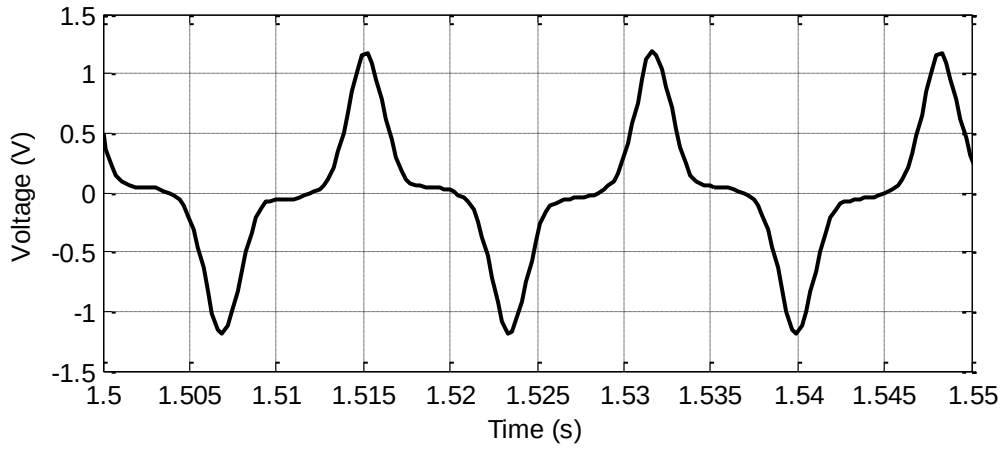

Figure 2.5 Voltage drop across the primary winding resistance

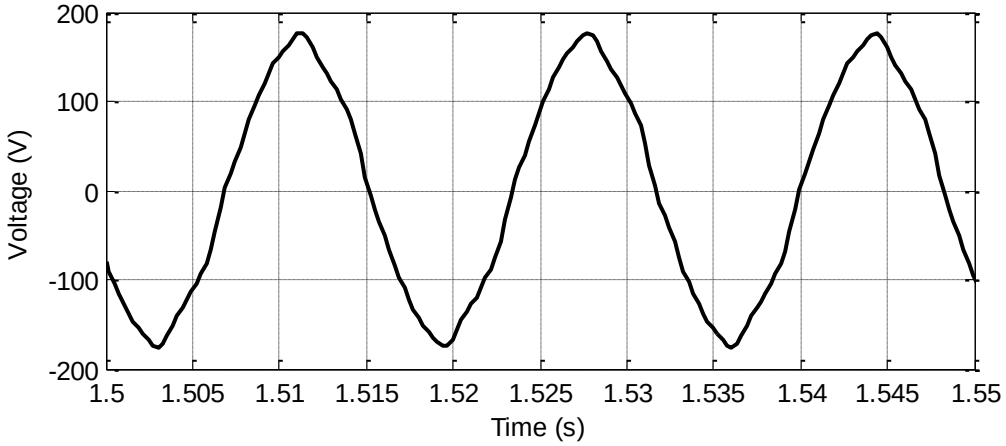

Figure 2.6 Voltage drop across primary winding's self inductance

Once the profile of v_X is generated, the flux linkage referred to the primary side (λ_P) is obtained by integrating this voltage according to the Faraday's Law, as shown in (2.12). Figure 2.7.a shows the flux linkage waveform, which was generated through trapezoidal integration by using the 'trapz' command in MATLAB. Due to lack of sensitivity of the voltage probe, a small DC offset was present in the unfiltered as well as the digitally filtered voltage waveforms. Presence of this DC offset leads to integration error and yields a flux linkage waveform whose RMS value increases in every cycle. Hence, a small offset correction factor of (0.562) was subtracted from the v_X waveform, before performing the trapezoidal integration. Figure 2.7.b shows the generated magnetizing current waveform. The fundamental component of permeance variation due to the magnetizing current, normalized with respect to the average permeance value, is shown in Figure 2.7.c. At the positive and negative peaks of the current, the permeability and hence permeance has the lowest possible values due to magnetic saturation. Similarly, near the zero crossings of the current, permeability and permeance are maximum. Hence, corresponding to the fundamental component of permeance variation can be approximated as a co-sinusoidal waveform with twice the frequency of the fundamental current. In real-life transformers, the magnetizing current contains higher-order saturation-related harmonics. Thus, higher-order co-sinusoidal terms also need to be incorporated in the permeability and permeance variations; and subsequently, for representing the variations of self- and magnetizing inductances.

$$\lambda_P = \int (v_X)\, dt \tag{2.12}$$

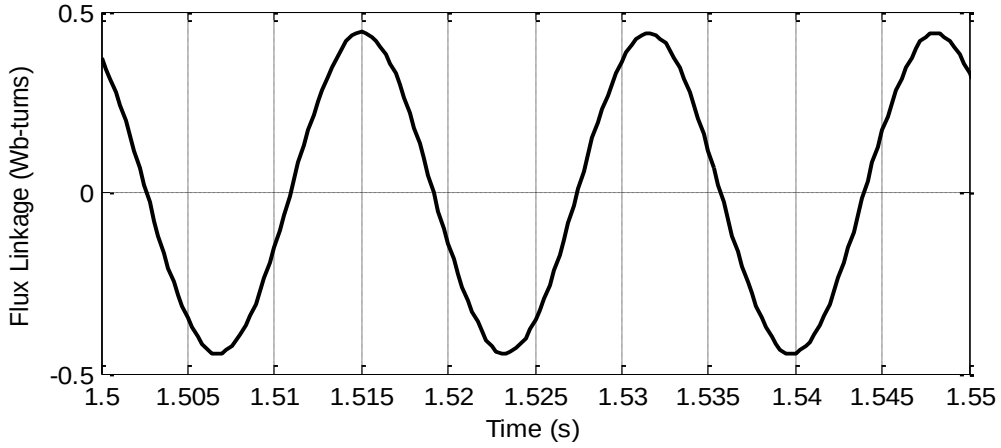

Figure 2.7.a Generated flux linkage profile

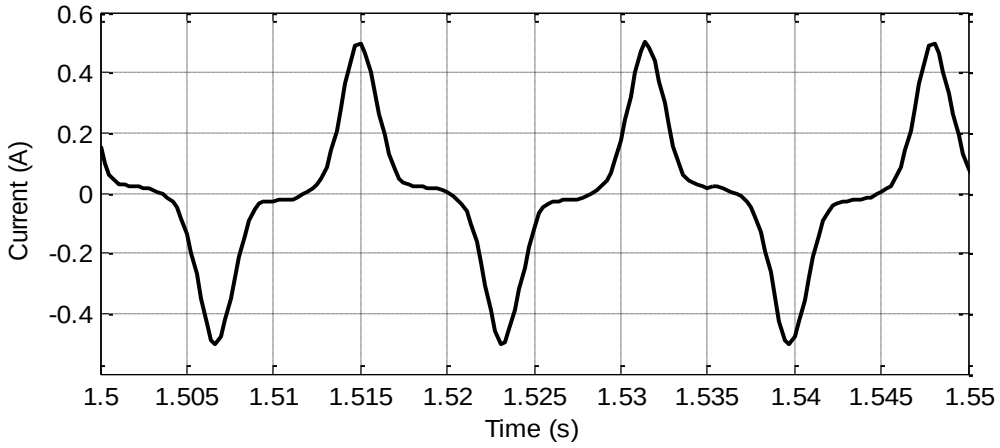

Figure 2.7.b Generated magnetizing current profile

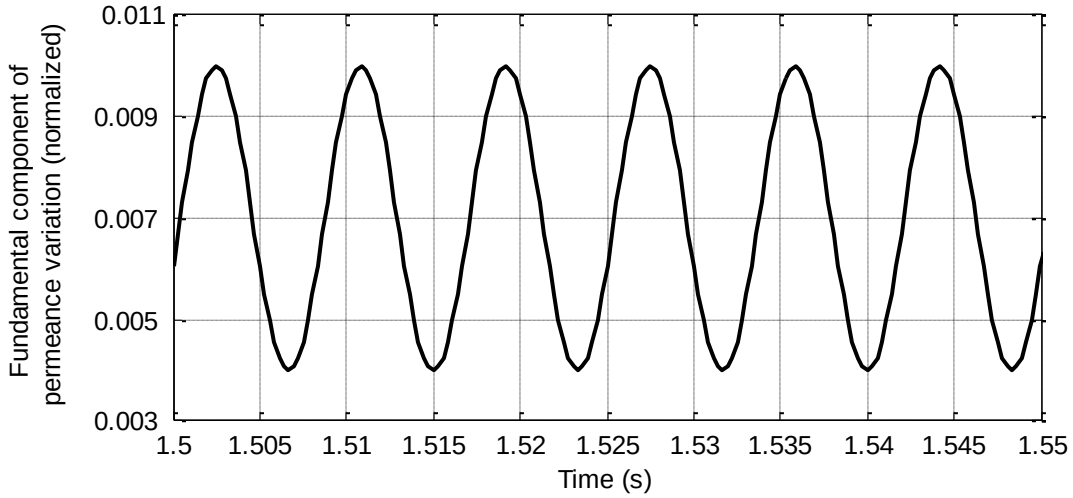

Figure 2.7.c Fundamental component of permeance variation (normalized) due to magnetizing current

Step 3 – Computation of the magnetizing inductance coefficients:

The cyclic variation in the magnetizing current results in variation of the relative permeability of the transformer core and therefore a corresponding variation in the permeance of the core [64]. Subsequently, a cyclic variation in the self inductance and hence, in the magnetizing inductance occurs as well. It is a well-known fact these inductances are functions of the magnetizing current, which again is a function of time. Hence, the self and magnetizing inductances can be

represented by time dependent infinite series as in (2.13) and (2.14) respectively, to model the effects of hysteresis and saturation [16, 70]. They can incorporate the peak values associated with any desired number of higher order saturation-related harmonics. The relationships between the coefficients of the self and magnetizing inductances are given in (2.15).

$$L_P(\omega,t) = [(L_P)_0] + [(L_P)_2]\cos\{2\omega t\} + [(L_P)_4]\cos\{4\omega t\} + [(L_P)_6]\cos\{6\omega t\} + [(L_P)_8]\cos\{8\omega t\} + \ldots \quad (2.13)$$

where $(L_P)_0$ is the magnitude of the DC component and $(L_P)_2$, $(L_P)_4$ $(L_P)_6$ and $(L_P)_8$ are the peak values of the 2nd, 4th, 6th and 8th harmonic components of the self inductance respectively.

$$L_{MP}(\omega,t) = [(L_{MP})_0] + [(L_{MP})_2]\cos\{2\omega t\} + [(L_{MP})_4]\cos\{4\omega t\} + [(L_{MP})_6]\cos\{6\omega t\} + [(L_{MP})_8]\cos\{8\omega t\} + \ldots \quad (2.14)$$

where $(L_{MP})_0$ is the magnitude of the DC component and $(L_{MP})_2$, $(L_{MP})_4$ $(L_{MP})_6$ and $(L_{MP})_8$ are the peak values of the 2nd, 4th, 6th and 8th harmonic components of the magnetizing inductance respectively.

$$(L_{MP})_0 = (L_P)_0 - L_{lP}\,; \quad (L_{MP})_2 = (L_P)_2\,; \quad (L_{MP})_4 = (L_P)_4\,; \ldots\ldots \quad (2.15)$$

The flux linkage λ_P was obtained by integrating the voltage drop v_X across the primary side's self inductance. Thus dividing λ_P by the magnetizing current i_M yields L_P , as shown in (2.16). Equating (2.13) to (2.16) yields (2.17). By solving (2.17) for different instantaneous values of L_P, the various coefficients of L_P can be determined. Then, using (2.15) the coefficients of L_{MP} can be obtained.

$$\lambda_P = L_P i_M \quad ,so \quad L_P = {}^{\lambda_P}/_{i_M} \quad (2.16)$$

$$\left[\lambda_P/_{i_M}\right]_{\omega t} = [(L_P)_0] + [(L_P)_2]\cos\{2\omega t\} + [(L_P)_4]\cos\{4\omega t\}$$

$$+ [(L_P)_6]\cos\{6\omega t\} + [(L_P)_8]\cos\{8\omega t\} + \ldots \quad (2.17)$$

Due to hysteresis effect the zero-crossings of the magnetizing current waveform are asymmetrical. Thus, the flux linkage waveform is considered as the reference as it is very close to a pure sine wave and its zero crossings are symmetrical. Figure 2.8.a shows the variation of i_M and λ_P over one cycle of the flux linkage. As expected the two waveforms have the same polarity in their respective half cycles, thereby guaranteeing a positive value of the self inductance and hence, the magnetizing inductance. The self inductance waveform obtained by directly dividing λ_P by i_M is shown in Figure 2.8.b. It is clearly evident that the self inductance waveform suffers from unavoidable peaks that tend to infinity near the zero-crossings of the magnetizing current. Thus λ_P cannot be directly obtained in this manner and used for modeling the single-phase transformer. This shows the need for subsequent analysis for obtaining a correct estimate of the self inductance of the transformer.

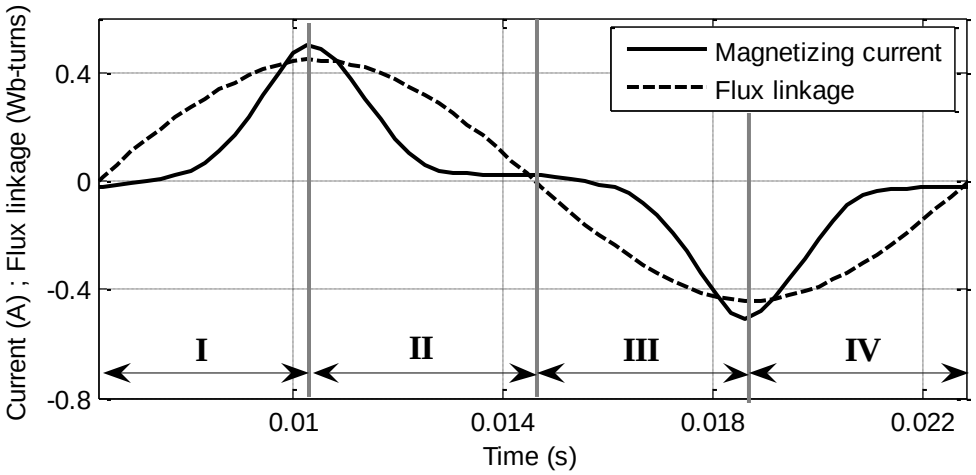

Figure 2.8.a Variation of magnetizing current and flux linkage over one cycle

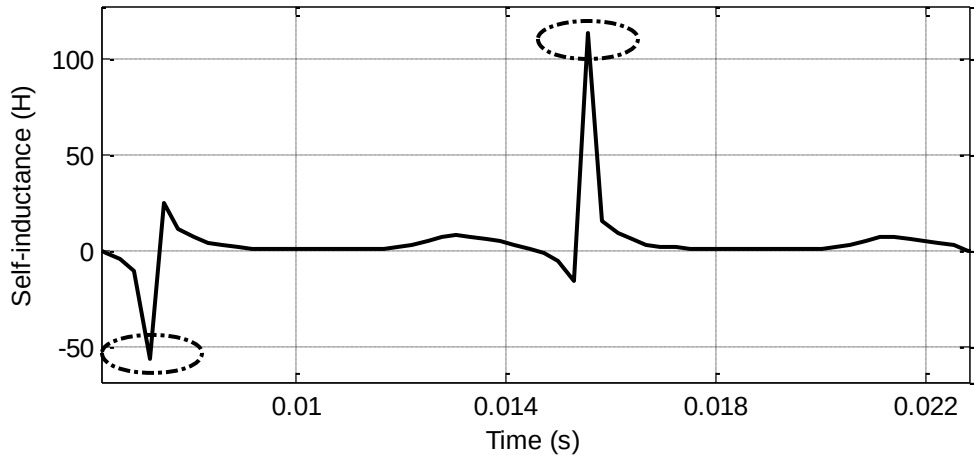

Figure 2.8.b Self inductance waveform obtained from direct division of flux linkage by magnetizing current

From Figure 2.8.a, it is evident that one cycle of flux linkage comprises of four quarter-cycles, which are:

- 1st quarter-cycle (Flux linkage is positive and monotonically increasing)
- 2nd quarter-cycle (Flux linkage is positive and monotonically decreasing)
- 3rd quarter-cycle (Flux linkage is negative and monotonically decreasing)
- 4th quarter-cycle (Flux linkage is negative and monotonically increasing)

At the beginning, computation of the first five coefficients of the self and magnetizing inductances was arbitrarily chosen in modeling the transformer. It will be shown later in the chapter that this choice indeed provides good accuracy. Hence, (2.17) need to be applied to a minimum of five instances of 'ωt' in one quarter-cycle (say the 1st quarter-cycle) to compute these coefficients. To improve the accuracy in computing the inductance coefficients and to capture the saturation level over the full current cycle, five coefficients were computed in the other three quarter cycles as well, and the averages of the four cycles were chosen.

The first zero-crossing of the flux-linkage waveform in the Figure 2.8.a is considered as the reference angular displacement i.e. $\omega t = 0°$. Since the waveforms have been sampled at 3600 Hz; the samples are roughly 6° apart from one another; considering 60 Hz fundamental frequency.

The instantaneous values of the magnetizing current and flux linkage have been recorded for different approximate values of 'ωt'. Tables 2.1 – 2.4 show these recorded values for the four quarter-cycles. Three important considerations have been taken into account, while selecting these five instances –

- It is always a good option to select evenly spaced 'ωt' instances.

- The 'ωt' instances for a particular quarter-cycle have been selected, such that they are distributed throughout the major part of that quarter-cycle.

- Due to hysteresis effect, the slope of the magnetizing current has sudden variations even within one quarter-cycle, especially near the zero-crossings. Thus, only those instances of 'ωt' have been selected for which the slope of the current waveform was approximately constant, i.e. the current was approximately linear.

Approximate angular displacement (ωt)	**Instantaneous values**		
	Flux linkage (in Wb-turns)	**Magnetizing current (in A)**	**Self-inductance (in H)**
36°	0.26984	0.03723	7.24792
48°	0.33521	0.11239	2.98256
60°	0.38931	0.23858	1.63178
72°	0.42931	0.40083	1.07105
84°	0.44600	0.50069	0.89077

Table 2.1 Instantaneous values of flux linkage, magnetizing current and self-inductance for five selected 'ωt' instances in the 1st quarter cycle

Approximate angular displacement (ωt)	Instantaneous values		
	Flux linkage (in Wb-turns)	Magnetizing current (in A)	Self-inductance (in H)
90°	0.44506	0.48809	0.91184
102°	0.43003	0.37403	1.14972
114°	0.39784	0.22628	1.75818
126°	0.34831	0.09991	3.48624
138°	0.28429	0.03846	7.39184

Table 2.2 Instantaneous values of flux linkage, magnetizing current and self-inductance for five selected 'ωt' instances in the 2nd quarter cycle

Approximate angular displacement (ωt)	Instantaneous values		
	Flux linkage (in Wb-turns)	Magnetizing current (in A)	Self-inductance (in H)
210°	-0.23819	-0.02557	9.31521
222°	-0.30733	-0.07943	3.86919
234°	-0.36587	-0.18968	1.92888
246°	-0.41196	-0.33971	1.21268
258°	-0.43828	-0.48499	0.90369

Table 2.3 Instantaneous values of flux linkage, magnetizing current and self-inductance for five selected 'ωt' instances in the 3rd quarter cycle

Approximate angular displacement (ωt)	Instantaneous values		
	Flux linkage (in Wb-turns)	Magnetizing current (in A)	Self-inductance (in H)
270°	-0.43942	-0.48098	0.91359
282°	-0.43340	-0.35808	1.17962
294°	-0.38817	-0.21315	1.82111
306°	-0.33678	-0.09013	3.73660
318°	-0.27099	-0.03685	7.35387

Table 2.4 Instantaneous values of flux linkage, magnetizing current and self-inductance for five selected 'ωt' instances in the 4th quarter cycle

Implementing (2.17) at the five selected 'ωt' instances in each quarter-cycle yields (2.18 – 2.21). The suffixes 'A', 'B', 'C' and 'D' have been used with the self-inductance coefficients for denoting that those coefficients are for the 1st, 2nd, 3rd and 4th quarter-cycles respectively. These equations have been solved for determining the coefficients corresponding to each quarter-cycle, as given in Table 2.5. Also, the average of the coefficients have been computed and shown in this table. These values have been deemed to be the final estimate of the coefficients of self-inductance.

$$\begin{bmatrix}[(L_P)_0]_A\\ [(L_P)_2]_A\\ [(L_P)_4]_A\\ [(L_P)_6]_A\\ [(L_P)_8]_A\end{bmatrix} = \begin{bmatrix}1 & \cos(72°) & \cos(144°) & \cos(216°) & \cos(288°)\\ 1 & \cos(96°) & \cos(192°) & \cos(288°) & \cos(384°)\\ 1 & \cos(120°) & \cos(240°) & \cos(360°) & \cos(480°)\\ 1 & \cos(144°) & \cos(288°) & \cos(432°) & \cos(576°)\\ 1 & \cos(168°) & \cos(336°) & \cos(504°) & \cos(672°)\end{bmatrix}^{-1} \begin{bmatrix}7.24792\\ 2.98256\\ 1.63178\\ 1.07105\\ 0.89077\end{bmatrix} \quad (2.18)$$

$$\begin{bmatrix}[(L_P)_0]_B\\ [(L_P)_2]_B\\ [(L_P)_4]_B\\ [(L_P)_6]_B\\ [(L_P)_8]_B\end{bmatrix} = \begin{bmatrix}1 & \cos(180°) & \cos(360°) & \cos(540°) & \cos(720°)\\ 1 & \cos(204°) & \cos(408°) & \cos(612°) & \cos(816°)\\ 1 & \cos(228°) & \cos(456°) & \cos(684°) & \cos(912°)\\ 1 & \cos(252°) & \cos(504°) & \cos(756°) & \cos(1008°)\\ 1 & \cos(276°) & \cos(552°) & \cos(828°) & \cos(1104°)\end{bmatrix}^{-1} \begin{bmatrix}0.91184\\ 1.14972\\ 1.75818\\ 3.48624\\ 7.39184\end{bmatrix} \quad (2.19)$$

$$\begin{bmatrix}[(L_P)_0]_C\\ [(L_P)_2]_C\\ [(L_P)_4]_C\\ [(L_P)_6]_C\\ [(L_P)_8]_C\end{bmatrix} = \begin{bmatrix}1 & \cos(420°) & \cos(840°) & \cos(1260°) & \cos(1680°)\\ 1 & \cos(444°) & \cos(888°) & \cos(1332°) & \cos(1776°)\\ 1 & \cos(468°) & \cos(936°) & \cos(1404°) & \cos(1872°)\\ 1 & \cos(492°) & \cos(984°) & \cos(1476°) & \cos(1968°)\\ 1 & \cos(516°) & \cos(1032°) & \cos(1548°) & \cos(2064°)\end{bmatrix}^{-1} \begin{bmatrix}9.31521\\ 3.86919\\ 1.92888\\ 1.21268\\ 0.90369\end{bmatrix}$$

(2.20)

$$\begin{bmatrix}[(L_P)_0]_D\\ [(L_P)_2]_D\\ [(L_P)_4]_D\\ [(L_P)_6]_D\\ [(L_P)_8]_D\end{bmatrix} = \begin{bmatrix}1 & \cos(540°) & \cos(1080°) & \cos(1620°) & \cos(2160°)\\ 1 & \cos(564°) & \cos(1128°) & \cos(1692°) & \cos(2256°)\\ 1 & \cos(588°) & \cos(1176°) & \cos(1764°) & \cos(2352°)\\ 1 & \cos(612°) & \cos(1224°) & \cos(1836°) & \cos(2448°)\\ 1 & \cos(636°) & \cos(1272°) & \cos(1908°) & \cos(2544°)\end{bmatrix}^{-1} \begin{bmatrix}0.91359\\ 1.17962\\ 1.82111\\ 3.73660\\ 7.35387\end{bmatrix}$$

(2.21)

Self inductance coefficients	**Inductance values (H)**				
	1st quarter-cycle	**2nd quarter-cycle**	**3rd quarter-cycle**	**4th quarter-cycle**	**Average value**
$(L_P)_0$	10.3246	6.7993	8.4345	2.3267	6.9713
$(L_P)_2$	14.6279	6.7113	11.6912	-1.1954	7.9588
$(L_P)_4$	7.1429	0.0419	5.6634	-5.0783	1.9425
$(L_P)_6$	2.4249	-1.2941	1.9406	-3.4267	-0.0888
$(L_P)_8$	0.4647	-0.5121	0.3852	-0.9569	-0.1548

Table 2.5 Computation of the final estimates of the coefficients of self-inductance

Finally using (2.15) and the known value of L_{lP}, the final estimates of the coefficients of magnetizing inductance have been determined as in (2.18).

$$(L_{MP})_0 = 6.9679\ H; \quad (L_{MP})_2 = 7.9588\ H; \quad (L_{MP})_4 = 1.9425\ H; \quad (L_{MP})_6 = -0.0888\ H; \quad (L_{MP})_8 = -0.1548\ H$$

(2.18)

Using these coefficients in (2.14), the magnetizing inductance has been represented as an infinite series of trigonometric terms as in (2.19), which can incorporate any desired number of higher order saturation related harmonics. The time derivative of L_{MP} is given in (2.20).

$$L_{MP}(\omega, t) = [6.9679] + [7.9588]\cos\{2\omega t\} + [1.9425]\cos\{4\omega t\} + [-0.0888]\cos\{6\omega t\} + [-0.1548]\cos\{8\omega t\} \quad (2.19)$$

$$\frac{dL_{MP}}{dt} = -[7.9588][2\omega]\sin\{2\omega t\} - [1.9425][4\omega]\sin\{4\omega t\} - [-0.0888][6\omega]\sin\{6\omega t\} - [-0.1548][8\omega]\sin\{8\omega t\} \quad (2.20)$$

Figure 2.9 shows the computed magnetizing inductance and its derivative along with the magnetizing current. The magnetizing inductance and its derivative are then used in an equivalent coupled inductive circuit based state-space model of the single-phase transformer for simulating the transformer under different load conditions.

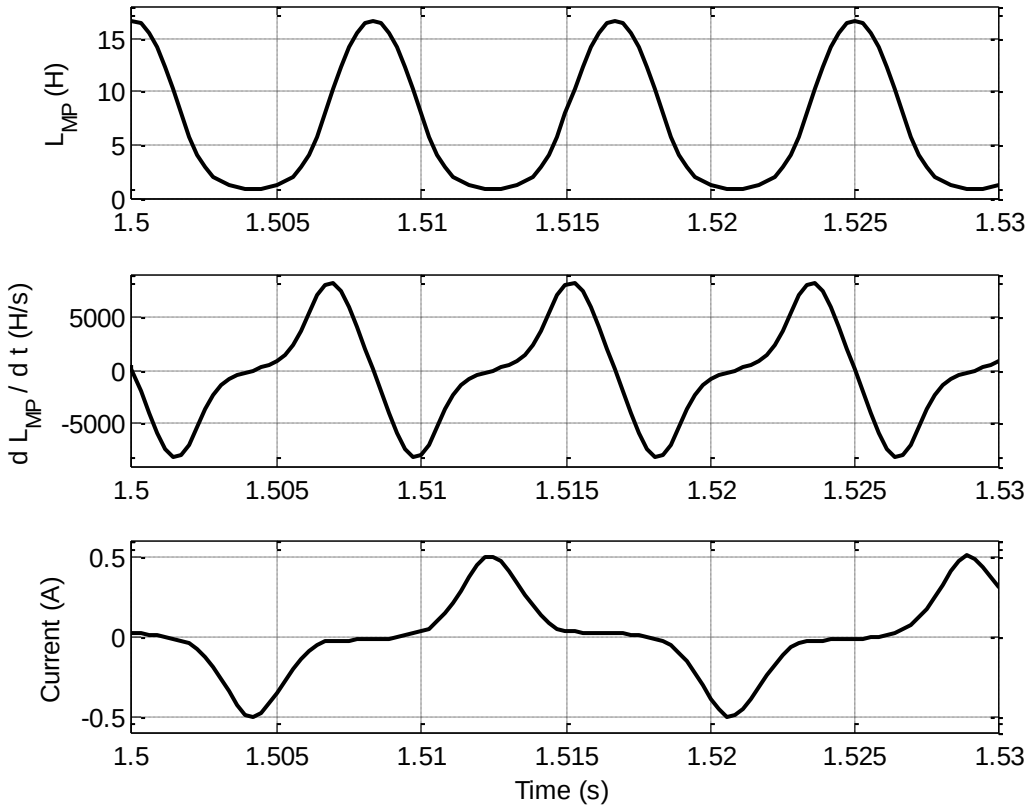

Figure 2.9 (Top to bottom) – Computed magnetizing inductance, time derivative of computed magnetizing inductance and magnetizing current

2.3.2 Simulation of the transformer model under healthy state using the computed magnetizing inductance

Equivalent coupled inductive circuit based state-space models of single-phase and three-phase transformers have been presented in [16]. In this thesis work, a similar state-space model of single-phase transformers has been used for all the simulations. The coupled inductive circuit for a single-phase transformer connected to a purely resistive load is shown in Figure 2.10. The primary and secondary winding currents are given by i_P and i_S respectively, while N_P and N_S represent the number of turns in the primary and secondary windings respectively. The primary line current is i_L , which is the sum of i_P and the core-loss current i_C . The load resistance is R_L .

The main feature of this coupled inductive circuit is the representation of the time-dependent magnetizing inductances corresponding to the primary and secondary sides as L_{MP} and L_{MS} respectively, where these two quantities are related to each other by (2.21).

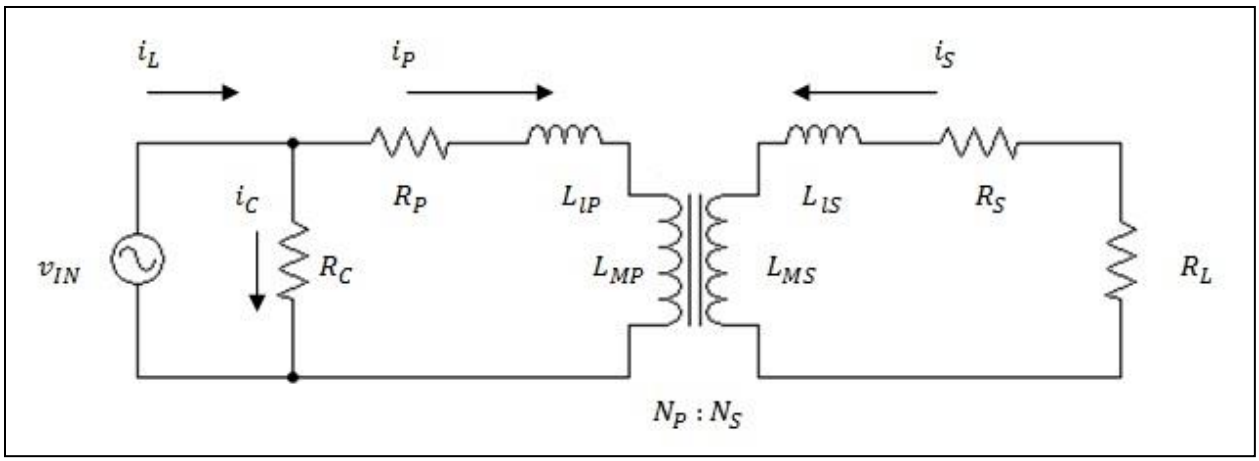

Figure 2.10 Equivalent coupled inductive circuit of a single-phase transformer, supplying an R load

$$\frac{L_{MP}}{L_{MS}} = \left(\frac{N_P}{N_S}\right)^2 \tag{2.21}$$

2.3.2.1 Model for no-load operation under healthy state

This is the simplest operating condition, as the state-space model is comprised of only one state variable which is the magnetizing current. The primary side had been already represented by (2.9), which has been rearranged as (2.22).

$$v_{IN} = i_M \left[R_P + \frac{dL_{MP}}{dt}\right] + \frac{di_M}{dt}\left[L_{MP} + L_{lP}\right] \tag{2.22}$$

Finally, the derived model has been shown in (2.23), which conforms to the standard state-space model given by (2.24).

$$\left(\frac{di_M}{dt}\right) = \left[L_{lP} + L_{MP}\right]^{-1}\left[-\left(R_P + \frac{dL_{MP}}{dt}\right)\right](i_M) + \left[L_{lP} + L_{MP}\right]^{-1}[v_{IN}] \tag{2.23}$$

$$(\dot{x}) = [A](x) + [B][u] \tag{2.24}$$

The computed magnetizing inductance and its derivative given by (2.19) and (2.20) respectively, have been substituted in the state-space model of (2.22), which is then solved in MATLAB environment using the 'ode23tb' solver for 5s using a time-step of 1/3600th of a second. Equation (2.25) shows the voltage input fed to the simulation program in MATLAB, where f is the voltage supply frequency of 60 Hz.

$$v_{IN}(t) = \left(120\sqrt{2}\right)\cos(\omega t) = \left(120\sqrt{2}\right)\cos(2\pi f t) \tag{2.25}$$

The core-loss current i_C given in (2.10), is then added to the simulated magnetizing current for obtaining the simulated exciting current, as shown in (2.26).

$$i_E(t) = i_M(t) + \frac{v_{IN}(t)}{R_C} \tag{2.26}$$

Figure 2.11 shows a comparative plot of the simulated and experimentally acquired exciting currents. The RMS values of the simulated and experimentally acquired exciting currents were found out to be 233.63 mA and 234.56 mA respectively. Thus the percentage error is only 0.396 %. Also, the simulated and experimental waveforms look very similar. Therefore, it is clear that the model is very accurate.

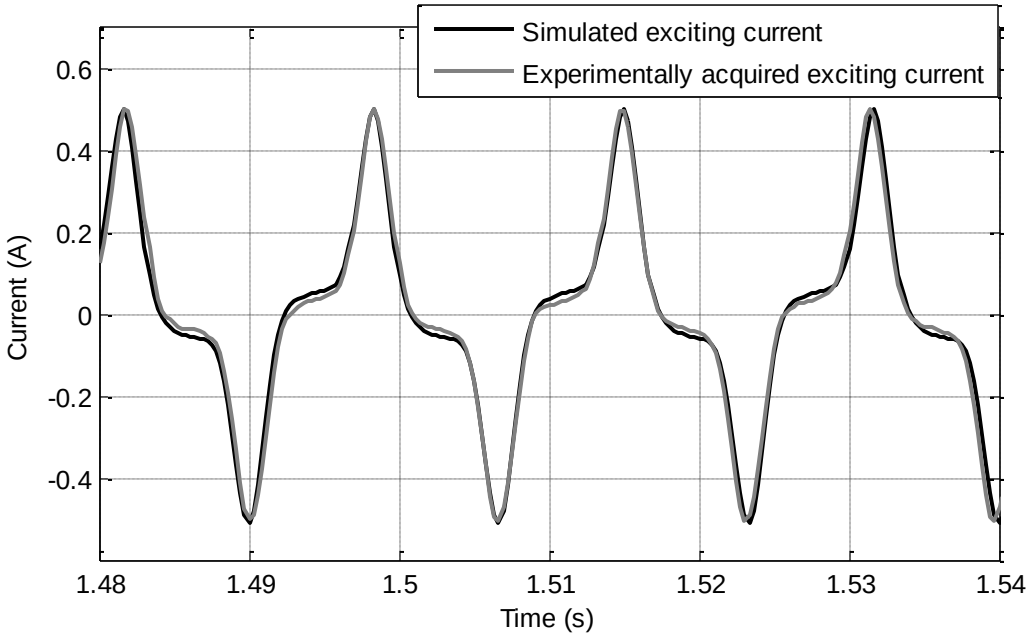

Figure 2.11 Comparison of simulated and experimentally acquired exciting currents under no-load

2.3.2.2 Model for on-load (R type) operation under healthy state

Under a unity power factor resistive load R_L, the primary side of the single-phase transformer has been represented by (2.27), where $i_S{}'$ is the secondary winding current referred to the primary side as in (2.28). Similarly, the secondary side of the transformer has been represented using (2.29). Here, $i_P{}'$ is the primary winding current referred to the secondary side as in (2.30). The final state-space model of the transformer has been derived from (2.27 – 2.30) and is given by (2.31). This model comprises of two state variables which are the primary and secondary winding currents.

$$v_{IN} = (i_P R_P) + L_{lP}\left(\frac{di_P}{dt}\right) + \frac{d}{dt}(L_{MP} i_P + L_{MP} i_S{}') \tag{2.27}$$

$$v_{IN} = (i_P R_P) + L_{lP}\left(\frac{di_P}{dt}\right) + \frac{d}{dt}\left(L_{MP} i_P + L_{MP}\left(\frac{N_S}{N_P}\right) i_S\right) \tag{2.28}$$

$$0 = (i_S R_S) + L_{lS}\left(\frac{di_S}{dt}\right) + \frac{d}{dt}(L_{MS} i_S + L_{MS} i_P{}') + (i_S R_L) \tag{2.29}$$

$$0 = (i_S R_S) + L_{lS}\left(\frac{di_S}{dt}\right) + \frac{d}{dt}\left(L_{MS} i_S + L_{MS}\left(\frac{N_P}{N_S}\right) i_P\right) + (i_S R_L) \tag{2.30}$$

$$\begin{pmatrix} \frac{di_P}{dt} \\ \frac{di_S}{dt} \end{pmatrix} = \begin{bmatrix} L_{lP} + L_{MP} & \left(\frac{N_S}{N_P}\right) L_{MP} \\ \left(\frac{N_P}{N_S}\right) L_{MS} & L_{lS} + L_{MS} \end{bmatrix}^{-1} \begin{bmatrix} -\left(R_P + \frac{dL_{MP}}{dt}\right) & -\left(\frac{N_S}{N_P}\right)\left(\frac{dL_{MP}}{dt}\right) \\ -\left(\frac{N_P}{N_S}\right)\left(\frac{dL_{MS}}{dt}\right) & -\left(R_S + R_L + \frac{dL_{MS}}{dt}\right) \end{bmatrix} \begin{pmatrix} i_P \\ i_S \end{pmatrix} + \begin{bmatrix} L_{lP} + L_{MP} & \left(\frac{N_S}{N_P}\right) L_{MP} \\ \left(\frac{N_P}{N_S}\right) L_{MS} & L_{lS} + L_{MS} \end{bmatrix}^{-1} \begin{bmatrix} v_{IN} \\ 0 \end{bmatrix} \tag{2.31}$$

The model in (2.31) has been simulated for full-load (R type) condition ($R_L = 96\ \Omega$) Here also the core-loss current i_C has been added to the simulated primary winding current i_P to obtain the primary line current i_L . Then the exciting current has been obtained using (2.32). N_P and N_S were known to be 261 and 269 respectively, from the datasheet provided by the manufacturer [71]. In its absence the nominal voltage ratios can be used from the nameplate data. Figure 2.12 shows a comparative plot of the simulated and experimentally acquired exciting currents. The simulated exciting current had a RMS value of 236.89 mA, whereas that for the experimental exciting current for this particular type of load was 228.4 mA. Thus the simulated exciting current had only 3.72 % error in its RMS value.

$$i_E = (i_P + i_C) - i_S{}' = i_L - \left(\frac{N_S}{N_P}\right) i_S \tag{2.32}$$

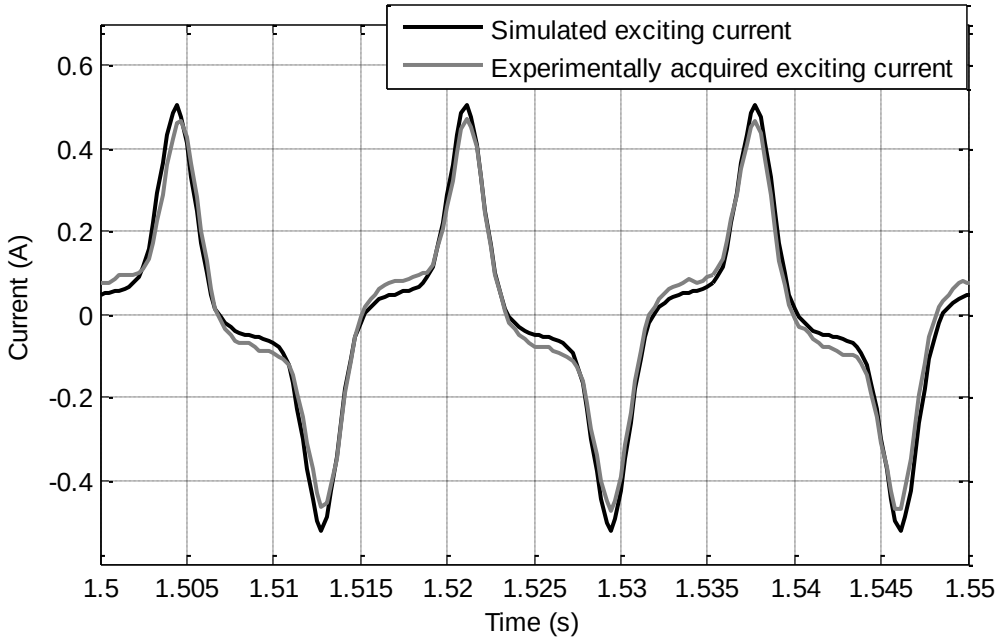

Figure 2.12 Comparison of simulated and experimentally acquired exciting currents under R type full-load

Figures 2.13 and 2.14 provide comparative plots of the simulated primary and secondary line currents with the experimentally acquired ones. The RMS values of the experimentally acquired primary and secondary line currents were found out to be 1.34 A and 1.26 A respectively. On the other hand, the simulated primary and secondary line currents had RMS values of 1.32 A and 1.22 A respectively. This meant that the simulated primary and secondary line currents had percentage errors of only 1.49 % and 3.17 % respectively in their RMS values, with respect to their experimentally acquired counter-parts.

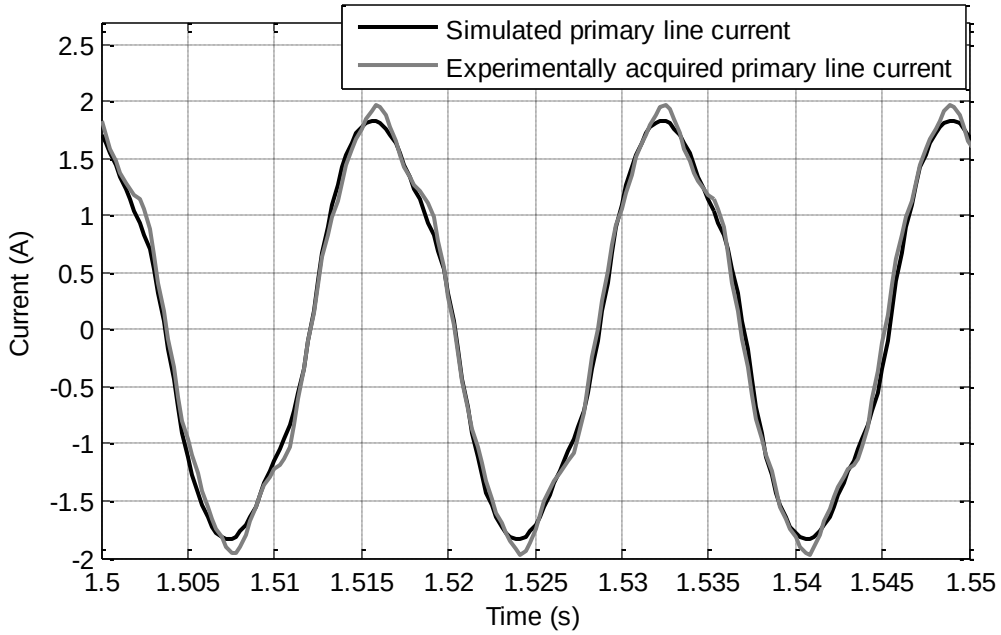

Figure 2.13 Comparison of simulated and experimentally acquired primary line currents under R type full-load

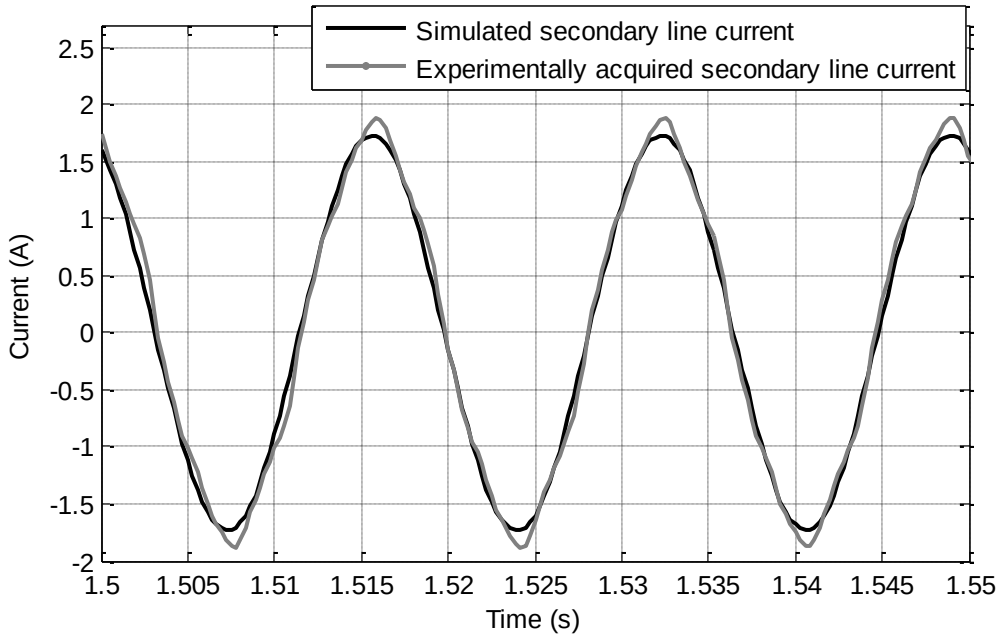

Figure 2.14 Comparison of simulated and experimentally acquired secondary line currents under R type full-load

2.3.2.3 Model for on-load (RL type) operation under healthy state

When connected to a RL load (R_L , the load resistance in series with L_L , the load inductance), the transformer primary side circuit equation remained same as in the previous case, while the secondary side circuit has been represented by (2.33). From these equations, the state-space model has been derived easily following similar steps as before. The model as given by (2.34), has been simulated with R_L and L_L being equal to 76.8 Ω and 152.80 mH respectively.

$$0 = (i_S R_S) + L_{lS}\left(\frac{di_S}{dt}\right) + \frac{d}{dt}(L_{MS} i_S + L_{MS} i_P{}') + (i_S R_L) + L_L\left(\frac{di_S}{dt}\right) \tag{2.33}$$

$$\begin{pmatrix} \frac{di_P}{dt} \\ \frac{di_S}{dt} \end{pmatrix} = \begin{bmatrix} L_{lP} + L_{MP} & \left(\frac{N_S}{N_P}\right) L_{MP} \\ \left(\frac{N_P}{N_S}\right) L_{MS} & L_{lS} + L_L + L_{MS} \end{bmatrix}^{-1} \begin{bmatrix} -\left(R_P + \frac{dL_{MP}}{dt}\right) & -\left(\frac{N_S}{N_P}\right)\left(\frac{dL_{MP}}{dt}\right) \\ -\left(\frac{N_P}{N_S}\right)\left(\frac{dL_{MS}}{dt}\right) & -\left(R_S + R_L + \frac{dL_{MS}}{dt}\right) \end{bmatrix} \begin{pmatrix} i_P \\ i_S \end{pmatrix}$$

$$+ \begin{bmatrix} L_{lP} + L_{MP} & \left(\frac{N_S}{N_P}\right) L_{MP} \\ \left(\frac{N_P}{N_S}\right) L_{MS} & L_{lS} + L_L + L_{MS} \end{bmatrix}^{-1} \begin{bmatrix} v_{IN} \\ 0 \end{bmatrix}$$

(2.34)

Figure 2.15 shows a comparative plot of the simulated and experimentally acquired exciting currents. For this case also, the simulated exciting current was obtained using (2.32). The RMS value of the simulated exciting current was found to be 231.27 mA, whereas that for the experimental exciting current for this particular type of load was 229.80 mA. Thus, the simulated exciting current had only 0.64 % error in its RMS value.

The comparative plots for the simulated and experimentally acquired primary and secondary line currents have been provided in Figures 2.16 and 2.17 respectively. The RMS values of the experimentally acquired primary and secondary line currents for this particular type of load were found out to be 1.34 A and 1.17 A respectively. So, with RMS values of 1.41 A and 1.21 A, the simulated primary and secondary line currents had percentage errors of 5.22 % and 3.42 % respectively with respect to their experimentally acquired counter-parts.

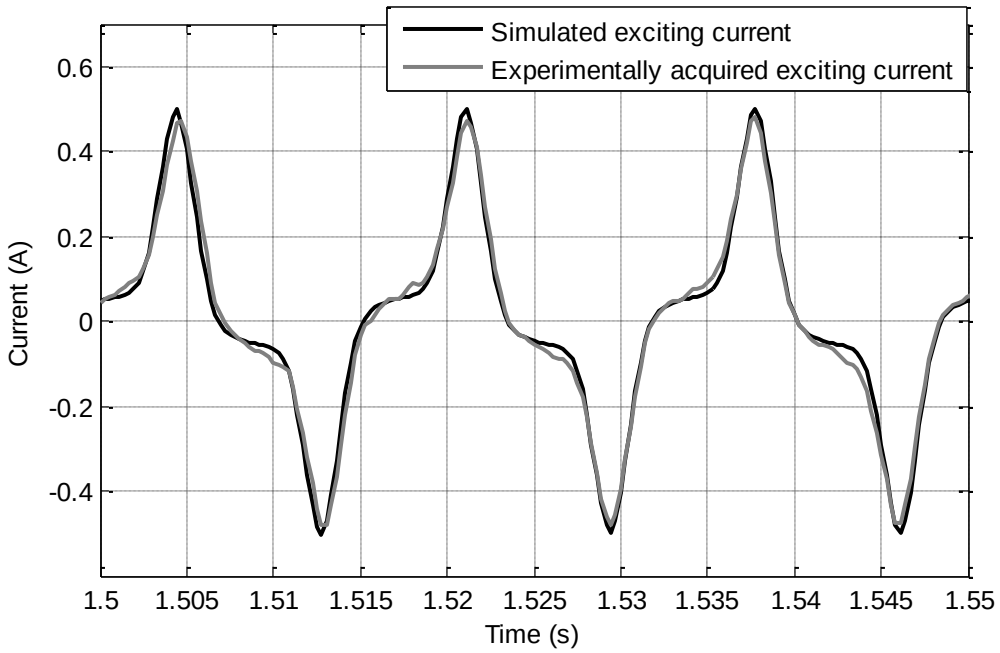

Figure 2.15 Comparison of simulated and experimentally acquired exciting currents under RL type full-load

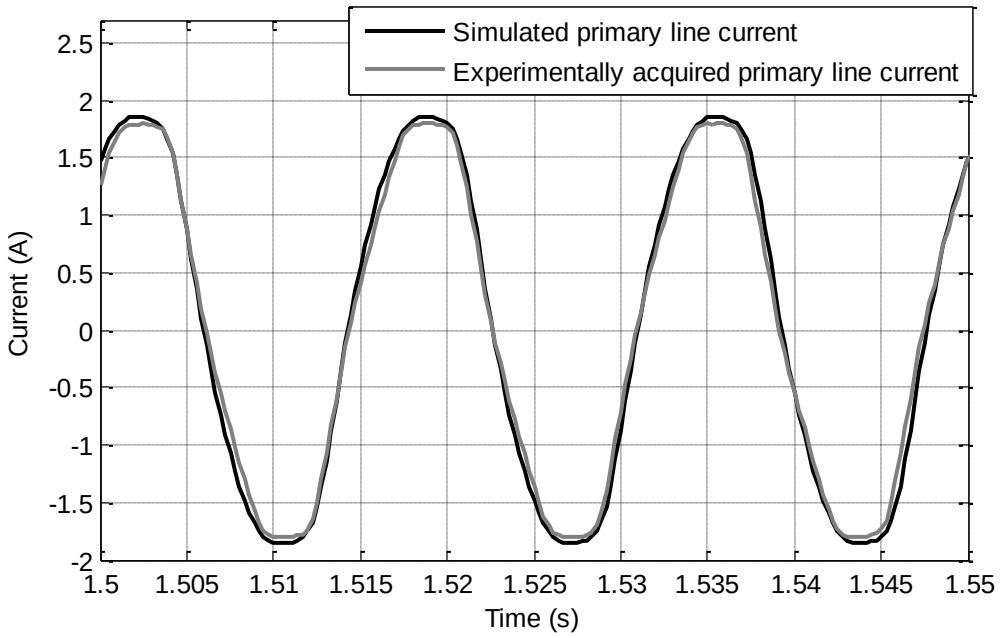

Figure 2.16 Comparison of simulated and experimentally acquired primary line currents under RL type full-load

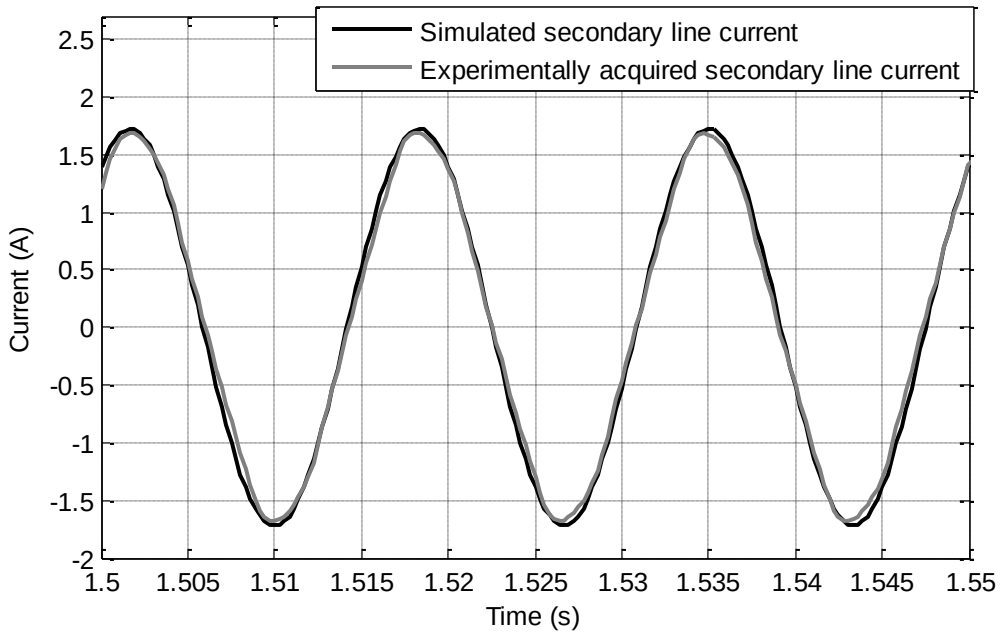

Figure 2.17 Comparison of simulated and experimentally acquired secondary line currents under RL type full-load

2.3.2.4 Model for on-load (RC type) operation under healthy state

For simulating the transformer under RC load (R_L , the load resistance in series with C_L , the load capacitance), an additional state-variable has to be incorporated in the state-space model. It is the voltage drop v_{C_L} across the load capacitance C_L . The primary side circuit equation here also remained same, while the secondary side circuit has been represented by (2.35). The additional state-variable has also been accounted for, using (2.36). Finally, based on these equations the state-space model has been derived as shown in (2.37). The model has been simulated with R_L and C_L being equal to 76.8 Ω and 46.05 µF respectively.

$$0 = (i_S R_S) + L_{lS}\left(\frac{di_P}{dt}\right) + \frac{d}{dt}(L_{MS} i_S + L_{MS} i_P{}') + (i_S R_L) + v_{C_L} \tag{2.35}$$

$$\left(\frac{dv_{C_L}}{dt}\right) = \left(\frac{1}{C_L}\right) i_S \tag{2.36}$$

$$\begin{pmatrix} \frac{di_P}{dt} \\ \frac{di_S}{dt} \\ \frac{dv_{C_L}}{dt} \end{pmatrix} = \begin{bmatrix} L_{lP} + L_{MP} & \left(\frac{N_S}{N_P}\right) L_{MP} & 0 \\ \left(\frac{N_P}{N_S}\right) L_{MS} & L_{lS} + L_{MS} & 0 \\ 0 & 0 & 1 \end{bmatrix}^{-1} \begin{bmatrix} -\left(R_P + \frac{dL_{MP}}{dt}\right) & -\left(\frac{N_S}{N_P}\right)\left(\frac{dL_{MP}}{dt}\right) & 0 \\ -\left(\frac{N_P}{N_S}\right)\left(\frac{dL_{MS}}{dt}\right) & -\left(R_S + R_L + \frac{dL_{MS}}{dt}\right) & -1 \\ 0 & \frac{1}{C_L} & 0 \end{bmatrix} \begin{pmatrix} i_P \\ i_S \\ v_{C_L} \end{pmatrix}$$

$$+ \begin{bmatrix} L_{lP} + L_{MP} & \left(\frac{N_S}{N_P}\right) L_{MP} & 0 \\ \left(\frac{N_P}{N_S}\right) L_{MS} & L_{lS} + L_{MS} & 0 \\ 0 & 0 & 1 \end{bmatrix}^{-1} \begin{bmatrix} v_{IN} \\ 0 \\ 0 \end{bmatrix} \tag{2.37}$$

Figure 2.18 shows a comparative plot of the simulated and experimentally acquired exciting currents. For this case also, the simulated exciting current was obtained using (2.32). The RMS value of the simulated exciting current was 236.54 mA, whereas that for the experimental exciting current for this particular type of load was 232.40 mA. Thus the simulated exciting current had only 1.78 % error in its RMS value.

The RMS values of the experimentally acquired primary and secondary line currents for this particular type of load were found out to be 1.21 A and 1.24 A respectively. The simulated and experimentally acquired line currents have been compared in Figures 2.19 and 2.20. With RMS values of 1.23 A and 1.25 A, the simulated primary and secondary line currents had percentage errors of only 1.65 % and 0.81 % respectively with respect to their experimentally acquired counter-parts.

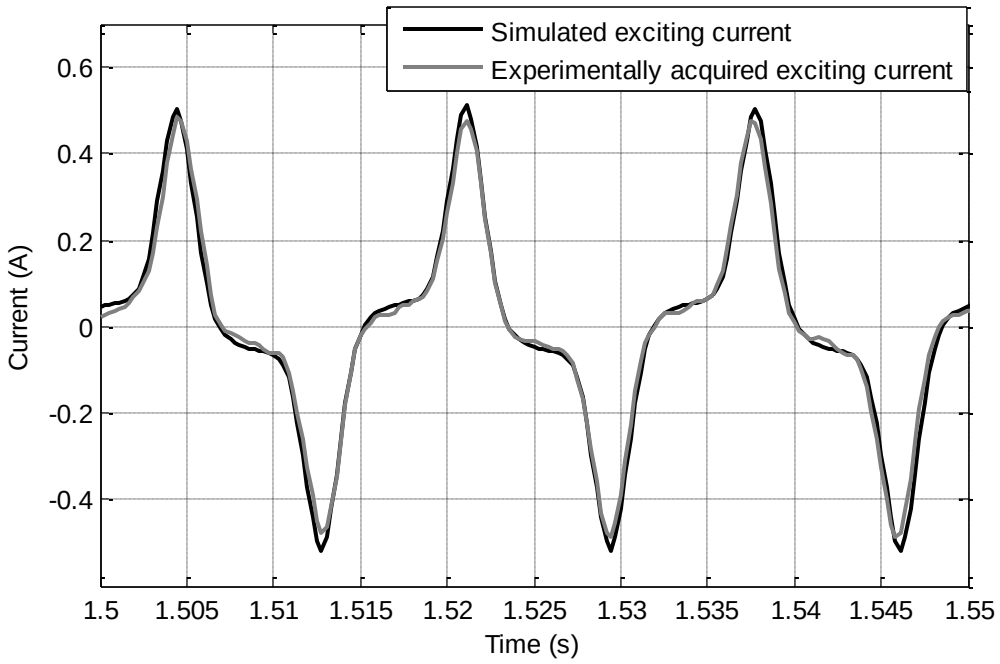

Figure 2.18 Comparison of simulated and experimentally acquired exciting currents under RC type full-load

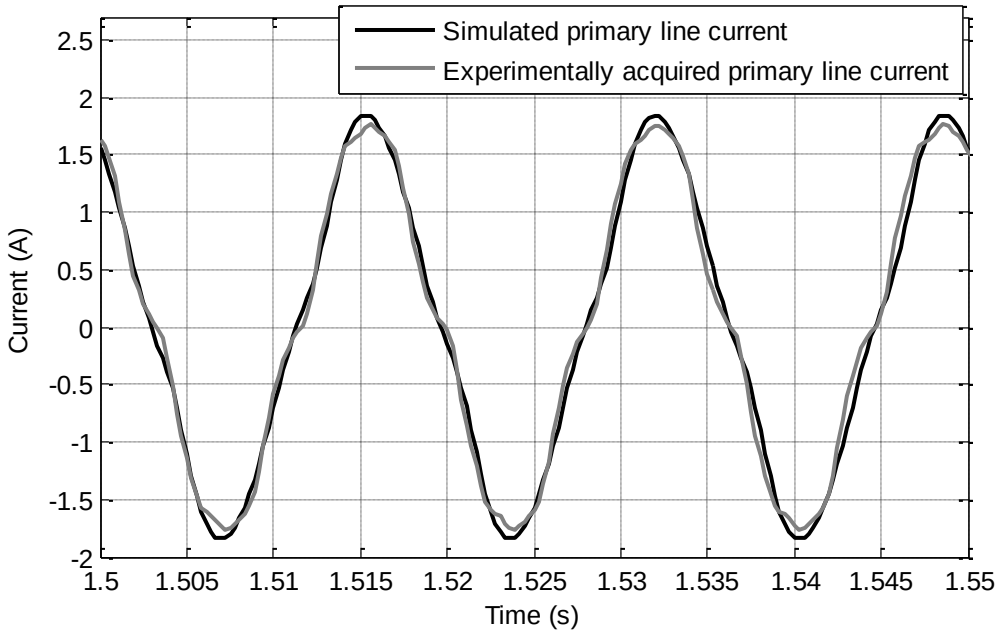

Figure 2.19 Comparison of simulated and experimentally acquired primary line currents under RC type full-load

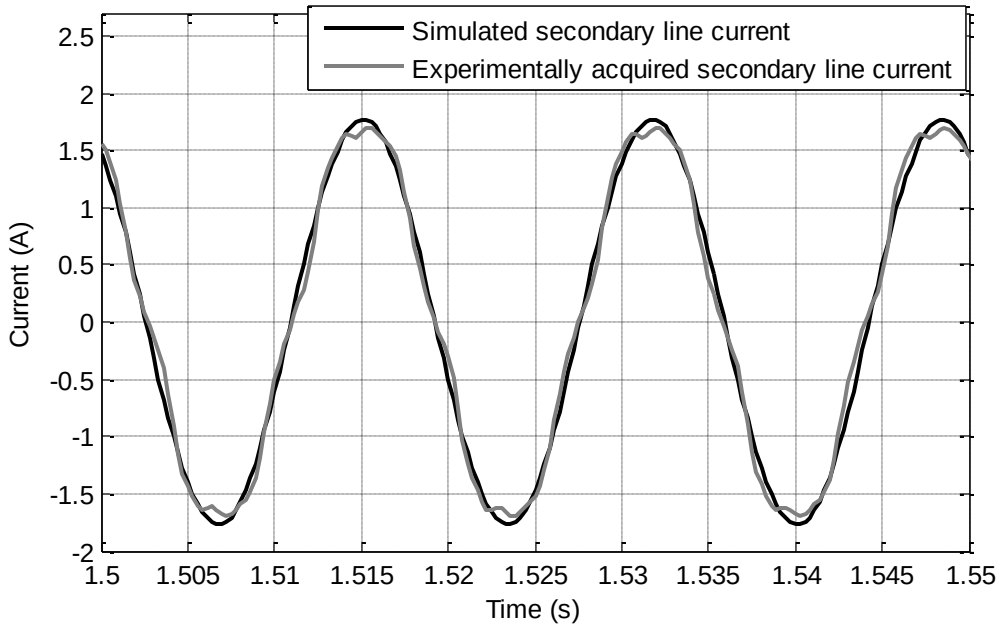

Figure 2.20 Comparison of simulated and experimentally acquired primary line currents under RC type full-load

2.3.3 Discussion on the accuracy of the simulation results

Three important points need to be considered regarding the differences obtained between the simulation and experimental results. First, the experiments were conducted with the transformer being fed from the laboratory's power supply which already had some higher order voltage harmonics. Second, the frequency of the utility was not exactly 60 Hz. Third, the level and power factor of the loads connected to the transformer during the experiments were not exactly same as their theoretical values because of the availability of only customer-made load modules (resistor, inductor and capacitor modules) in the laboratory. These facts definitely have contributed, though by a small amount, to the percentage errors between the simulated and experimental primary line, secondary line and exciting currents. Hence, keeping the three factors discussed above in mind, the model is deemed to be reasonably accurate in modeling the real-life behavior of the transformer under no-load and full-load operation with unity, lagging and leading power factor loads connected. Not only there is close resemblance between all the experimental and simulated currents, but also the errors in their RMS values are mostly within about 3 %. Table

2.6 summarizes the simulation and experimental results, showing the percentage errors in their RMS values as well.

Operating condition	**Current**		**RMS values**	**Percentage errors**
No-load	Exciting	Simulated	233.63 mA	0.396 %
		Experimental	234.56 mA	
Full load R type	Exciting	Simulated	236.89 mA	3.72 %
		Experimental	228.40 mA	
	Primary line	Simulated	1.32 A	1.49 %
		Experimental	1.34 A	
	Secondary line	Simulated	1.22 A	3.17 %
		Experimental	1.26 A	
Full load RL type	Exciting	Simulated	231.27 mA	0.64 %
		Experimental	229.80 mA	
	Primary line	Simulated	1.41 A	5.22 %
		Experimental	1.34 A	
	Secondary line	Simulated	1.21 A	3.42 %
		Experimental	1.17 A	
Full load RC type	Exciting	Simulated	236.54 mA	1.78 %
		Experimental	232.40 mA	
	Primary line	Simulated	1.23 A	1.65 %
		Experimental	1.21 A	
	Secondary line	Simulated	1.25 A	0.81 %
		Experimental	1.24 A	

Table 2.6 Comparison of simulation and experimental results

All simulations in this subsection have been presented for healthy operating condition of the single-phase transformer. In the next Chapter, the coupled inductance based state-space model

has been modified for simulating the transformer under faulty condition i.e. when it is affected by inter-turn short circuit fault in one of its winding.

Chapter 3

Detection of Inter-turn Winding Faults in Single-phase Transformers – Simulation Results

In this chapter, a scheme for the diagnosis of inter-turn winding faults in single-phase transformers has been proposed. The scheme is based on the analysis of harmonic content in the exciting current of the transformer under healthy and faulty conditions. The scheme has been shown to reliably detect incipient stages of inter-turn winding faults such as a single-turn short-circuit fault, under no-load as well as loaded conditions. Simulations have been carried out for fault detection under different levels and types of load; and the results have been presented to substantiate the theoretical analysis.

3.1. Introduction to the proposed fault detection scheme

The exciting current of single-phase transformers is non-sinusoidal in nature even for a sinusoidal voltage supply because of the non-linear properties of silicon steel. This indicates the presence of higher order, saturation related harmonics in the exciting current even under healthy operating condition of the transformer. Flux density and saturation level in the transformer core are two essential factors affecting the RMS value and harmonic content of the exciting current [38, 39]. Occurrence of inter-turn winding faults in transformers affects the flux density and core saturation around the faulty region, hence affecting the exciting current as well. Thus, the proposed fault detection technique is based on the changes in the harmonics of the exciting current of transformers under the occurrence of internal winding faults. Another advantage of the exciting current based fault detection is that it works independent of the level and type of load connected to the transformer.

3.1.1. Theoretical background of the fault detection scheme

It was shown in [73] that the fundamental flux linkage component of a transformer does not change in the presence of an inter-turn winding short circuit. It was demonstrated by shorting 1.5 % of the turns on primary side. The short did not result in any voltage change at the secondary terminal of the transformer. Thus, neglecting the local saturation effects in the neighbourhood of the shorted turns, it can be said that the magnetic characteristics and hence, the saturation and hysteresis levels of the transformer core do not get affected by small number of short circuited turns. This means that the harmonics of transformer magnetizing current also remain unchanged when this type of fault occurs. However, in order to compensate for the decrease in fundamental flux linkage caused by the shorted turns, an equivalent fundamental current component must flow in the primary winding. If $(i_M)_1$ is the fundamental magnetizing current in the healthy transformer, then for N_F number of shorted turns with fault current i_F on the secondary side, the new magnetizing current will be given by (3.1). For a similar fault on the primary side the new magnetizing current will be given by (3.2).

$$[\,(i_M)_1]_{fS} = \left(\frac{N_P\,(i_M)_1 + N_F i_F}{N_P}\right) \tag{3.1}$$

$$[\,(i_M)_1]_{fP} = \left(\frac{N_P\,(i_M)_1 + N_F i_F}{N_P - N_F}\right) \tag{3.2}$$

Thus the Total Harmonic Distortion (THD) of the magnetizing current and hence, that of exciting current given by (3.3), will decrease with inter-turn short circuit fault in a transformer as outlined by (3.4). In (3.3), $(I_E)_1$ and $(I_E)_h$ represent the RMS values of the fundamental and other higher-order harmonic components in the exciting current respectively, with h being the higher-order harmonic number.

$$(THD)_{i_E} = \sqrt{\sum_{h=2}^{\infty} (I_E)_h{}^2} \Big/ (I_E)_1 \tag{3.3}$$

$$[(THD)_{i_E}]_{HEALTHY} > [(THD)_{i_E}]_{FAULTY} \tag{3.4}$$

At the beginning, peak values of up to the 15th harmonic in the exciting current have been arbitrary considered for computing the corresponding THDs. It will be shown later in the chapter, that this choice provides good accuracy in the THD computations and hence, in the detection of the inter-turns winding faults. Since $[\ (i_M)_1]_{fP}$ is greater than $[\ (i_M)_1]_{fS}$ from (3.1) and (3.2), the magnetizing and exciting currents' THDs will decrease more for a fault in the primary than that in secondary.

The exciting current can be obtained from the primary and secondary line currents, following (2.32) from the previous chapter. i_L represents the primary line current, which is the sum of primary winding current i_P and core-loss current i_C . On the other hand, the secondary line current is equal to the secondary winding current itself and is given by i_S . If the turns ratio is not known, then the nominal voltage ratio obtained from the nameplate data of the single-phase transformer can be used. However, it will lead to some inaccuracy. This is shown in (3.5) where V_P and V_S represents nominal RMS values of primary and secondary line voltages respectively.

$$i_E = i_L - \left(\frac{N_S}{N_P}\right) i_S \approx i_L - \left(\frac{V_S}{V_P}\right) i_S \tag{3.5}$$

It has been also shown in [5, 6, 7, 73 and 74] that the changes in RMS value and harmonic content of the primary input voltage are quite small in case of inter-turn winding faults. Still any changes in the primary line voltage harmonics during the fault will affect the harmonics in the exciting current, irrespective of however small the changes are. Thus for increasing the robustness of the proposed fault detection scheme, the THD of the single-phase transformer's primary line voltage is monitored as well, as will be shown in Chapter 4.

3.1.2. Salient features of the fault detection scheme

The proposed fault detection technique has several advantages, which are:

- **Non-invasive –** The methodology is simple and does not require physical access to any parts inside the transformer casing or tank. It requires the measurements of only the terminal quantities like the line currents and voltage.

- **Cost-effective –** The only apparatus required for implementing this scheme are current and voltage sensors along with a relatively inexpensive data acquisition system for analysis of acquired waveforms leading to fault detection.

- **Flexibility in application –** The scheme can be used for fault detection in dry-type as well as oil-filled single-phase transformers, since it is completely non-invasive. Apart from that, it can be implemented on transformers which are newly installed as well the ones operating for a long period of time. Also, the scheme can be implemented irrespective of the type and level of load connected to the transformer

- **Quick on-site implementation –** Fault detection can be done on-site without isolating the transformer from the load and that also, within a short span of time. The fault detection technique however, does not incorporate the effect of stray losses and inter-winding capacitances which are characteristic of large power transformers (around tens to hundreds of kVA of power rating and a few to several hundreds of kV of voltage rating). Thus, the proposed technique is best suited for fault diagnosis in smaller rating (within a few kVA and a few kV), single-phase distribution transformers, where inter-turn capacitances are negligible.

3.2. Modeling of single-phase transformer under faulty state

In the previous chapter, detailed modeling and simulation of the single-phase 150 VA, 120/120 V shell-type laboratory transformer under healthy state operating with different level and type of loads have been presented. In this subsection, similar models have been derived for the same transformer but under faulty state. It has been shown in [12, 73 and 74] that inter-turn winding faults at the extremities of a transformer winding are most difficult to detect as the changes in the primary line and exciting currents are minimum. Such behavior occurs due to higher concentration of the electromagnetic flux lines near the axial centre of a transformer winding as compared to that near the two ends of it. Flux lines are curved near the winding extremities where the core limbs meet the yoke segments; whereas the flux lines are more concentrated near

the axial center of the windings [73]. Thus according to Faraday's Law, the higher concentration of flux lines near the axial center of a transformer winding leads to the circulation of higher fault current if an inter-turn winding fault develops there. Understandably, the fault current generated in case of inter-turn faults developing near the winding extremities are comparatively smaller. Thus, for such faults the increase in the primary line current and hence, the increase in the exciting current are also slightly smaller.

In case of a fault at one extremity of the transformer winding, the affected winding can be considered as two parts:

- One, which is shorted and can be represented by a closed-loop circuit comprising of the winding resistance and leakage inductance corresponding to the number of turns shorted.
- And the other, which is un-shorted. It is the healthy part of the winding and is connected to the load (if the fault is on the secondary side) or the source (if the fault is on the primary side).

However, if the inter-turn fault occurs anywhere between the two extremities of the winding, then the two healthy parts of the winding (one on either side of the short-circuited turns) can be considered together as one single healthy sub-winding while the shorted turns can be dealt with separately. The healthy sub-winding can be connected to the load (if the fault is on the secondary side) or the source (if the fault is on the primary side). Such an analytical modeling technique will not be able to accurately replicate the curvature of electromagnetic flux lines near the extremities of a winding and hence, incorporate the slight increase in the fault current in case of winding faults near the axial center of the winding. But for our fault detection purpose, this modeling technique has been deemed accurate enough, as will be seen in the simulation results presented later in this chapter. However, for more accurate representation of the electromagnetic flux in the transformer core during an inter-turn winding fault, Finite-Element based models can be employed as in [73]; but the models cannot be used for real-time fault diagnosis due to their extremely long simulation times.

In this chapter, coupled inductive circuit based transformer models have been derived for inter-turn faults in both the primary and secondary windings. The magnetizing inductance L_{MP} and its derivative $\frac{dL_{MP}}{dt}$ given by (2.19) and (2.20) respectively in the previous chapter can be

substituted in these models for simulating the transformer under faulty state. Under such a condition, the shorted part of the winding acts as a separate short-circuited tertiary winding [16].

3.2.1 Transformer model with inter-turn winding fault on the secondary side

The equivalent coupled inductive circuit model of the single-phase transformer under healthy state connected to a purely resistive load has already been illustrated in Figure 2.10 of the previous chapter. The model for a similar transformer under an inter-turn short circuit fault in the secondary winding is given in Figure 3.1. Although the transformer in the figure is shown delivering power to a purely resistive load (with load resistance R_L); the same model can be used for RL and RC loads as well by replacing the resistor with a series connected R and L or R and C. With a fault in the secondary winding, the circuit for the primary side remains unchanged with N_P turns, R_P as winding resistance, L_{lP} as leakage inductance and L_{MP} as equivalent magnetizing inductance. i_P , i_C and i_L are the primary winding current, core-loss current and primary line current respectively. It is already known that the primary line current is the sum of the core-loss current and primary winding current.

N_{SX} is the number of turns in the healthy part of the secondary winding and it is related to the total turns on the secondary side N_S and the number of shorted turns N_F as per (3.6). The winding resistance and leakage inductance in the healthy part of the secondary winding are given by R_{SX} and L_{lSX} respectively whereas the magnetizing inductance corresponding to the healthy part of the secondary winding is given by L_{MSX} . These quantities can be obtained from their corresponding values under healthy state, as per (3.7). i_{SX} is the current in the healthy part of the secondary winding and is basically the load current in this case.

Similarly, the shorted part of the secondary winding comprising of N_F turns has an equivalent winding resistance and leakage inductance of R_F and L_{lF} respectively. The magnetizing inductance corresponding to the shorted winding is given by L_{MF}. They are related to their corresponding secondary side quantities by (3.8). i_F is the fault current flowing through the shorted circuit. Since the impedance in the shorted winding is very small, i_F generally is quite high as compared to the rated secondary current.

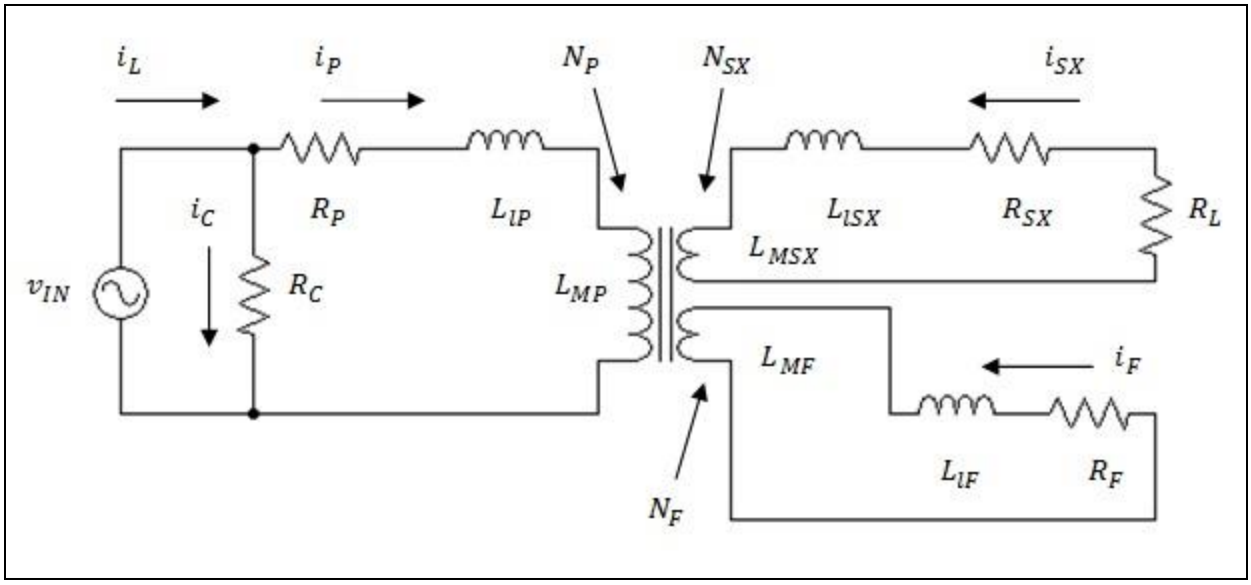

Figure 3.1 Equivalent coupled inductive circuit of a single-phase transformer with inter-turn short circuit fault in the secondary winding, supplying an R load.

$$N_{SX} = N_S - N_F \tag{3.6}$$

$$R_{SX} = R_S\left(\frac{N_{SX}}{N_S}\right) \quad ; \quad L_{lSX} = L_{lS}\left(\frac{N_{SX}}{N_S}\right)^2 \quad ; \quad L_{MSX} = L_{MS}\left(\frac{N_{SX}}{N_S}\right)^2 \tag{3.7}$$

$$R_F = R_S\left(\frac{N_F}{N_S}\right) \quad ; \quad L_{lF} = L_{lS}\left(\frac{N_F}{N_S}\right)^2 \quad ; \quad L_{MF} = L_{MS}\left(\frac{N_F}{N_S}\right)^2 \tag{3.8}$$

3.2.1.1 Model for no-load operation under faulty state – Fault on secondary side

This is the simplest operating condition under faulty state of the transformer, as the state-space model comprises of only two state variables: magnetizing current on the primary side and fault current in the shorted winding. Under this condition, the primary winding current i_P is same as the magnetizing current i_M , as shown in (3.9). The primary side circuit is represented by (3.10), where $i_F{}'$ is the fault current referred to primary side as in (3.11). Similarly the shorted winding is described by (3.12), where $i_M{}''$ is the magnetizing current referred to the shorted winding, as in (3.13). The final model is derived from (3.10 – 3.13) in matrix form as given by (3.14).

$$i_P = i_M \tag{3.9}$$

Primary winding:

$$v_{IN} = (i_M R_P) + L_{lP}\left(\frac{di_M}{dt}\right) + \frac{d}{dt}(L_{MP} i_M + L_{MP} i_F{}') \tag{3.10}$$

$$or, \quad v_{IN} = (i_M R_P) + L_{lP}\left(\frac{di_M}{dt}\right) + \frac{d}{dt}\left(L_{MP} i_M + L_{MP}\left(\frac{N_F}{N_P}\right) i_F\right) \tag{3.11}$$

Secondary winding, faulty part:

$$0 = (i_F R_F) + L_{lF}\left(\frac{di_F}{dt}\right) + \frac{d}{dt}(L_{MF} i_F + L_{MF} i_M{}'') \tag{3.12}$$

$$or, \quad 0 = (i_F R_F) + L_{lF}\left(\frac{di_F}{dt}\right) + \frac{d}{dt}\left(L_{MF} i_F + \left(\frac{N_P}{N_F}\right) i_M\right) \tag{3.13}$$

$$\begin{pmatrix} \frac{di_M}{dt} \\ \frac{di_F}{dt} \end{pmatrix} = \begin{bmatrix} L_{lP} + L_{MP} & \left(\frac{N_F}{N_P}\right) L_{MP} \\ \left(\frac{N_P}{N_F}\right) L_{MF} & L_{lF} + L_{MF} \end{bmatrix}^{-1} \begin{bmatrix} -\left(R_P + \frac{dL_{MP}}{dt}\right) & -\left(\frac{N_F}{N_P}\right)\left(\frac{dL_{MP}}{dt}\right) \\ -\left(\frac{N_P}{N_F}\right)\left(\frac{dL_{MF}}{dt}\right) & -\left(R_F + \frac{dL_{MF}}{dt}\right) \end{bmatrix} \begin{pmatrix} i_M \\ i_F \end{pmatrix} + \begin{bmatrix} L_{lP} + L_{MP} & \left(\frac{N_F}{N_P}\right) L_{MP} \\ \left(\frac{N_P}{N_F}\right) L_{MF} & L_{lF} + L_{MF} \end{bmatrix}^{-1} \begin{bmatrix} v_{IN} \\ 0 \end{bmatrix} \tag{3.14}$$

Once the magnetizing current is estimated from the above model of (3.14), the core-loss current is added to it in order to obtain the simulated exciting current under faulty state. This is done in the same way as for the transformer in healthy state and is shown in (3.15).

$$i_{E,f} = i_M + i_C = i_M + \left(\frac{v_{IN}}{R_C}\right) \tag{3.15}$$

3.2.1.2 Model for on-load (R type) operation under faulty state – Fault on secondary side

Under this condition, the primary side is represented by (3.16), where $i_{SX}{}'$ is the current in the healthy part of the secondary winding referred to the primary side, as in (3.17). Equation (3.18) represents the circuit for the healthy part of the secondary winding which is connected to the load. $i_P{}'$ and $i_F{}''$ are the primary winding current and fault current referred to this healthy part of secondary winding, as in (3.19). The shorted winding is further represented by (3.20), where $i_{SX}{}''$ is the current in the healthy part of the secondary winding referred to the shorted winding as in (3.21). Similarly, $i_P{}''$ represents the primary winding current referred to the shorted winding. The final state-space model is derived from (3.16 – 3.21) and is given by (3.22).

Primary winding:

$$v_{IN} = (i_P R_P) + L_{lP}\left(\frac{di_P}{dt}\right) + \frac{d}{dt}(L_{MP} i_P + L_{MP} i_{SX}{}' + L_{MP} i_F{}') \tag{3.16}$$

$$or, \quad v_{IN} = (i_P R_P) + L_{lP}\left(\frac{di_P}{dt}\right) + \frac{d}{dt}\left(L_{MP} i_P + L_{MP}\left(\frac{N_{SX}}{N_P}\right) i_{SX} + L_{MP}\left(\frac{N_F}{N_P}\right) i_F\right) \tag{3.17}$$

Secondary winding, healthy part:

$$0 = (i_{SX} R_{SX}) + L_{lSX}\left(\frac{di_{SX}}{dt}\right) + \frac{d}{dt}(L_{MSX} i_{SX} + L_{MSX} i_P{}' + L_{MSX} i_F{}'') + (i_{SX} R_L) \tag{3.18}$$

$$or, \quad 0 = (i_{SX} R_{SX}) + L_{lSX}\left(\frac{di_{SX}}{dt}\right) + \frac{d}{dt}\left(L_{MSX} i_{SX} + L_{MSX}\left(\frac{N_P}{N_{SX}}\right) i_P + L_{MSX}\left(\frac{N_F}{N_{SX}}\right) i_F\right) + (i_{SX} R_L) \tag{3.19}$$

Secondary winding, faulty part:

$$0 = (i_F R_F) + L_F\left(\frac{di_F}{dt}\right) + \frac{d}{dt}(L_{MF} i_F + L_{MF} i_P{}'' + L_{MF} i_{SX}{}'') \tag{3.20}$$

$$or, \qquad 0 = (i_F R_F) + L_F\left(\frac{di_F}{dt}\right) + \frac{d}{dt}\left(L_{MF} i_F + L_{MF}\left(\frac{N_P}{N_F}\right) i_P + L_{MF}\left(\frac{N_{SX}}{N_F}\right) i_{SX}\right) \tag{3.21}$$

$$\begin{pmatrix} \frac{di_P}{dt} \\ \frac{di_{SX}}{dt} \\ \frac{di_F}{dt} \end{pmatrix} = \begin{bmatrix} L_{lP} + L_{MP} & \left(\frac{N_{SX}}{N_P}\right) L_{MP} & \left(\frac{N_F}{N_P}\right) L_{MP} \\ \left(\frac{N_P}{N_{SX}}\right) L_{MSX} & L_{lSX} + L_{MSX} & \left(\frac{N_F}{N_{SX}}\right) L_{MSX} \\ \left(\frac{N_P}{N_F}\right) L_{MF} & \left(\frac{N_{SX}}{N_F}\right) L_{MF} & L_{lF} + L_{MF} \end{bmatrix}^{-1}$$

$$\begin{bmatrix} -\left(R_P + \frac{dL_{MP}}{dt}\right) & -\left(\frac{N_{SX}}{N_P}\right)\left(\frac{dL_{MP}}{dt}\right) & -\left(\frac{N_F}{N_P}\right)\left(\frac{dL_{MP}}{dt}\right) \\ -\left(\frac{N_P}{N_{SX}}\right)\left(\frac{dL_{MSX}}{dt}\right) & -\left(R_{SX} + R_L + \frac{dL_{MSX}}{dt}\right) & -\left(\frac{N_F}{N_{SX}}\right)\left(\frac{dL_{MSX}}{dt}\right) \\ -\left(\frac{N_P}{N_F}\right)\left(\frac{dL_{MF}}{dt}\right) & -\left(\frac{N_{SX}}{N_F}\right)\left(\frac{dL_{MF}}{dt}\right) & -\left(R_F + \frac{dL_{MF}}{dt}\right) \end{bmatrix} \begin{pmatrix} i_P \\ i_{SX} \\ i_F \end{pmatrix}$$

$$+ \begin{bmatrix} L_{lP} + L_{MP} & \left(\frac{N_{SX}}{N_P}\right) L_{MP} & \left(\frac{N_F}{N_P}\right) L_{MP} \\ \left(\frac{N_P}{N_{SX}}\right) L_{MSX} & L_{lSX} + L_{MSX} & \left(\frac{N_F}{N_{SX}}\right) L_{MSX} \\ \left(\frac{N_P}{N_F}\right) L_{MF} & \left(\frac{N_{SX}}{N_F}\right) L_{MF} & L_{lF} + L_{MF} \end{bmatrix}^{-1} \begin{bmatrix} v_{IN} \\ 0 \\ 0 \end{bmatrix}$$

(3.22)

Here also, the core-loss current is added to the simulated primary winding current in order to obtain the simulated primary line current under faulty state. Then, the secondary current referred to the primary side is subtracted from the primary line current for computing the exciting current under faulty state. This is done in the same way as for the transformer under healthy state and is shown in (3.23).

$$i_{E,f} = (i_P + i_C) - i_{SX}{}' = i_L - \left(\frac{N_{SX}}{N_P}\right) i_{SX} \tag{3.23}$$

3.2.1.3 Model for on-load (RL type) operation under faulty state – Fault on secondary side

When connected to a RL load (R_L , the load resistance in series with L_L , the load inductance), the equations for the transformer's primary side and the faulty winding remained same as in the previous case, while the secondary side circuit has been represented by (3.24). From these, the state-space model is derived as in (3.25) and the exciting current is then obtained by (3.23).

$$0 = (i_{SX}R_{SX}) + L_{lSX}\left(\frac{di_{SX}}{dt}\right) + \frac{d}{dt}(L_{MSX}i_{SX} + L_{MSX}i_P{}' + L_{MSX}i_F{}'') + (i_{SX}R_L) + L_L\left(\frac{di_{SX}}{dt}\right)$$

(3.24)

$$\begin{pmatrix} \frac{di_P}{dt} \\ \frac{di_{SX}}{dt} \\ \frac{di_F}{dt} \end{pmatrix} = \begin{bmatrix} L_{lP} + L_{MP} & \left(\frac{N_{SX}}{N_P}\right)L_{MP} & \left(\frac{N_F}{N_P}\right)L_{MP} \\ \left(\frac{N_P}{N_{SX}}\right)L_{MSX} & L_{lSX} + L_L + L_{MSX} & \left(\frac{N_F}{N_{SX}}\right)L_{MSX} \\ \left(\frac{N_P}{N_F}\right)L_{MF} & \left(\frac{N_{SX}}{N_F}\right)L_{MF} & L_{lF} + L_{MF} \end{bmatrix}^{-1}$$

$$\begin{bmatrix} -\left(R_P + \frac{dL_{MP}}{dt}\right) & -\left(\frac{N_{SX}}{N_P}\right)\left(\frac{dL_{MP}}{dt}\right) & -\left(\frac{N_F}{N_P}\right)\left(\frac{dL_{MP}}{dt}\right) \\ -\left(\frac{N_P}{N_{SX}}\right)\left(\frac{dL_{MSX}}{dt}\right) & -\left(R_{SX} + R_L + \frac{dL_{MSX}}{dt}\right) & -\left(\frac{N_F}{N_{SX}}\right)\left(\frac{dL_{MSX}}{dt}\right) \\ -\left(\frac{N_P}{N_F}\right)\left(\frac{dL_{MF}}{dt}\right) & -\left(\frac{N_{SX}}{N_F}\right)\left(\frac{dL_{MF}}{dt}\right) & -\left(R_F + \frac{dL_{MF}}{dt}\right) \end{bmatrix} \begin{pmatrix} i_P \\ i_{SX} \\ i_F \end{pmatrix}$$

$$+ \begin{bmatrix} L_{lP} + L_{MP} & \left(\frac{N_{SX}}{N_P}\right)L_{MP} & \left(\frac{N_F}{N_P}\right)L_{MP} \\ \left(\frac{N_P}{N_{SX}}\right)L_{MSX} & L_{lSX} + L_L + L_{MSX} & \left(\frac{N_F}{N_{SX}}\right)L_{MSX} \\ \left(\frac{N_P}{N_F}\right)L_{MF} & \left(\frac{N_{SX}}{N_F}\right)L_{MF} & L_{lF} + L_{MF} \end{bmatrix}^{-1} \begin{bmatrix} v_{IN} \\ 0 \\ 0 \end{bmatrix}$$

(3.25)

3.2.1.4 Model for on-load (RC) operation under faulty state – Fault on secondary side

When the transformer is connected to a RC load (R_L , the load resistance in series with C_L , the load capacitance), equations for the primary side of the transformer and its faulty winding remain same. The secondary side circuit has been represented by (3.26). An additional state-variable, which is the voltage drop v_{C_L}across the load capacitance C_L , has been represented by (3.27). The final model is given by (3.28). Here also, the exciting current is obtained using (3.23).

$$0 = (i_{SX}R_{SX}) + L_{lSX}\left(\frac{di_{SX}}{dt}\right) + \frac{d}{dt}(L_{MSX}i_{SX} + L_{MSX}i_P{}' + L_{MSX}i_F{}'') + (i_{SX}R_L) + v_{C_L} \quad (3.26)$$

$$\left(\frac{dv_{C_L}}{dt}\right) = \left(\frac{1}{C_L}\right)i_{SX} \quad (3.27)$$

$$\begin{pmatrix} \frac{di_P}{dt} \\ \frac{di_{SX}}{dt} \\ \frac{di_F}{dt} \\ \frac{dv_{C_L}}{dt} \end{pmatrix} = \begin{bmatrix} L_{lP}+L_{MP} & \left(\frac{N_{SX}}{N_P}\right)L_{MP} & \left(\frac{N_F}{N_P}\right)L_{MP} & 0 \\ \left(\frac{N_P}{N_{SX}}\right)L_{MSX} & L_{lSX}+L_{MSX} & \left(\frac{N_F}{N_{SX}}\right)L_{MSX} & 0 \\ \left(\frac{N_P}{N_F}\right)L_{MF} & \left(\frac{N_{SX}}{N_F}\right)L_{MF} & L_{lF}+L_{MF} & 0 \\ 0 & 0 & 0 & 1 \end{bmatrix}^{-1}$$

$$\begin{bmatrix} -\left(R_P + \frac{dL_{MP}}{dt}\right) & -\left(\frac{N_{SX}}{N_P}\right)\left(\frac{dL_{MP}}{dt}\right) & -\left(\frac{N_F}{N_P}\right)\left(\frac{dL_{MP}}{dt}\right) & 0 \\ -\left(\frac{N_P}{N_{SX}}\right)\left(\frac{dL_{MSX}}{dt}\right) & -\left(R_{SX}+R_L+\frac{dL_{MSX}}{dt}\right) & -\left(\frac{N_F}{N_{SX}}\right)\left(\frac{dL_{MSX}}{dt}\right) & -1 \\ -\left(\frac{N_P}{N_F}\right)\left(\frac{dL_{MF}}{dt}\right) & -\left(\frac{N_{SX}}{N_F}\right)\left(\frac{dL_{MF}}{dt}\right) & -\left(R_F + \frac{dL_{MF}}{dt}\right) & 0 \\ 0 & \frac{1}{C_L} & 0 & 0 \end{bmatrix} \begin{pmatrix} i_P \\ i_{SX} \\ i_F \\ v_{C_L} \end{pmatrix}$$

$$+ \begin{bmatrix} L_{lP}+L_{MP} & \left(\frac{N_{SX}}{N_P}\right)L_{MP} & \left(\frac{N_F}{N_P}\right)L_{MP} & 0 \\ \left(\frac{N_P}{N_{SX}}\right)L_{MSX} & L_{lSX}+L_{MSX} & \left(\frac{N_F}{N_{SX}}\right)L_{MSX} & 0 \\ \left(\frac{N_P}{N_F}\right)L_{MF} & \left(\frac{N_{SX}}{N_F}\right)L_{MF} & L_{lF}+L_{MF} & 0 \\ 0 & 0 & 0 & 1 \end{bmatrix}^{-1} \begin{bmatrix} v_{IN} \\ 0 \\ 0 \\ 0 \end{bmatrix}$$

(3.28)

3.2.2 Transformer model with inter-turns winding fault on the primary side

In this subsection, an inter-turn winding fault has been modeled on the primary side of the single-phase transformer and all necessary state-space models of the transformer operation under different load conditions have been derived following similar steps as in the previous subsection. Thus, the steps for the derivations have not been explicitly shown here.

The model for a single-phase transformer under an inter-turn short circuit fault at one extremity of the primary winding is shown in Figure 3.3. Although the transformer in the figure is shown delivering power to a purely resistive load (with load resistance R_L); the same model can be used for RL and RC loads as well by replacing the resistor with a series connected R and L or R and C. With a fault in the primary winding, the circuit for the secondary side remains unchanged with N_S turns, R_S as winding resistance, L_{lS} as leakage inductance and L_{MS} as equivalent magnetizing inductance. i_S is the winding current in the secondary side.

N_{PX} is the number of turns in the healthy part of the primary winding and it is related to the total turns on the primary side N_P and the number of shorted turns N_F as per (3.29). The winding resistance and leakage inductance in the healthy part of the primary winding are given by R_{PX} and L_{lPX} respectively whereas the magnetizing inductance corresponding to the healthy part of the primary winding is given by L_{MPX} . These quantities can be obtained from their corresponding values under healthy state, as per (3.30). i_{PX} is the winding current in the healthy part of the primary winding. i_{PX} , when added to the core-loss current i_C gives the primary line current i_L .

Similarly, the shorted part of the primary winding comprising of N_F turns has an equivalent winding resistance and leakage inductance of R_F and L_{lF} respectively. The magnetizing inductance corresponding to shorted winding is given byL_{MF}. These quantities are related to their corresponding primary side quantities by (3.31). i_F is the fault current flowing through the shorted circuit.

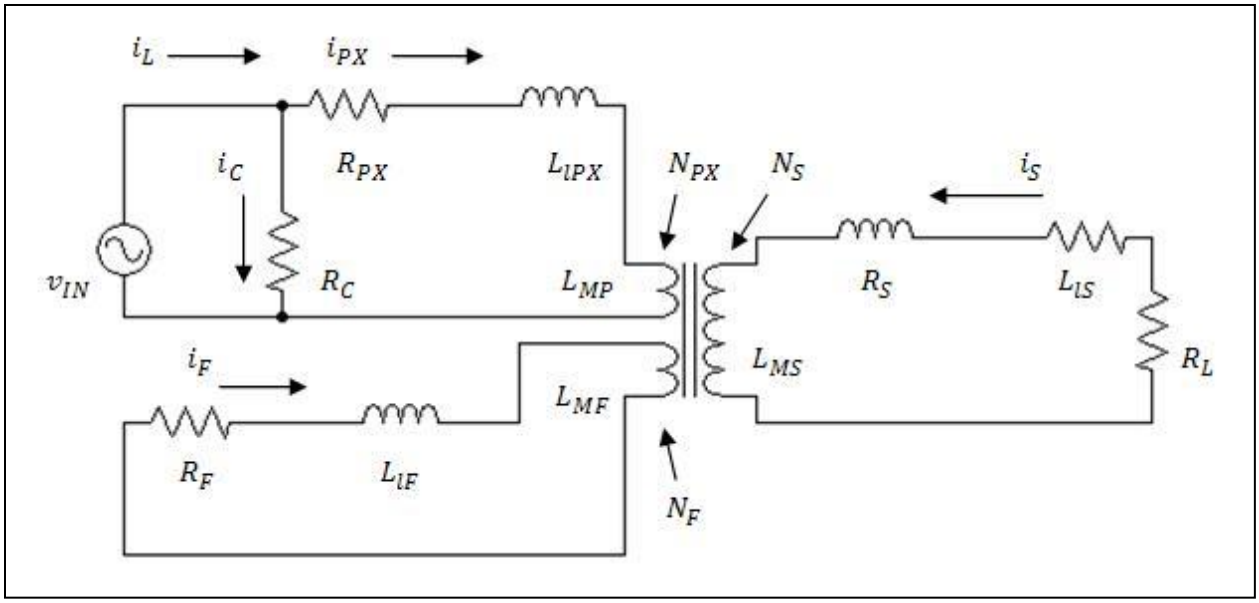

Figure 3.2 Equivalent coupled inductive circuit of a single-phase transformer with inter-turn short circuit fault in the primary winding, supplying an R load.

$$N_{PX} = N_P - N_F \tag{3.29}$$

$$R_{PX} = R_P\left(\frac{N_{PX}}{N_P}\right) \quad ; \quad L_{lPX} = L_{lP}\left(\frac{N_{PX}}{N_P}\right)^2 \quad ; \quad L_{MPX} = L_{MP}\left(\frac{N_{PX}}{N_P}\right)^2 \tag{3.30}$$

$$R_F = R_P\left(\frac{N_F}{N_P}\right) \quad ; \quad L_{lF} = L_{lP}\left(\frac{N_F}{N_P}\right)^2 \quad ; \quad L_{MF} = L_{MP}\left(\frac{N_F}{N_P}\right)^2 \tag{3.31}$$

3.2.2.1 Model for no-load operation under faulty state – Fault on primary side

$$\begin{pmatrix}\frac{di_M}{dt}\\ \frac{di_F}{dt}\end{pmatrix} = \begin{bmatrix} L_{lPX} + L_{MPX} & \left(\frac{N_F}{N_{PX}}\right)L_{MPX} \\ \left(\frac{N_{PX}}{N_F}\right)L_{MF} & L_{lF} + L_{MF}\end{bmatrix}^{-1} \begin{bmatrix} -\left(R_{PX} + \frac{dL_{MPX}}{dt}\right) & -\left(\frac{N_F}{N_{PX}}\right)\left(\frac{dL_{MPX}}{dt}\right) \\ -\left(\frac{N_{PX}}{N_F}\right)\left(\frac{dL_{MF}}{dt}\right) & -\left(R_F + \frac{dL_{MF}}{dt}\right)\end{bmatrix}\begin{pmatrix} i_M \\ i_F\end{pmatrix} + \begin{bmatrix} L_{lPX} + L_{MPX} & \left(\frac{N_F}{N_{PX}}\right)L_{MPX} \\ \left(\frac{N_{PX}}{N_F}\right)L_{MF} & L_{lF} + L_{MF}\end{bmatrix}^{-1} \begin{bmatrix} v_{IN} \\ 0\end{bmatrix} \tag{3.32}$$

3.2.2.2 Model for on-load (R type) operation under faulty state – Fault on primary side

$$\begin{pmatrix} \frac{di_{PX}}{dt} \\ \frac{di_S}{dt} \\ \frac{di_F}{dt} \end{pmatrix} = \begin{bmatrix} L_{lPX} + L_{MPX} & \left(\frac{N_S}{N_{PX}}\right) L_{MPX} & \left(\frac{N_F}{N_{PX}}\right) L_{MPX} \\ \left(\frac{N_{PX}}{N_S}\right) L_{MS} & L_{lS} + L_{MS} & \left(\frac{N_F}{N_S}\right) L_{MS} \\ \left(\frac{N_{PX}}{N_F}\right) L_{MF} & \left(\frac{N_S}{N_F}\right) L_{MF} & L_{lF} + L_{MF} \end{bmatrix}^{-1}$$

$$\begin{bmatrix} -\left(R_{PX} + \frac{dL_{MPX}}{dt}\right) & -\left(\frac{N_S}{N_{PX}}\right)\left(\frac{dL_{MPX}}{dt}\right) & -\left(\frac{N_F}{N_{PX}}\right)\left(\frac{dL_{MPX}}{dt}\right) \\ -\left(\frac{N_{PX}}{N_S}\right)\left(\frac{dL_{MS}}{dt}\right) & -\left(R_S + R_L + \frac{dL_{MS}}{dt}\right) & -\left(\frac{N_F}{N_S}\right)\left(\frac{dL_{MS}}{dt}\right) \\ -\left(\frac{N_{PX}}{N_F}\right)\left(\frac{dL_{MF}}{dt}\right) & -\left(\frac{N_S}{N_F}\right)\left(\frac{dL_{MF}}{dt}\right) & -\left(R_F + \frac{dL_{MF}}{dt}\right) \end{bmatrix} \begin{pmatrix} i_{PX} \\ i_S \\ i_F \end{pmatrix}$$

$$+ \begin{bmatrix} L_{lPX} + L_{MPX} & \left(\frac{N_S}{N_{PX}}\right) L_{MPX} & \left(\frac{N_F}{N_{PX}}\right) L_{MPX} \\ \left(\frac{N_{PX}}{N_S}\right) L_{MS} & L_{lS} + L_{MS} & \left(\frac{N_F}{N_S}\right) L_{MS} \\ \left(\frac{N_{PX}}{N_F}\right) L_{MF} & \left(\frac{N_S}{N_F}\right) L_{MF} & L_{lF} + L_{MF} \end{bmatrix}^{-1} \begin{bmatrix} v_{IN} \\ 0 \\ 0 \end{bmatrix} \tag{3.33}$$

After simulating the model, the exciting current can be obtained from the primary and secondary winding currents, as in (3.34).

$$i_{E,f} = (i_{PX} + i_C) - i_S{}' = i_L - \left(\frac{N_S}{N_{PX}}\right) i_S \tag{3.34}$$

3.2.2.3 Model for on-load (RL type) operation under faulty state – Fault on primary side

This model given by (3.35) is very similar to the one in (3.33), apart from the inclusion of the L_L term, for incorporating the load inductance. The exciting current can be obtained using (3.34) as before.

$$\begin{pmatrix} \frac{di_{PX}}{dt} \\ \frac{di_S}{dt} \\ \frac{di_F}{dt} \end{pmatrix} = \begin{bmatrix} L_{lPX} + L_{MPX} & \left(\frac{N_S}{N_{PX}}\right) L_{MPX} & \left(\frac{N_F}{N_{PX}}\right) L_{MPX} \\ \left(\frac{N_{PX}}{N_S}\right) L_{MS} & L_{lS} + L_{MS} & \left(\frac{N_F}{N_S}\right) L_{MS} \\ \left(\frac{N_{PX}}{N_F}\right) L_{MF} & \left(\frac{N_S}{N_F}\right) L_{MF} & L_{lF} + L_{MF} \end{bmatrix}^{-1}$$

$$\begin{bmatrix} -\left(R_{PX} + \frac{dL_{MPX}}{dt}\right) & -\left(\frac{N_S}{N_{PX}}\right)\left(\frac{dL_{MPX}}{dt}\right) & -\left(\frac{N_F}{N_{PX}}\right)\left(\frac{dL_{MPX}}{dt}\right) \\ -\left(\frac{N_{PX}}{N_S}\right)\left(\frac{dL_{MS}}{dt}\right) & -\left(R_S + R_L + \frac{dL_{MS}}{dt}\right) & -\left(\frac{N_F}{N_S}\right)\left(\frac{dL_{MS}}{dt}\right) \\ -\left(\frac{N_{PX}}{N_F}\right)\left(\frac{dL_{MF}}{dt}\right) & -\left(\frac{N_S}{N_F}\right)\left(\frac{dL_{MF}}{dt}\right) & -\left(R_F + \frac{dL_{MF}}{dt}\right) \end{bmatrix} \begin{pmatrix} i_{PX} \\ i_S \\ i_F \end{pmatrix}$$

$$+ \begin{bmatrix} L_{lPX} + L_{MPX} & \left(\frac{N_S}{N_{PX}}\right) L_{MPX} & \left(\frac{N_F}{N_{PX}}\right) L_{MPX} \\ \left(\frac{N_{PX}}{N_S}\right) L_{MS} & L_{lS} + L_{MS} & \left(\frac{N_F}{N_S}\right) L_{MS} \\ \left(\frac{N_{PX}}{N_F}\right) L_{MF} & \left(\frac{N_S}{N_F}\right) L_{MF} & L_{lF} + L_{MF} \end{bmatrix}^{-1} \begin{bmatrix} v_{IN} \\ 0 \\ 0 \end{bmatrix}$$

(3.35)

3.2.2.4 Model for on-load (RC type) operation under faulty state – Fault on primary side

The final model for this case is given by (3.36). As before, here also the voltage drop v_{C_L} across the load capacitance C_L has to be incorporated as an additional state variable. The exciting current can be obtained similarly using (3.34).

$$\begin{pmatrix} \frac{di_{PX}}{dt} \\ \frac{di_S}{dt} \\ \frac{di_F}{dt} \\ \frac{dv_{C_L}}{dt} \end{pmatrix} = \begin{bmatrix} L_{lPX} + L_{MPX} & \left(\frac{N_S}{N_{PX}}\right) L_{MPX} & \left(\frac{N_F}{N_{PX}}\right) L_{MPX} & 0 \\ \left(\frac{N_{PX}}{N_S}\right) L_{MS} & L_{lS} + L_{MS} & \left(\frac{N_F}{N_S}\right) L_{MS} & 0 \\ \left(\frac{N_{PX}}{N_F}\right) L_{MF} & \left(\frac{N_S}{N_F}\right) L_{MF} & L_{lF} + L_{MF} & 0 \\ 0 & 0 & 0 & 1 \end{bmatrix}^{-1}$$

$$\begin{bmatrix} -\left(R_{PX} + \frac{dL_{MPX}}{dt}\right) & -\left(\frac{N_S}{N_{PX}}\right)\left(\frac{dL_{MPX}}{dt}\right) & -\left(\frac{N_F}{N_{PX}}\right)\left(\frac{dL_{MPX}}{dt}\right) & 0 \\ -\left(\frac{N_{PX}}{N_S}\right)\left(\frac{dL_{MS}}{dt}\right) & -\left(R_S + R_L + \frac{dL_{MS}}{dt}\right) & -\left(\frac{N_F}{N_S}\right)\left(\frac{dL_{MS}}{dt}\right) & -1 \\ -\left(\frac{N_{PX}}{N_F}\right)\left(\frac{dL_{MF}}{dt}\right) & -\left(\frac{N_S}{N_F}\right)\left(\frac{dL_{MF}}{dt}\right) & -\left(R_F + \frac{dL_{MF}}{dt}\right) & 0 \\ 0 & \frac{1}{C_L} & 0 & 0 \end{bmatrix} \begin{pmatrix} i_{PX} \\ i_S \\ i_F \\ v_{C_L} \end{pmatrix}$$

$$+ \begin{bmatrix} L_{lPX} + L_{MPX} & \left(\frac{N_S}{N_{PX}}\right) L_{MPX} & \left(\frac{N_F}{N_{PX}}\right) L_{MPX} & 0 \\ \left(\frac{N_{PX}}{N_S}\right) L_{MS} & L_{lS} + L_{MS} & \left(\frac{N_F}{N_S}\right) L_{MS} & 0 \\ \left(\frac{N_{PX}}{N_F}\right) L_{MF} & \left(\frac{N_S}{N_F}\right) L_{MF} & L_{lF} + L_{MF} & 0 \\ 0 & 0 & 0 & 1 \end{bmatrix}^{-1} \begin{bmatrix} v_{IN} \\ 0 \\ 0 \\ 0 \end{bmatrix}$$

(3.36)

3.3 Inter-turn winding fault detection based on simulation results

This section is dedicated towards demonstrating the application of the proposed fault detection scheme (introduced in the previous section), based on simulation results. The simulations have been performed using the single-phase transformer models for healthy state given by (2.23), (2.31), (2.34) and (2.37) in the previous chapter; models for secondary side faults given by (3.14), (3.22), (3.24) and (3.28); and models for primary side faults given by (3.32), (3.33), (3.35) and (3.36) given in the previous subsection. A sinusoidal input voltage source has been used to feed the transformer in all the models. The THD of the simulated exciting currents under healthy and faulty conditions have been compared as per (3.4) for detecting inter-turns winding faults.

Simulation results for single-turn short circuit faults on the primary and secondary sides have been shown in subsection 3.3.1 and the effectiveness of the proposed scheme in detecting these incipient faults has been highlighted. Then in subsection 3.3.2 the fault detection scheme has been extended to detect more severe levels of inter-turn faults i.e. up to five-turn winding faults and provide an estimate of the fault severity. Finally, a discussion of all the simulation based fault detection results have been presented in subsection 3.3.3.

3.3.1 Detection of incipient faults

It has been already discussed in Chapter 1 that detection of incipient stages of inter-turns winding faults such as a single-turn fault, is very difficult. So in this subsection, the effectiveness of the proposed scheme in detecting these incipient faults in the primary and secondary windings has been investigated.

The healthy and faulty transformer models have been simulated under various levels and types of load conditions. Table 3.1 shows the values for the resistance, inductance and capacitance of various load combinations used for simulating the transformer models.

Load level	Type	R_L (Ω)	L_L (mH)	C_L (μF)	Power Factor
No-load	**-**	0	0	0	-
25 % load	**R**	384	0	0	Unity
	RL	307.2	611.2	0	0.8 lagging
	RC	307.2	0	11.513	0.8 leading
50 % load	**R**	192	0	0	Unity
	RL	153.6	305.6	0	0.8 lagging
	RC	153.6	0	23.026	0.8 leading
75 % load	**R**	128	0	0	Unity
	RL	102.4	203.7	0	0.8 lagging
	RC	102.4	0	34.540	0.8 leading
Full load	**R**	96	0	0	Unity
	RL	76.8	152.8	0	0.8 lagging
	RC	76.8	0	46.050	0.8 leading

Table 3.1 Different load conditions used for the single-phase transformer simulations.

3.3.1.1 Detection of single-turn fault on the secondary side

The transformer models for an inter-turn fault on the secondary side have already been derived in (3.14), (3.22), (3.24) and (3.28) for no-load, R – load, RL – load and RC – load respectively. They have been simulated by substituting N_P , N_{SX} and N_F as 261, 268 and 1 respectively for incorporating a single-turn fault on the secondary side.

Under no-load operation of the transformer, the simulated exciting current at faulty state has been obtained from the simulated magnetizing current following (3.15). However under loaded

condition, the simulated exciting current at faulty state has been obtained using (3.23). Finally, these simulated exciting currents at faulty state have been compared with the corresponding simulated exciting currents at healthy state for the detection of the fault.

3.3.1.1.1 Fault detection under full-load operation

The transformer models have been simulated under full-load (with different power factors) for healthy and faulty states and the results have been provided below.

- **Transformer connected to R type (unity p.f.) full-load**

  When connected to an R type full-load (R_L, the load resistance being 96 Ω), the primary line, secondary line and exciting currents simulated under healthy and single-turn (on secondary side) faulty states have been provided in Figures 3.3.a and 3.3.b respectively. Comparing these two figures, it is evident that under an incipient winding fault the changes in the primary and secondary line currents are very small whereas, the exciting current shows more significant changes in its wave-shape and hence, in its harmonic content. The exciting currents under healthy and faulty states have been compared in Figure 3.4.

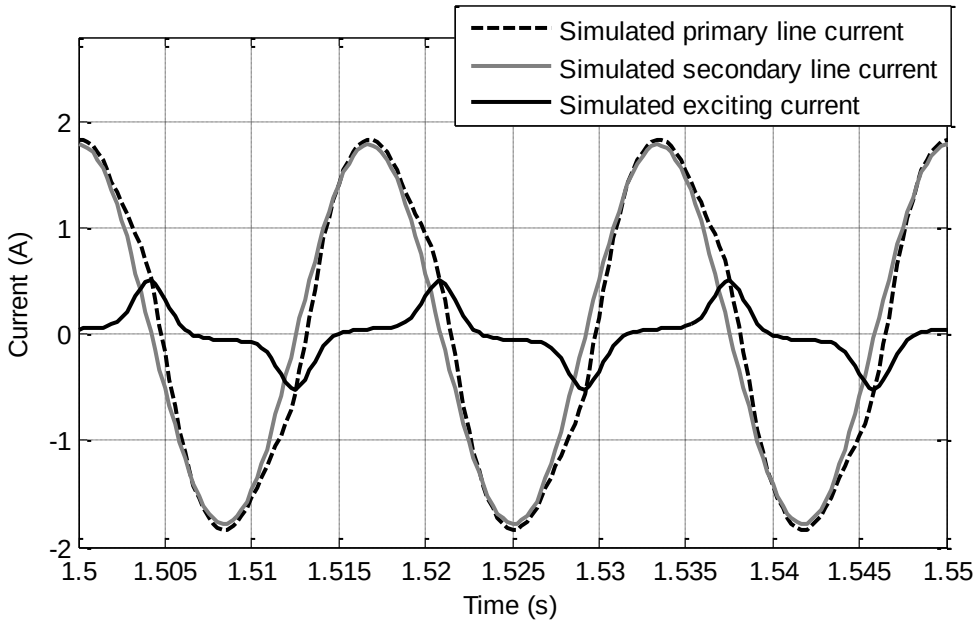

Figure 3.3.a Simulated primary line, secondary line and exciting currents for healthy state under R type full-load

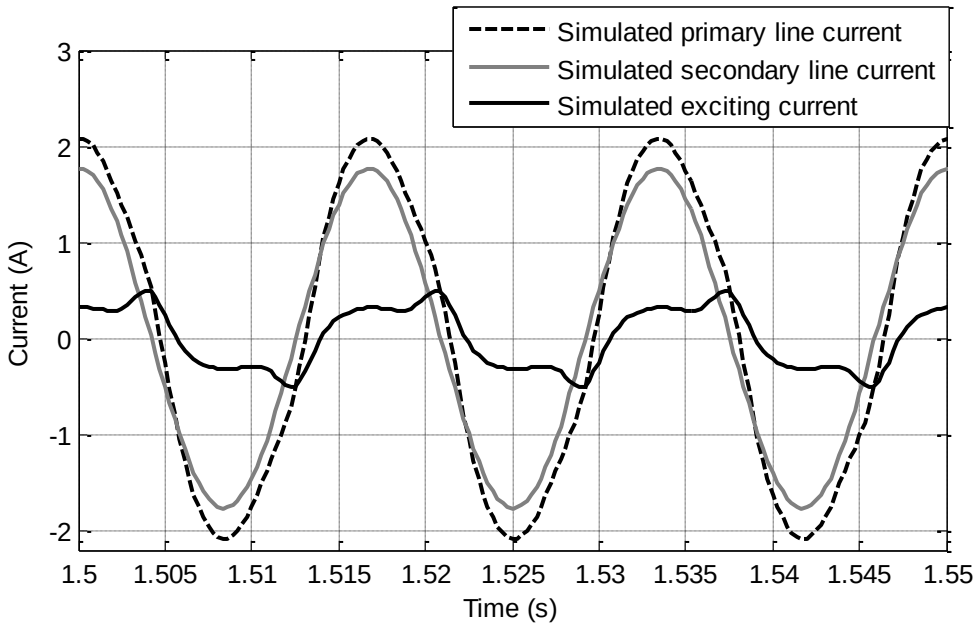

Figure 3.3.b Simulated primary line, secondary line and exciting currents for single-turn faulty state (fault on secondary side) under R type full-load

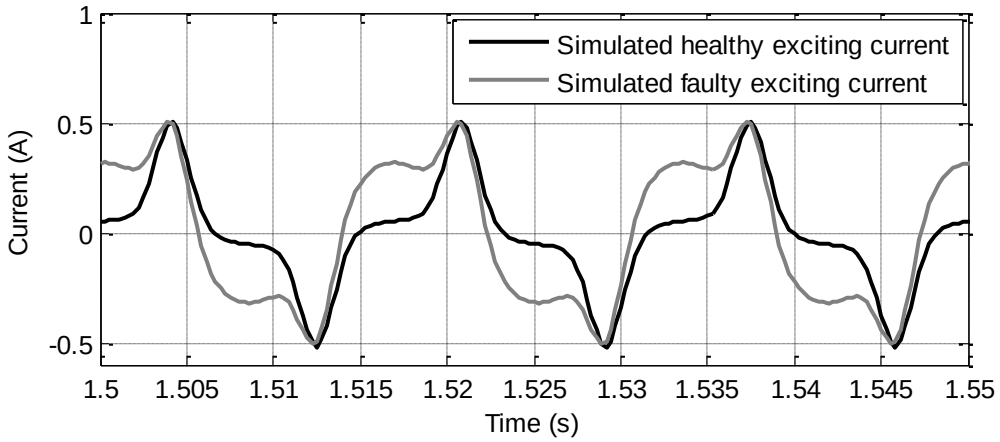

Figure 3.4 Comparison of simulated exciting currents for healthy and single-turn faulty states (fault on secondary side) under R type full-load

The simulated fault current is shown in Figure 3.5. As expected, the fault current in the short-circuited winding is of significantly higher magnitude compared to the rated current of the transformer. This is because, the effective impedance in the shorted winding is extremely small (only a fraction of the winding resistance and leakage inductance on the secondary side).

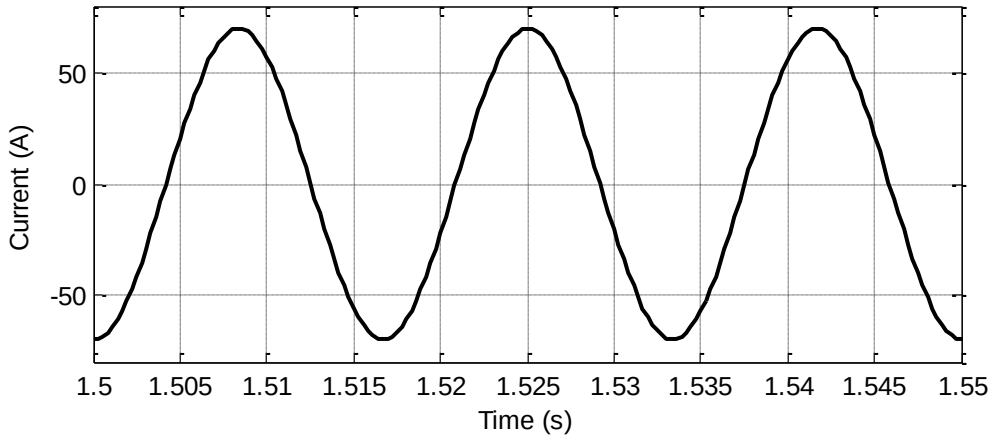

Figure 3.5 Simulated fault current under R type full-load

- **Transformer connected to RL type (0.8 p.f. lagging) full-load**

  Similar results have been observed for the transformer connected to an RL type full-load (load resistance R_L of 76.8 Ω in series with the load inductance L_L of 152.8 mH) of 0.8 lagging power factor. The healthy and faulty exciting currents for this particular load condition have been compared in Figure 3.6.

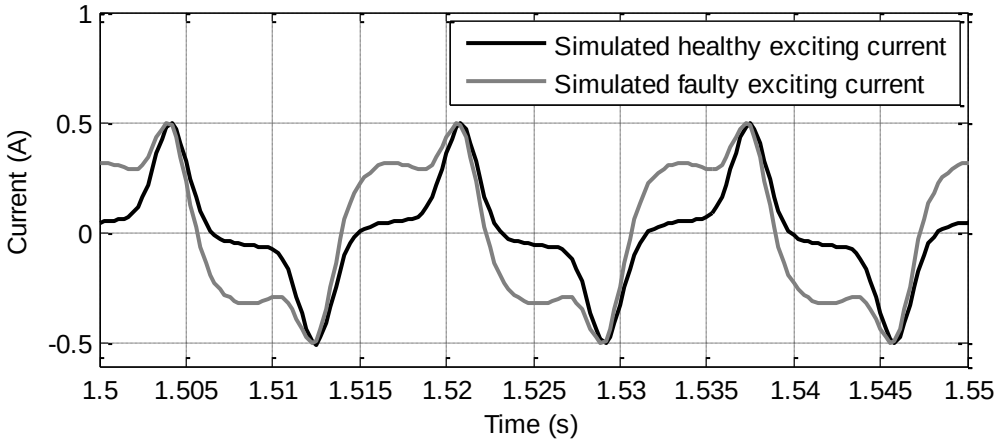

Figure 3.6 Comparison of simulated exciting currents for healthy and single-turn faulty states (fault on secondary side) under RL type full-load

- **Transformer connected to RC type (0.8 p.f. leading) full-load**

  For an RC type full-load (load resistance R_L of 76.8 Ω in series with the load capacitance C_L of 46.05 μF) of 0.8 leading power factor; the healthy and faulty exciting currents have been compared in Figure 3.7.

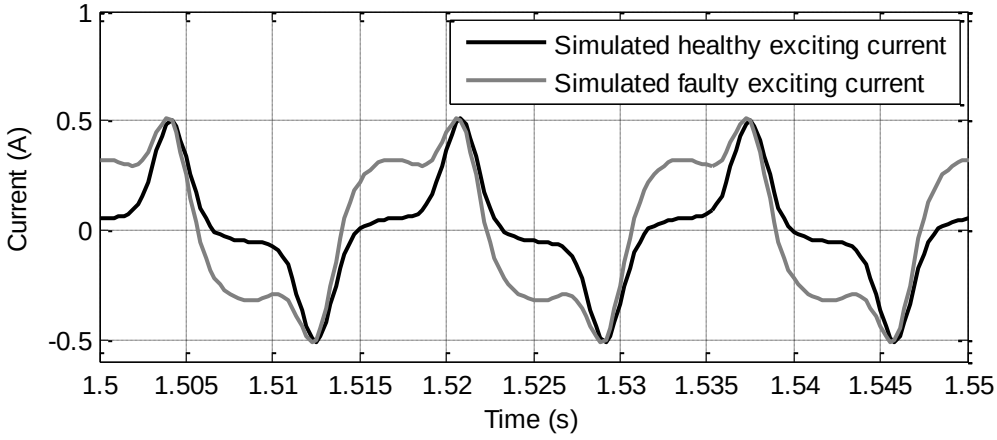

Figure 3.7 Comparison of simulated exciting currents for healthy and single-turn faulty states (fault on secondary side) under RC type full-load

After simulating the models and obtaining the exciting current data, their harmonic content have been investigated using a single-sided FFT [66] at a sampling frequency of 3.6 kHz over 1 sec of current data. Figures 3.8.a and b show the frequency spectra of the simulated exciting currents for healthy and single-turn faulty states under R type full-load condition respectively. It is clearly evident that the changes in the peak values of the third and other higher order harmonics in the exciting current are quite insignificant. However, the peak value of the current's fundamental component rises by a significant proportion with the fault.

This is followed by the computation of the THDs of the exciting currents under healthy and faulty states. Table 3.2 compares the exciting current THDs for a single-turn fault on the secondary side under full-load (with different power factors) operation. It is observed that the THD of the exciting current decreases in case of an inter-turn winding fault. This is in accordance with the proposed fault detection scheme, given in (3.4).

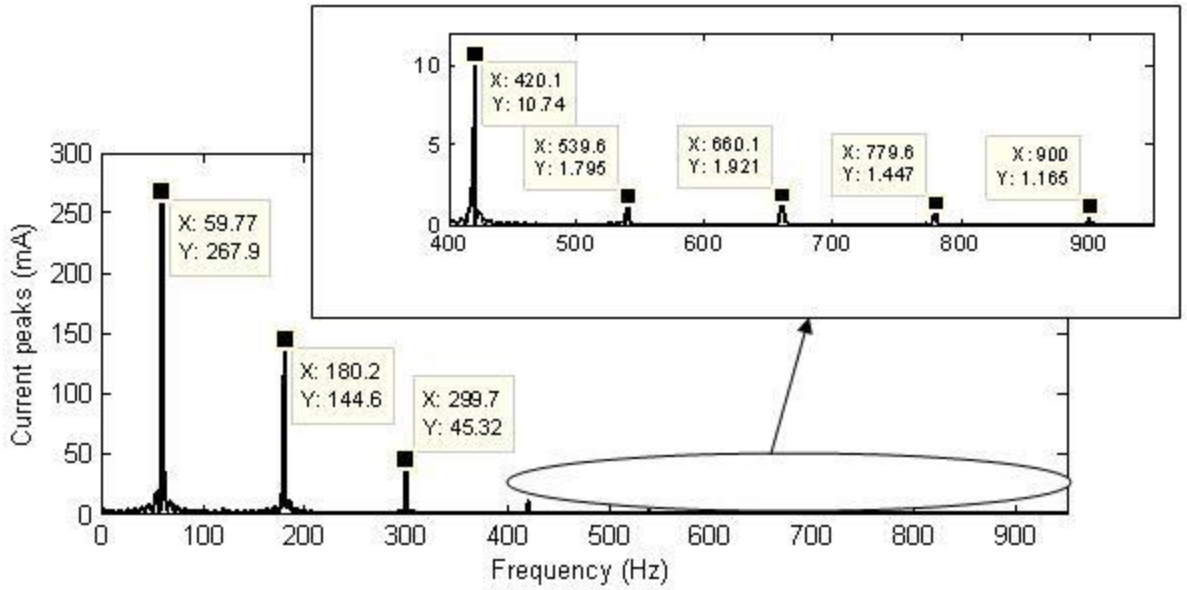

Figure 3.8.a Frequency spectrum of simulated exciting current for healthy state under R type full-load

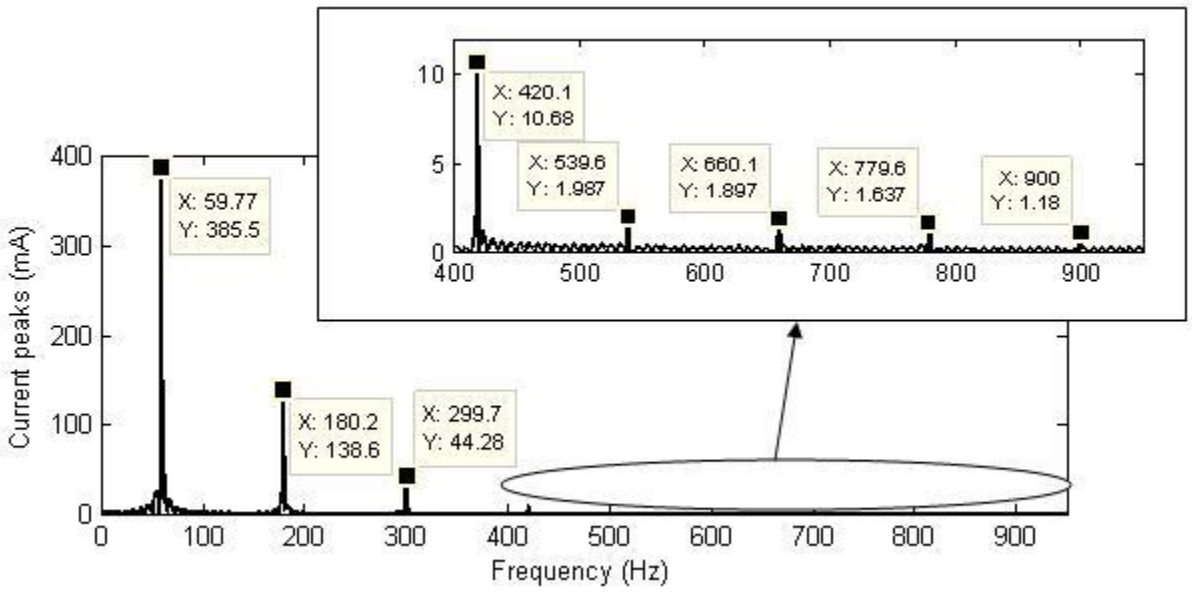

Figure 3.8.b Frequency spectrum of simulated exciting current for single-turn faulty state (fault on secondary side) under R type full-load

Type of load	THD of simulated exciting current	
	Healthy	Single-turn fault
R (unity p.f.)	0.56719	0.37855
RL (0.8 p.f. lagging)	0.56639	0.38036
RC (0.8 p.f. leading)	0.56942	0.37735

Table 3.2 Comparison of simulated exciting current THDs for healthy and single-turn faulty states (fault on secondary side) under full-load

3.3.1.1.2 Fault detection under 75 % load operation

The transformer models have been simulated under 75 % load (with different power factors) for healthy and faulty states and the results have been provided below.

- **Transformer connected to R type (unity p.f.) 75 % load**

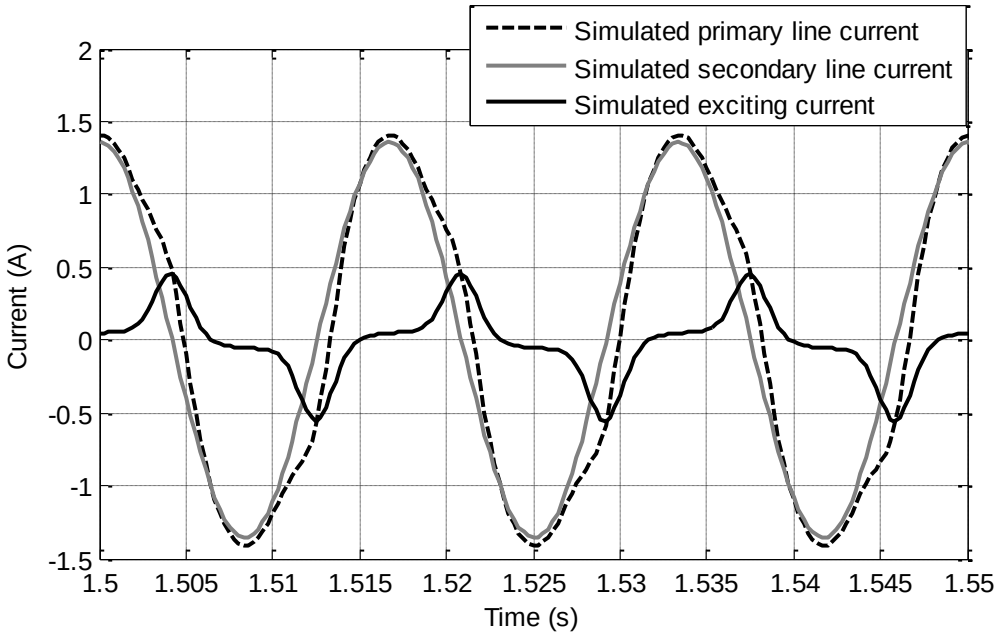

Figure 3.9.a Simulated primary line, secondary line and exciting currents for healthy state under R type 75 % load

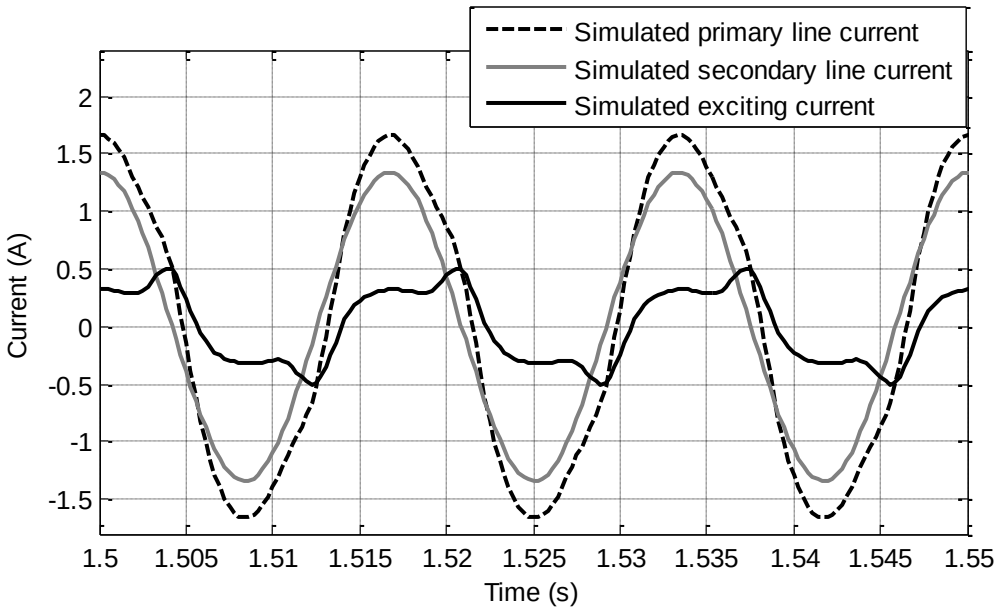

Figure 3.9.b Simulated primary line, secondary line and exciting currents for single-turn faulty state (fault on secondary side) under R type 75 % load

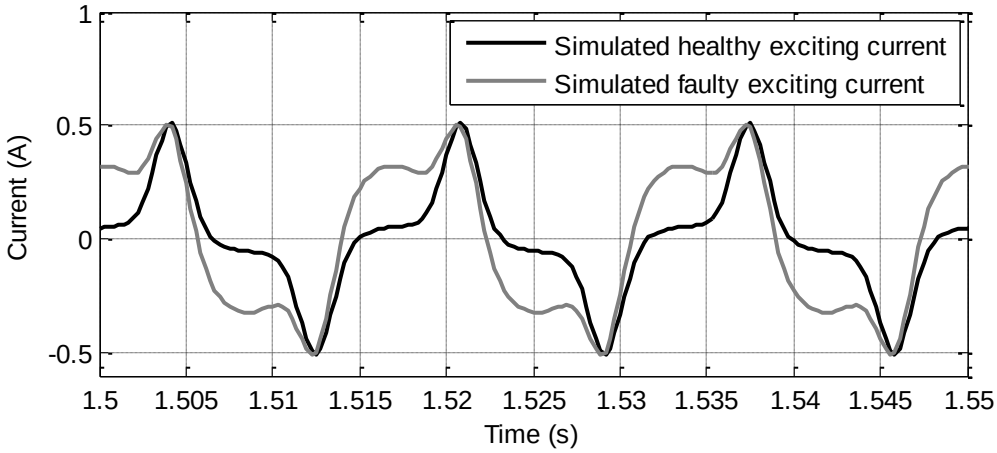

Figure 3.10 Comparison of simulated exciting currents for healthy and single-turn faulty states (fault on secondary side) under R type 75 % load

- **Transformer connected to RL type (0.8 p.f. lagging) and RC type (0.8 p.f. leading) 75 % load**

  Under RL & RC type 75 % load as well; the primary line, secondary line and exciting currents showed similar characteristics as that for an R type 75 % load, given in Figures 3.9.a, 3.9.b and 3.10 respectively. Thus, these results have not been shown explicitly.

Table 3.3 compares the exciting current THDs for a single-turn fault on the secondary side under 75 % load (with different power factors). It is also observed that the THD of the exciting current decreases in case of an inter-turn winding fault.

Type of load	**THD of simulated exciting current**	
	Healthy	**Single-turn fault**
R (unity p.f.)	0.56773	0.37899
RL (0.8 p.f. lagging)	0.56719	0.38035
RC (0.8 p.f. leading)	0.56954	0.37822

Table 3.3 Comparison of simulated exciting current THDs for healthy and single-turn faulty states (fault on secondary side) under 75 % load

3.3.1.1.3 Fault detection under 50 % load operation

The transformer models have been simulated under 50 % load (with different power factors) for healthy and faulty states and the results have been provided below.

- **Transformer connected to R type (unity p.f.) 50 % load**

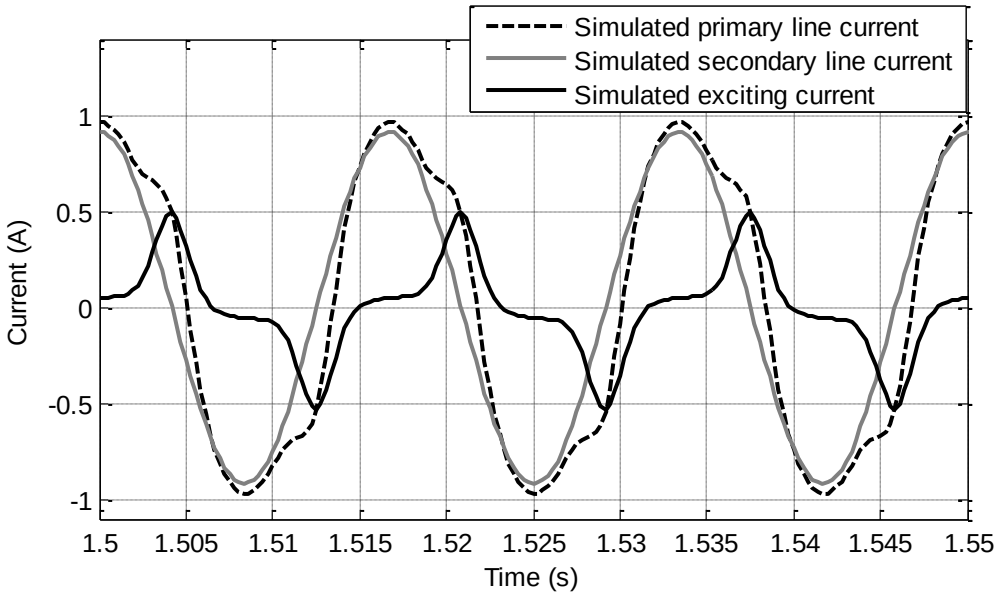

Figure 3.11.a Simulated primary line, secondary line and exciting currents for healthy state under R type 50 % load

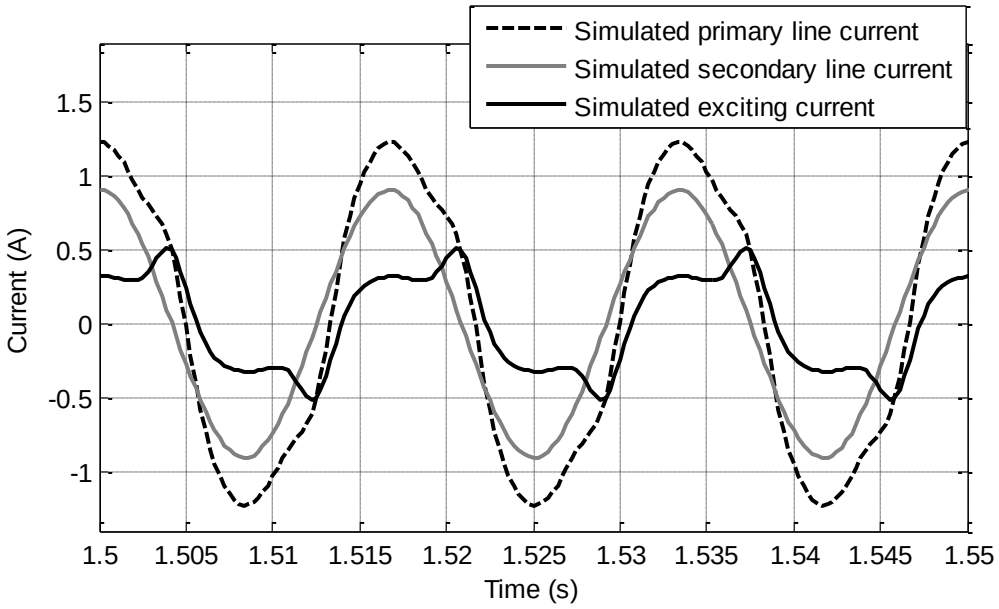

Figure 3.11.b Simulated primary line, secondary line and exciting currents for single-turn faulty state (fault on secondary side) under R type 50 % load

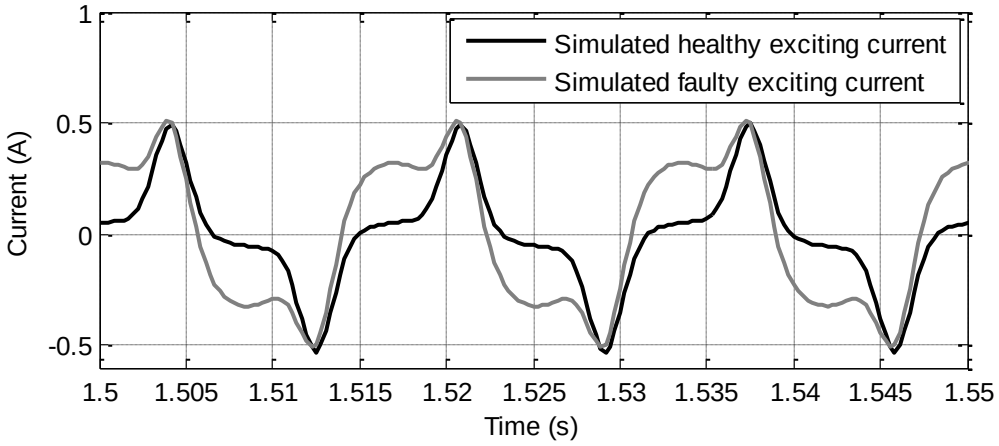

Figure 3.12 Comparison of simulated exciting currents for healthy and single-turn faulty states (fault on secondary side) under R type 50 % load

- **Transformer connected to RL type (0.8 p.f. lagging) and RC type (0.8 p.f. leading) 50 % load**

  Under RL & RC type 50 % load as well; the primary line, secondary line and exciting currents showed similar characteristics as that for an R type 50 % load, given in Figures 3.11.a, 3.11.b and 3.12. Thus, these results have not been shown explicitly as well.

Table 3.4 compares the exciting current THDs for a single-turn fault on the secondary side under 50 % load (with different power factors). It is also observed that the THD of the exciting current decreases in case of an inter-turn winding fault.

Type of load	**THD of simulated exciting current**	
	Healthy	**Single-turn fault**
R (unity p.f.)	0.56821	0.37957
RL (0.8 p.f. lagging)	0.56778	0.38060
RC (0.8 p.f. leading)	0.56977	0.37917

Table 3.4 Comparison of simulated exciting current THDs for healthy and single-turn faulty states (fault on secondary side) under 50 % load

3.3.1.1.4 Fault detection under 25 % load operation

The transformer models have been simulated under 25 % load (with different power factors) for healthy and faulty states and the results have been provided below.

- **Transformer connected to R type (unity p.f.) 25 % load**

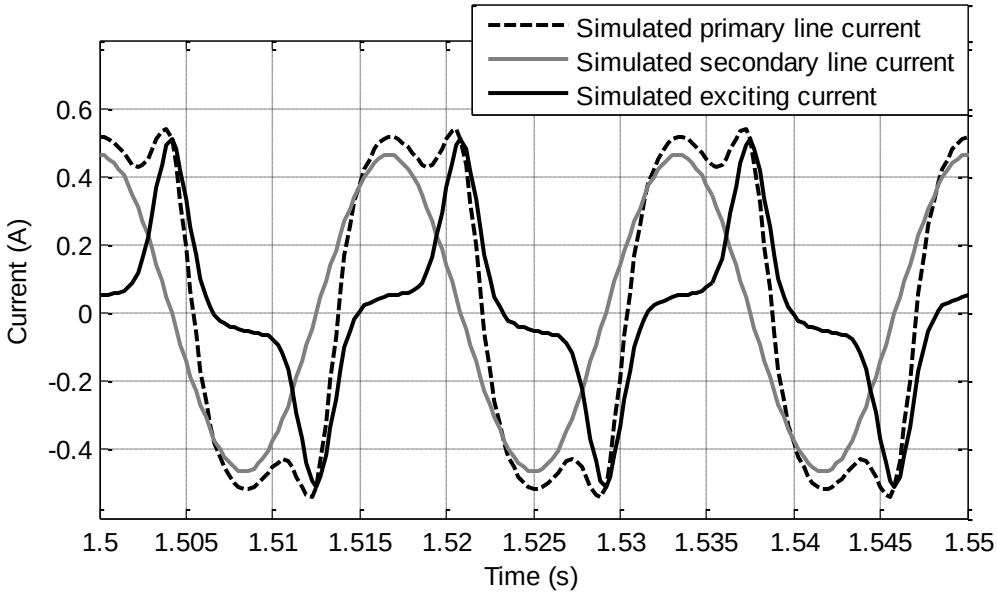

Figure 3.13.a Simulated primary line, secondary line and exciting currents for healthy state under R type 25 % load

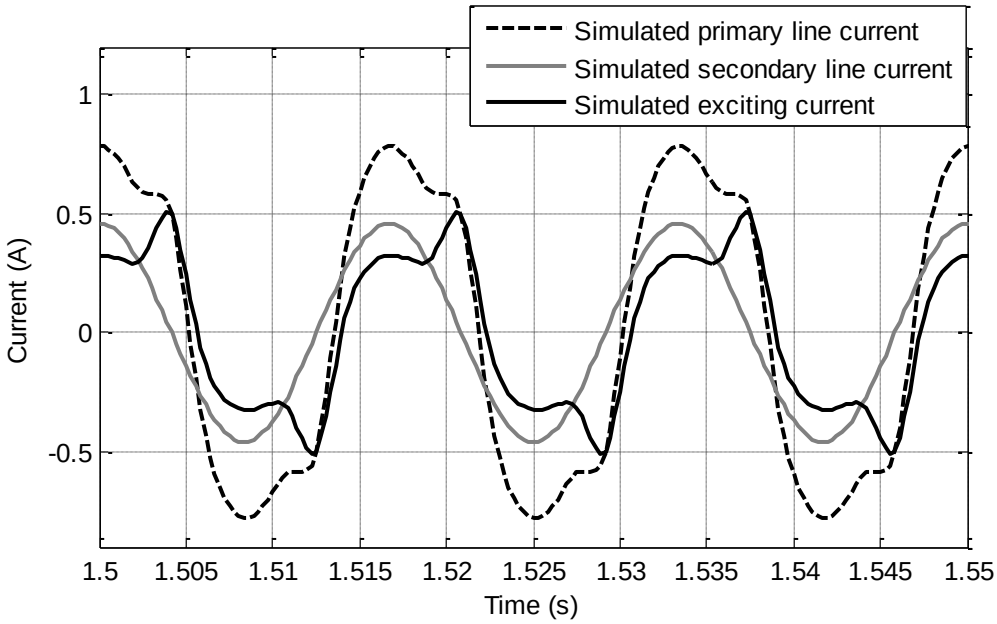

Figure 3.13.b Simulated primary line, secondary line and exciting currents for single-turn faulty state (fault on secondary side) under R type 25 % load

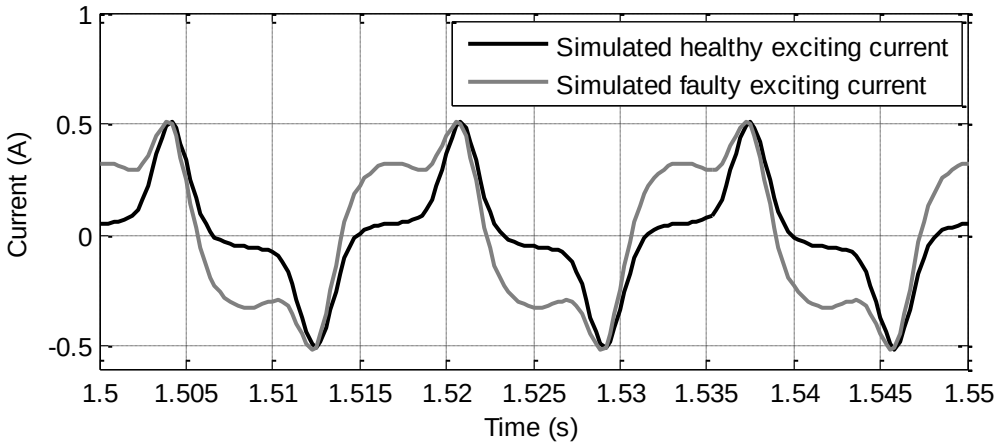

Figure 3.14 Comparison of simulated exciting currents for healthy and single-turn faulty states (fault on secondary side) under R type 25 % load

- **Transformer connected to RL type (0.8 p.f. lagging) and RC type (0.8 p.f. leading) 25 % load**

  Under RL & RC type 25 % load as well; the primary line, secondary line and exciting currents showed similar characteristics as that for an R type 25 % load, given in Figures 3.13.a, 3.13.b and 3.14. Thus, these results have not been shown explicitly.

Table 3.5 compares the exciting current THDs for a single-turn fault on the secondary side under 25 % load (with different power factors). It is also observed that the THD of the exciting current decreases in case of an inter-turn winding fault.

Type of load	**THD of simulated exciting current**	
	Healthy	**Single-turn fault**
R (unity p.f.)	0.56902	0.38024
RL (0.8 p.f. lagging)	0.56848	0.38076
RC (0.8 p.f. leading)	0.56972	0.37988

Table 3.5 Comparison of simulated exciting current THDs for healthy and single-turn faulty states (fault on secondary side) under 25 % load

3.3.1.1.5 Fault detection under no-load operation

The transformer models have been simulated under no-load condition for healthy and faulty states and the exciting currents have been compared in Figure 3.15. The simulated fault current shown in Figure 3.16, is quite similar to that under loaded operation of the transformer.

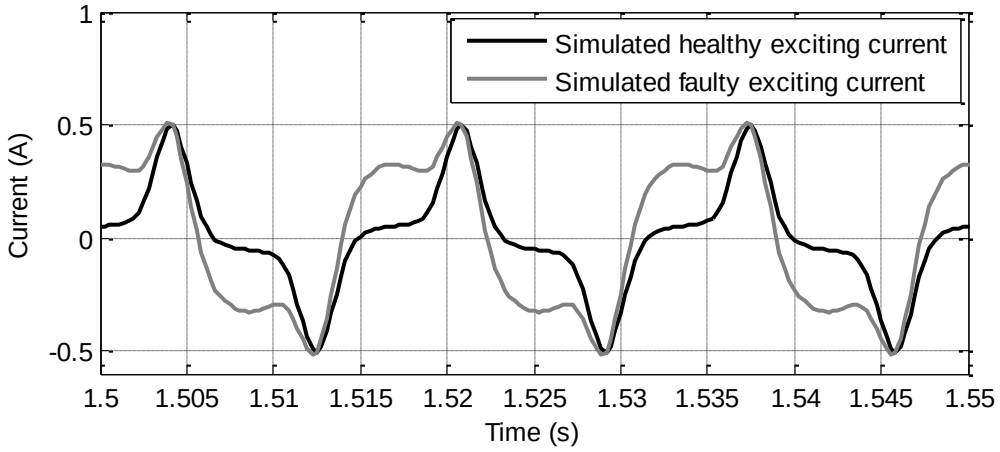

Figure 3.15 Comparison of simulated exciting currents for healthy and single-turn faulty states (fault on secondary side) under no-load

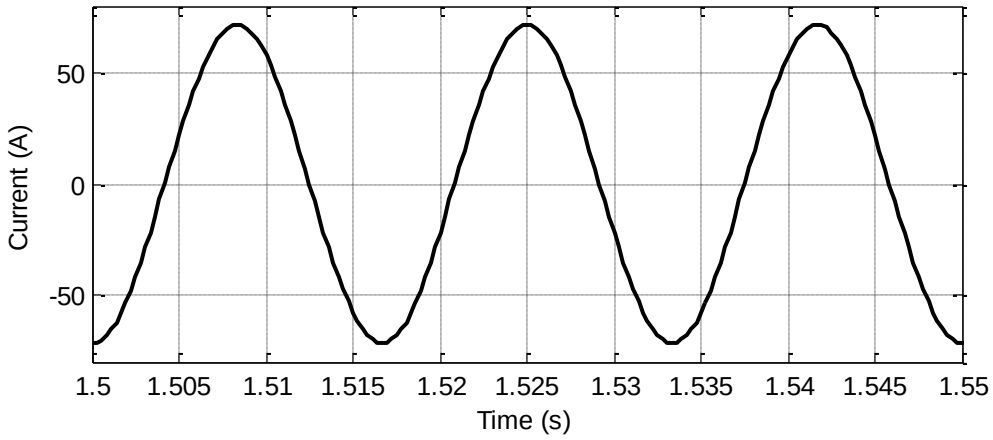

Figure 3.16 Simulated fault current under no-load

Figures 3.17.a & b show the frequency spectra of the simulated exciting currents for healthy and single-turn faulty states under no-load condition respectively. The peak values of the fundamental and other harmonic components show similar changes as seen before for R type full-load operation of the transformer. Then a comparison of the THDs of the exciting currents is provided in Table 3.6. It is observed that even under no-load operation, the exciting current THD is higher under healthy state as compared to that under faulty state.

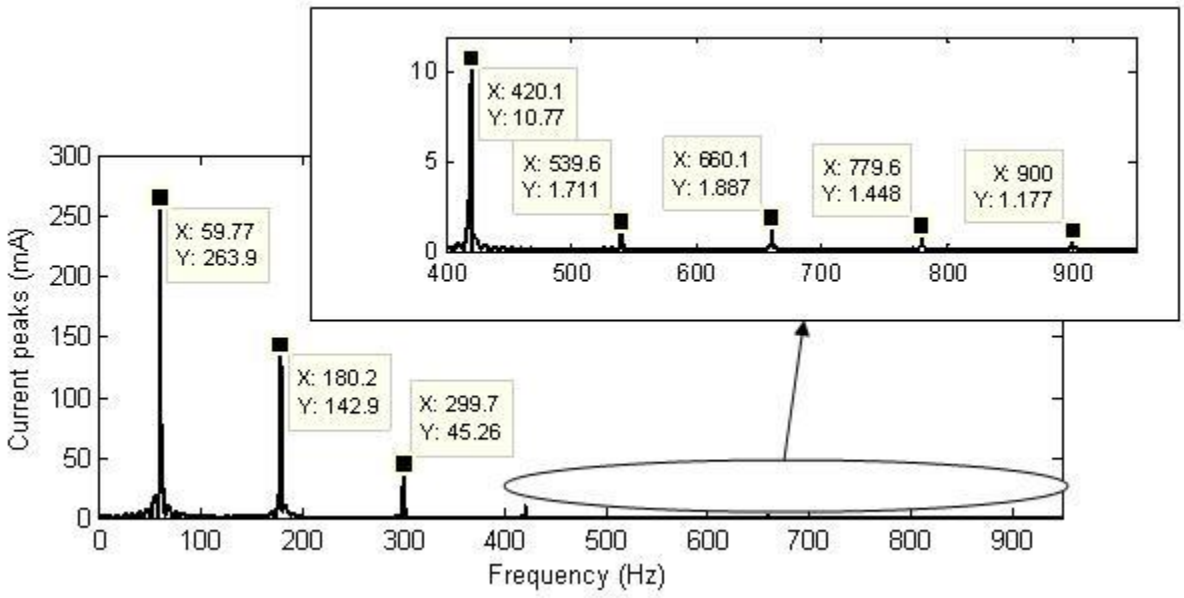

Figure 3.17.a Frequency spectrum of simulated exciting current for healthy state under no-load

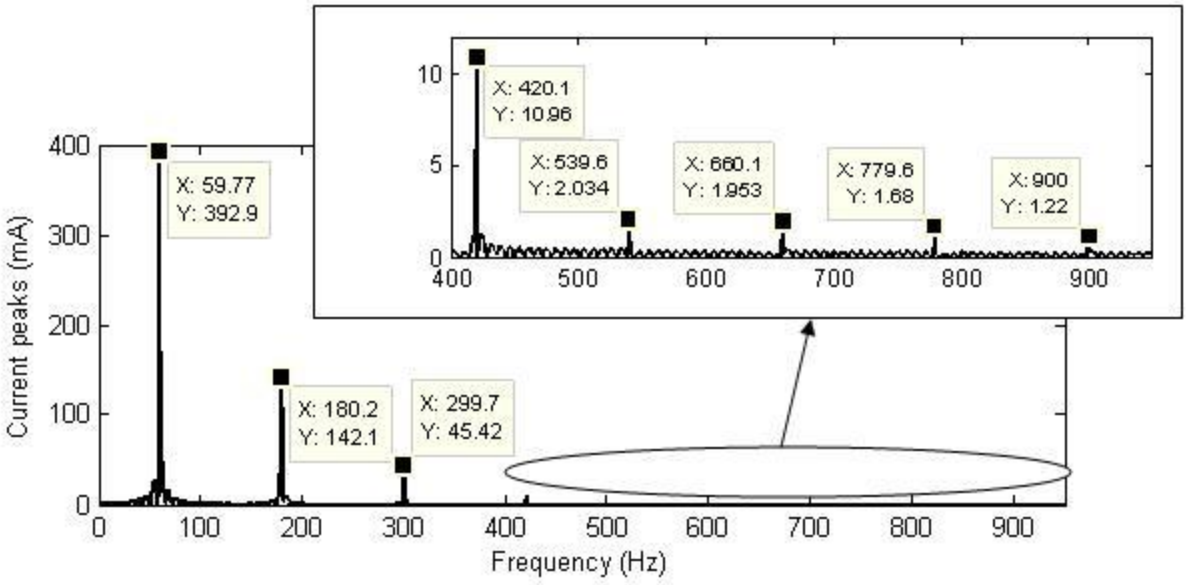

Figure 3.17.b Frequency spectrum of simulated exciting current for single-turn faulty state (fault on secondary side) under no-load

Type of load	**THD of simulated exciting current**	
	Healthy	**Single-turn fault**
No-load	0.56959	0.38082

Table 3.6 Comparison of simulated exciting current THDs for healthy and single-turn faulty states (fault on secondary side) under no-load

3.3.1.2 Detection of single-turn fault on primary side

The transformer models for an inter-turn fault on the primary side have already been derived in (3.32), (3.33), (3.35) and (3.36) for no-load, R – load, RL – load and RC – load respectively. They have been simulated by substituting N_{PX} , N_S and N_F as 260, 269 and 1 respectively for incorporating a single-turn fault on the primary side.

Under no-load operation of the transformer, the simulated exciting current at faulty state has been obtained from the simulated magnetizing current following (3.15). However under on-load operation, the simulated exciting current at faulty state has been obtained using (3.34). Finally,

these simulated exciting currents at faulty state have been compared with the corresponding simulated exciting currents at healthy state for the detection of the fault.

3.3.1.2.1 Fault detection under on-load operation

The transformer models have been simulated under an R type full-load for healthy and single-turn (on primary side) faulty states and the exciting currents have been compared in Figure 3.18. This is followed by a comparison of the THDs of the exciting currents for R, RL and RC loads, provided in Table 3.7. The exciting current THD is consistently higher under healthy state than under faulty state for on-load operation, even if the fault occurs on the primary side.

It was observed that the exciting current waveforms and their THD values in case of RL and RC types of full-load were similar to that for the R type load. Even for 75 %, 50 % and 25 % loads (of different power factors), the changes in the exciting current under healthy and faulty conditions remained consistent. Hence, these results have not been provided explicitly.

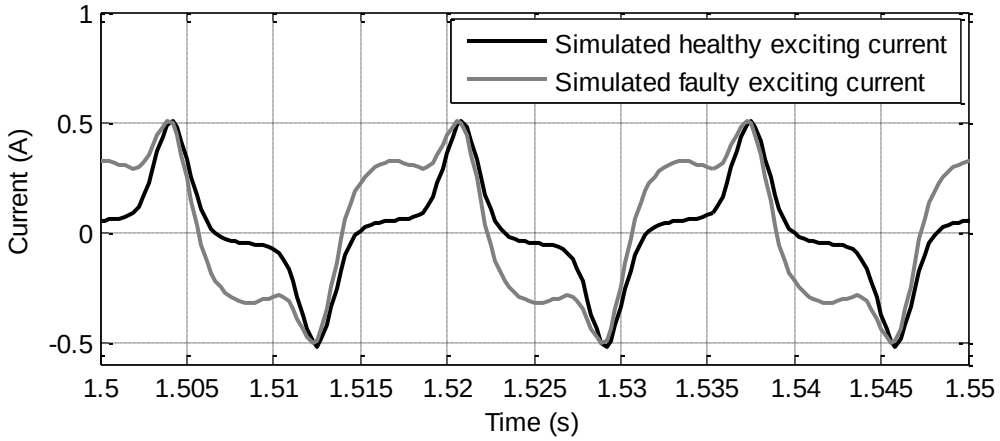

Figure 3.18 Comparison of simulated exciting currents for healthy and single-turn faulty states (fault on primary side) under R type full-load

Type of load	THD of simulated exciting current	
	Healthy	Single-turn fault
R (unity p.f.)	0.56719	0.37873
RL (0.8 p.f. lagging)	0.56639	0.38052
RC (0.8 p.f. leading)	0.56942	0.37745

Table 3.7 Comparison of simulated exciting current THDs for healthy and single-turn faulty states (fault on primary side) under full-load

3.3.1.2.2 Fault detection under no-load operation

The transformer models have been simulated under no-load condition for healthy and single-turn (on primary side) faulty states and the exciting currents have been compared in Figure 3.19. This is followed by a comparison of the THDs of the exciting currents, provided in Table 3.8. The exciting current THD is consistently higher under healthy state than under faulty state for no-load operation, even if the fault occurs on the primary side.

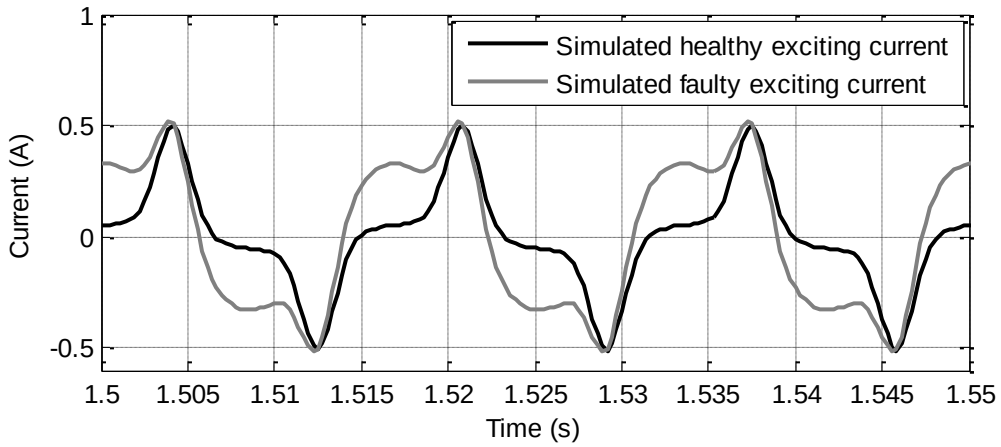

Figure 3.19 Comparison of simulated exciting currents for healthy and single-turn faulty states (fault on primary side) under no-load

Type of load	THD of simulated exciting current	
	Healthy	Single-turn fault
No-load	0.56959	0.38114

Table 3.8 Comparison of simulated exciting current THDs for healthy and single-turn faulty states (fault on primary side) under no-load

3.3.2 Detection of fault severity

It has been already shown in the previous subsection that the proposed scheme detects incipient faults such as a single-turn winding fault under all levels and types of load. Also, incipient faults occurring both on the primary and secondary windings are detected with almost identical sensitivity. In this subsection, the proposed scheme has been extended to estimate the fault severity. The fault severity has been simulated using the models derived previously, only by substituting a higher number of shorter turns in them. Then for each case, the exciting current of the transformer has been obtained and its THD has been computed as an indicator of the fault.

Table 3.9 shows the THD values of the simulated exciting current under R type full-load operation of the transformer for healthy and faulty states. Winding faults ranging from a single-turn short (incipient fault) up to a five-turn short (severe fault) have been simulated on both the primary and secondary windings. Table 3.10 provides similar results for the transformer operating under no-load. It is evident that the THD of exciting current monotonically decreases as the severity of the winding fault increases. This occurs because the peak value of the fundamental component in the exciting current monotonically increases with fault severity. Similar variations in the THD values of exciting current have been observed for RL and RC type full-load operations, hence they have not been explicitly provided. These trends confer with the theoretical explanation provided in subsection 3.1.1.

Operation	THD of simulated exciting current	
Healthy	0.56719	
Severity of fault	**Fault in primary**	**Fault in secondary**
1 turn	0.37873	0.37855
2 turn	0.24613	0.24581
3 turn	0.17751	0.17728
4 turn	0.13760	0.13751
5 turn	0.11209	0.11200

Table 3.9 Comparison of simulated exciting current THDs for healthy and faulty states under R type full-load

Operation	THD of simulated exciting current	
Healthy	0.56959	
Severity of fault	**Fault in primary**	**Fault in secondary**
1 turn	0.38114	0.38082
2 turn	0.24740	0.24709
3 turn	0.17822	0.17810
4 turn	0.13817	0.13806
5 turn	0.11243	0.11236

Table 3.10 Comparison of simulated exciting current THDs for healthy and faulty states under no-load

A time-domain comparison of the exciting current for healthy and faulty states under R type full-load and no-load operations have been provided in Figures 3.20 and 3.21 respectively. The increase in the fundamental peak and RMS values of the exciting current with increase in the fault severity (i.e. with increase in the number of shorted turns on the secondary side) is clearly evident, as shown in Figures 3.22 and 3.23 for R type full-load and no-load operations respectively. The x-coordinate representing ‘0’ turns shorted on the secondary winding in these two figures corresponds to the healthy operation case.

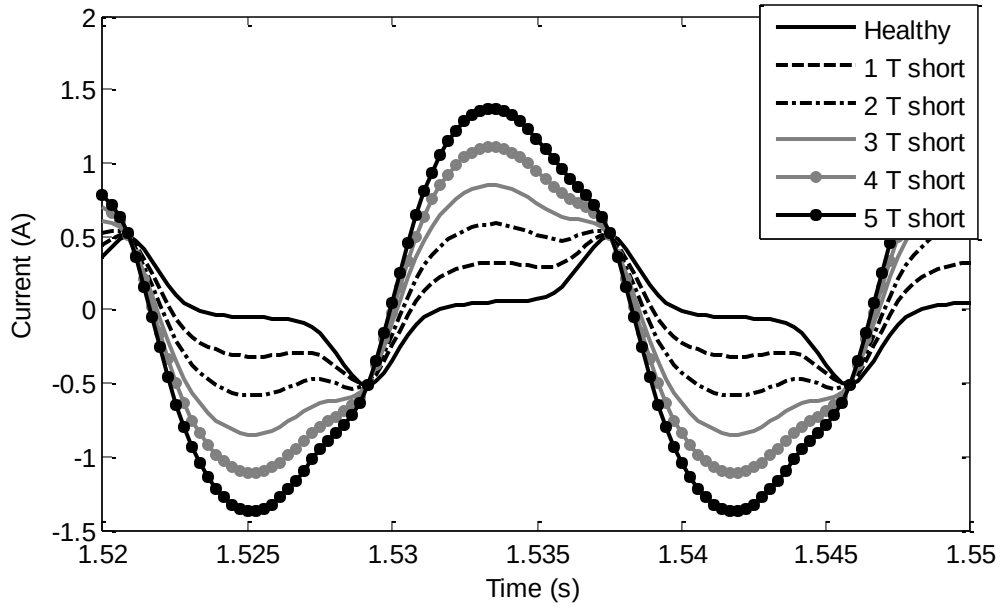

Figure 3.20 Comparison of simulated exciting currents for healthy and faulty states (faults on secondary side) under R type full-load

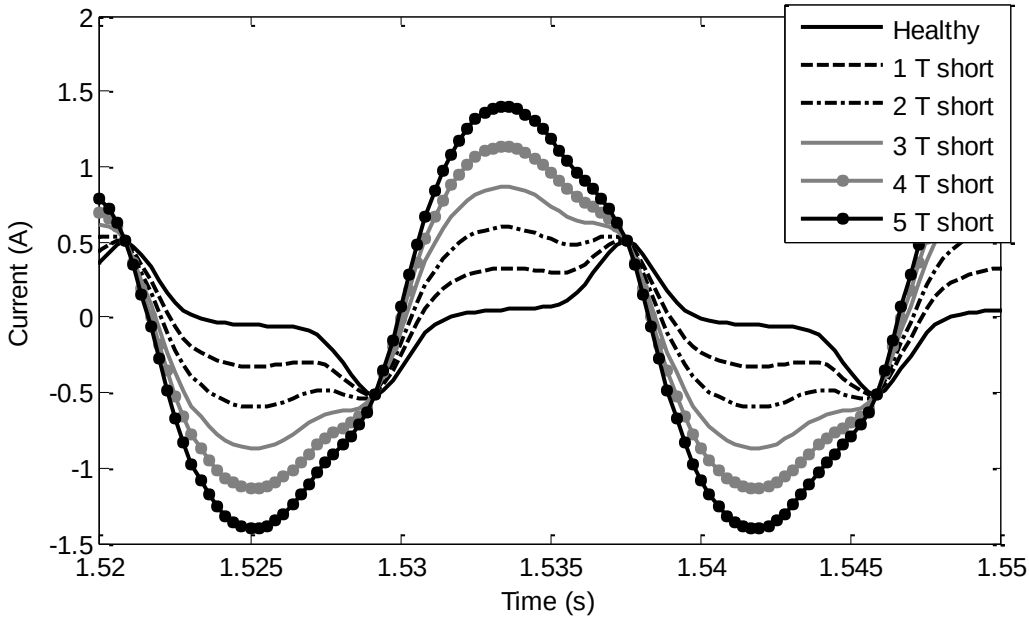

Figure 3.21 Comparison of simulated exciting currents for healthy and faulty states (faults on secondary side) under no-load

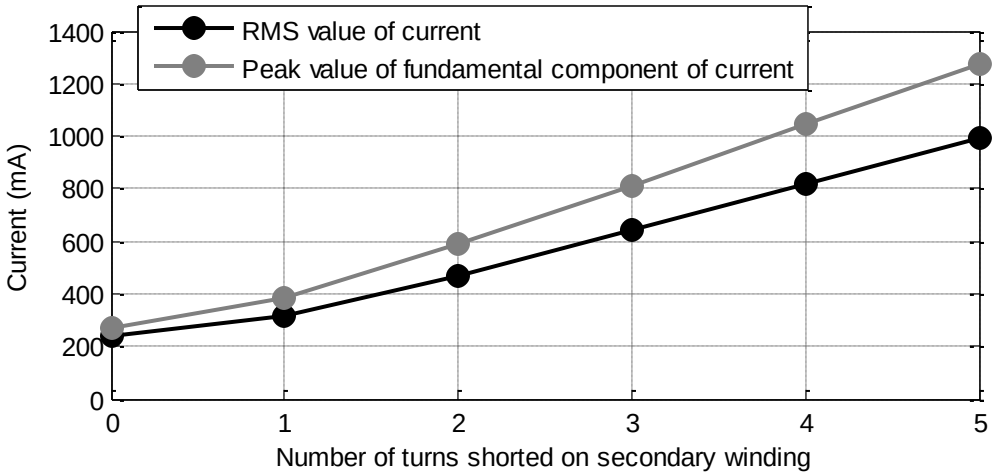

Figure 3.22 Plot of fundamental peak and RMS values of simulated exciting current with respect to the turns shorted on the secondary side under R type full-load

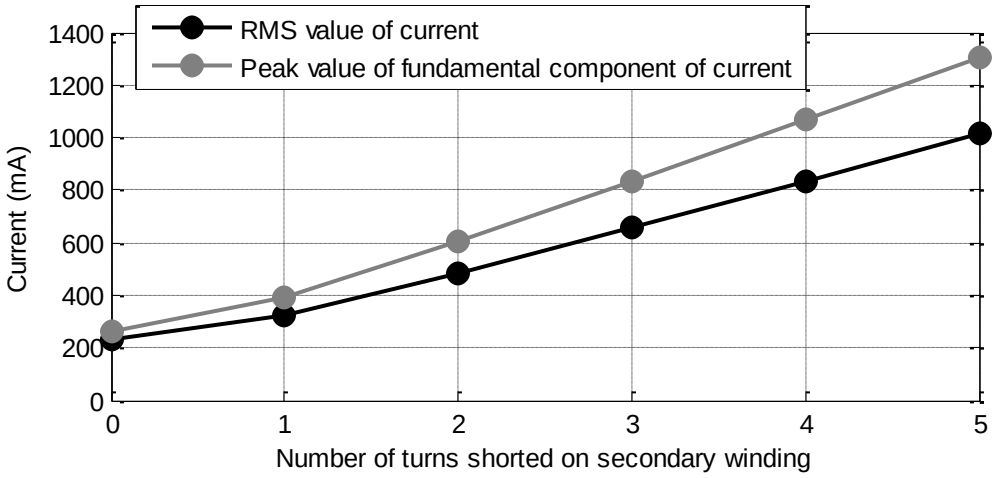

Figure 3.23 Plot of fundamental peak and RMS values of simulated exciting current with respect to the turns shorted on the secondary side under no-load

Similar results have been observed from the time-domain comparison of the exciting currents for winding faults on the primary side, under full-load and no-load operations.

3.3.3 Discussion of simulation results for fault detection

Through elaborate and thorough simulation results, it has been demonstrated that the proposed fault technique is highly effective in detecting even a single-turn winding fault occurring on both the primary and secondary windings. Also, as the scheme is based on the analysis of the harmonic content of the exciting current; it works equally well under any type or level of load. In general, the exciting currents under different load condition for healthy state had THD values of around 0.56 approximately; while those under single-turn faulty states were around 0.38 approximately.

The fault detection technique has been extended to show that it can be used to estimate fault severity as well. It has been observed that the decrease in the THD values of the exciting current is even more significant for higher number of turns shorted. Thus, higher the number of turns shorted, easier it is for detecting the fault using the proposed scheme. This gives an estimation of the sensitivity of the scheme with respect to the severity of the inter-turn winding fault.

Keeping these results in mind, it is worth investigating the performance of the proposed fault detection scheme in practical conditions. In the next chapter, the experimental results for the detection and severity estimation of inter-turn winding faults have been provided.

Chapter 4

Detection of Inter-turn Winding Faults in Single-phase Transformers – Experimental Results

In this chapter, the inter-turn winding fault detection scheme has been tested under various experimental conditions and shown to reliably detect incipient stages as well as more severe levels of such faults. The faults have been artificially created on both the primary and secondary windings of a single-phase transformer ranging from a single-turn fault to a five-turn fault. The experiments have been conducted under different levels and types of load conditions. Finally, a technique for practically implementing the fault detection scheme has been proposed.

4.1 Modified fault detection scheme

It has been already discussed in the previous chapter that for a single-phase transformer the THD of the exciting current decreases in case of an inter-turn winding fault. Through a large number of simulations, it has been established that this particular trend in the THD of exciting current is consistent for faults on primary as well as secondary winding under any load condition. Also, the decrease in the THD of exciting current has been shown to be proportional to the severity level of the fault i.e. the number of turns shorted. Overall, the fault detection scheme has been found to be quite efficient in diagnosing the inter-turn faults in the simulation environment, where a constant 120 V, 60 Hz purely sinusoidal source was always used to supply input power to the healthy and faulty models of the transformer.

However, for the practical implementation of the fault detection scheme, some essential facts need to be taken into consideration. They are:

- The actual terminal voltage available to the primary side of a single-phase transformer in a power distribution network is far from being purely sinusoidal. It contains additional

voltage harmonics. Infact, these voltage harmonics constantly vary with time due to different external factors; thereby changing the current harmonics accordingly as well. Although they are quite small in magnitude, such changes occurring in the primary line voltage get reflected in the exciting current of the transformer.

- In case of an inter-turn winding fault, the RMS value and the harmonic content of the primary line voltage changes by a very small amount [5, 6, 7, 73 and 74]. Nevertheless, these changes in the voltage harmonics during the fault affect the harmonics in the exciting current, irrespective of however small the changes are.

Thus, in order to minimize the influence of the voltage harmonics on inter-turn winding fault detection; the THD of the line voltage needs to be accounted in the fault detection scheme apart from the usual exciting current THD. This enhances the robustness of the scheme and increases its effectiveness. In this chapter, the proposed modification has been incorporated in the fault detection scheme. The experimental set-up for implementing the modified fault detection scheme is shown in Figure 4.1.

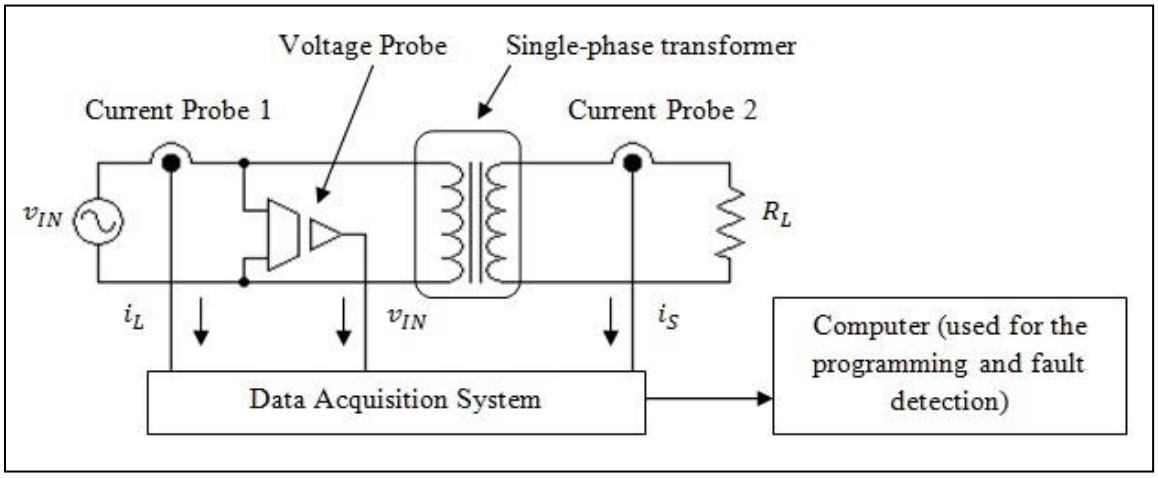

Figure 4.1 Schematic representation of the experimental set-up for fault detection

In Figure 4.1, although the single-phase transformer is shown supplying power to a purely resistive load, the fault detection scheme works independent of the load conditions. The two current sensors are used for acquiring the primary and secondary line current data; while the

voltage sensor acquires the primary line voltage data. Using the acquired primary and secondary line current data, the exciting current can be obtained following (3.1) of the previous chapter. Then, the exciting current THD can be computed using (3.2), also from the previous chapter. As an additional step, the primary line voltage THD can be computed from the experimentally acquired voltage data, using (4.1) where $(V_{IN})_1$ represent the RMS value of the fundamental component in the primary line voltage. The RMS values of the higher order harmonics in the primary line voltage are represented by $(V_{IN})_h$, where h is the harmonic number.

$$(THD)_{v_{IN}} = \sqrt{\sum_{h=2}^{\infty} (V_{IN})_h^{\,2}} \Big/ (V_{IN})_1 \tag{4.1}$$

In the previous chapter, it has been demonstrated that considering the peak values up to 15th harmonic in the exciting current provides good accuracy in the THD computations and hence, in the simulations for fault detection. Following similar methodology, the peak values up to the 15th harmonic have been considered for computing the THDs of both the primary line voltage and the exciting current in this chapter also. It will be shown later in this chapter, that this choice provides good accuracy in the experimental results.

Finally, the fault indicator K can be computed using the voltage and current THDs, as per (4.2). In case of an inter-turn winding fault, the exciting current THD decreases as compared to its value under healthy state as shown in (4.3). The suffixes ‘H’ and ‘F’ correspond to the healthy and faulty states of the transformer. Equation (4.4) is deemed to be true as utilities usually maintain their THD within a small value. Thus, as a cumulative effect the value of the fault indictor K decreases under fault, as highlighted in (4.5) and (4.6).

$$K = (THD)_{i_E} \Big/ (THD)_{v_{IN}} \tag{4.2}$$

$$[(THD)_{i_E}]_H \; > \; [(THD)_{i_E}]_F \tag{4.3}$$

$$[(THD)_{v_{IN}}]_H \approx \; [(THD)_{v_{IN}}]_F \tag{4.4}$$

$$\left(\frac{[(THD)_{i_E}]_H}{[(THD)_{v_{IN}}]_H}\right) > \left(\frac{[(THD)_{i_E}]_F}{[(THD)_{v_{IN}}]_F}\right) \tag{4.5}$$

$$or, \qquad K_H > K_F \tag{4.6}$$

Equation (4.6) represents the modified fault detection scheme. In the next section, various experimental results have been provided to demonstrate the effectiveness of the scheme for detecting incipient as well as severe levels of inter-turn faults.

4.2 Inter-turn winding fault detection based on experimental results

The single-phase shell-type laboratory transformer that was used for performing all the experiments comprised of a number of tap connections on one of its winding, from which electrical terminals were brought out. These terminals were short-circuited for creating inter-turn winding faults ranging from a single-turn to a five-turn fault. A schematic of the transformer tap-connections [71] is provided in Figure 4.2. All the terminals were color coded for convenience in identification, as seen in the figure.

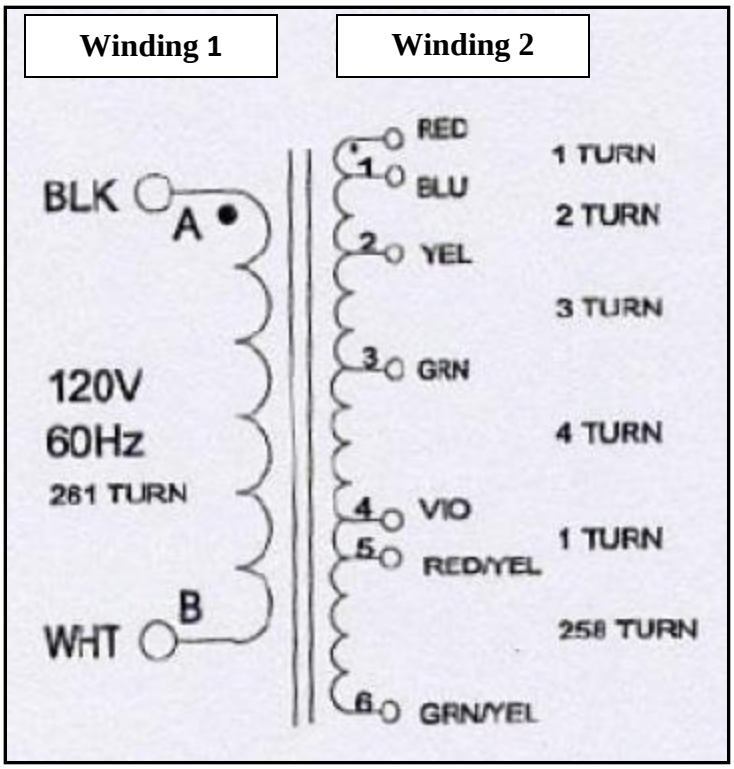

Figure 4.2 Schematic representation of the single-phase transformer tap-connections

Figure 4.3 shows the actual set-up used for conducting all the experiments on the single-phase transformer in the laboratory. The figure clearly shows the two current probes used for sensing the primary and secondary line currents; beside the voltage probe for sensing the primary line voltage. The transformer was fed from the laboratory's power supply via a variac (not shown in Figure 4.3).

Undesired and unexpected fluctuations in the terminal voltage and hence, in the terminal currents are quite common in the real-life operation of a distribution transformer. In order to account for these fluctuations, during each experiment the primary line voltage, primary and secondary line current data were acquired ten times. Using these data, ten different sets of K_H and K_F values were computed for every test condition. Various plots have been provided in the Subsections 4.2.2 and 4.2.3 in order to compare the ten sets of K_H and K_F values for every experimental condition. If the K_H values are consistently greater than their corresponding K_F values, the presence of an inter-turn winding fault is indicated.

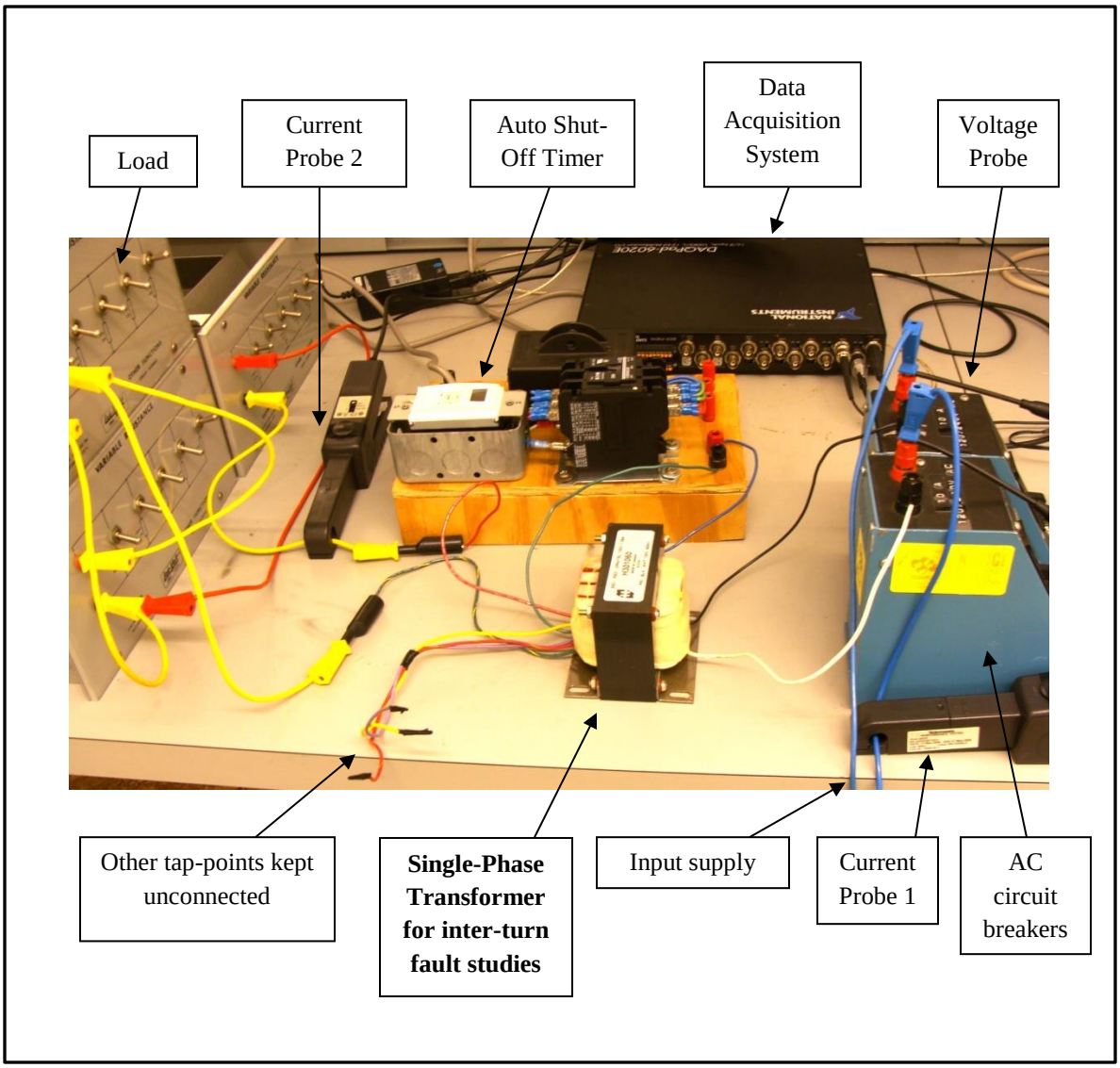

Figure 4.3 Actual experimental set-up in the laboratory for fault detection

4.2.1 Description of the experimental procedure

The various steps followed while performing the experiments can be outlined below:

Step 1:

Under a particular level and type of load, the single-phase transformer was energized and its operating temperature was monitored using an infra-red digital temperature probe [75]. It was also verified using a contact type temperature probe. All the temperature readings were taken at points near the axial centers of the transformer windings and core limbs. The idea was to allow the operating temperature to rise and settle down around a steady state value, as this replicated the real-life operating conditions of a single-phase distribution transformer more closely. Usually, the transformer was considered to have reached steady state operating temperature when its temperature rise was recorded as lower than 2ºC during a consecutive 3hrs time period, as envisaged in [76, 77].

The ambient temperature was considered to be the room temperature in the laboratory (usually around 21-24ºC) where all the experiments were conducted. Generally under full-load operation, the operating temperature settled down around 41-44ºC and took about 6.5-7.5hrs time to reach this steady state. Under no-load condition, the operating temperature took the same amount of time to settle down around 34-37ºC. Usually, the temperature rise was observed to be higher, with higher loading of the transformer. This is obvious, as with higher loading of the transformer, there were higher currents in the primary and secondary windings and hence higher were the copper losses and heat dissipated.

Figure 4.4 shows the temperature rise of the transformer under RC type full-load operation over a period of 7hrs. It clearly demonstrates that at the start of the operation, the ambient temperature of the transformer was 23.5ºC; after 4 hrs the temperature increased up to 41ºC and after 7hrs it reached 42.7ºC. So, basically during the last 3hrs of operation, the temperature rise was 1.7ºC, which is well within the stipulated 2ºC. Thus, the operating temperature of the transformer was deemed to have reached steady state for this particular case.

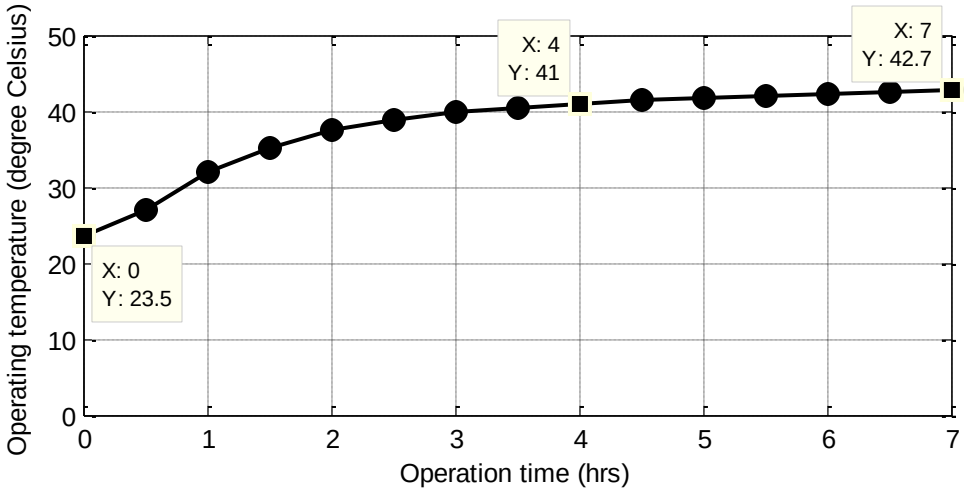

Figure 4.4 Temperature rise of the transformer under RC type full-load

Step 2:

Once the operating temperature settled down around a steady state value; the primary line voltage, primary and secondary line currents data were acquired using a data acquisition system [65] for 10s at a sampling frequency of 18 kHz. Then the acquired data was filtered using a 6^{th} order low-pass Butterworth digital filter of 1 kHz cut-off frequency [66] for noise elimination. As previously discussed in Chapter 2, in order to perform zero phase digital filtering, the 'filtfilt' command in MATLAB [72] was used as it processed the input data in forward as well as reverse directions. At the time of the data acquisition for 10s, any two selected tap-connections of the transformer were shorted for a period of 3s using a digital auto-shut off timer [78]. The 3s time duration was previously set in the timer, so the timing was triggered by an ON switch and after the end of 3s, it automatically turned OFF thus disconnecting the circuit for shorting the selected turns of the transformer.

Step 3:

The acquired dataset comprised of 7s of data corresponding to the healthy state of the transformer (*healthy data*) and 3s of data corresponding to the faulty state (*faulty data*). Any one second of the *healthy data* was chosen and single-sided FFT was performed on the primary line voltage and exciting current (obtained from the acquired primary and secondary line currents

data) for investigating their harmonic contents. Then, $[(THD)_{i_E}]_H$ and $[(THD)_{v_{IN}}]_H$ were computed, followed by the determination of the fault indicator K_H.

The last second of the *faulty data* was chosen and following similar steps as before $[(THD)_{i_E}]_F$ and $[(THD)_{v_{IN}}]_F$ were computed. Choosing the data for the last second in this way, eliminated the chances of any error due to the inter-turn short circuit fault related transients in the line and exciting currents. Usually, these transients were very minimal in magnitude and died down within a maximum of 1.5s. Then the fault indicator K_F was obtained.

Step 4:

Finally, steps 2 and 3 were repeated nine more times for obtaining a total of ten different sets of K_H and K_F values. As described earlier, this was done in order to incorporate the undesired and unexpected fluctuations in the line voltage and currents commonly occurring in real-life utility distribution networks. Additional care was taken, to allow sufficient time interval between the tests for preventing any undesired temperature rise and any permanent damage to the transformer windings due to localized heating caused by the short-circuit of the winding. Usually the tests were repeated after time intervals of a minimum of 10-15mins.

Then, the averages of the ten different values of K_H and K_F were calculated as shown in (4.7) and (4.8), where $(K_H)_{mean}$ and $(K_F)_{mean}$ are the means of the different K_H and K_F values respectively. In these equations, m represents the total number of datasets or tests conducted as part of a single experiment and is equal to ten. Based on the previously discussed theoretical background, these values must satisfy (4.9) and thus, aid in the detection of inter-turn winding faults.

$$(K_H)_{mean} = {(\sum_{i=1}^{m}(K_H)_i)}/{m} \tag{4.7}$$

$$(K_F)_{mean} = {(\sum_{i=1}^{m}(K_F)_i)}/{m} \tag{4.8}$$

$$(K_H)_{mean} > (K_F)_{mean} \tag{4.9}$$

The experimentally acquired waveforms for three different fault cases have been presented in Figures 4.5-4.7, for demonstrating the behavior of the single-phase transformer under fault. The three different fault conditions are:

- Single-turn fault on secondary side under RL type 50 % load
- 2-turn fault on secondary side under R type full-load
- Single-turn fault on primary side under no-load

For all three cases, the waveforms for the primary and secondary line currents, exciting current, primary and secondary line voltages and the circulating fault current have been provided. From these figures it is clearly evident that for incipient stages of inter-turn winding fault such as a single-turn or a 2-turn fault, the changes in the line currents and voltages are extremely small. The exciting current is the only parameter which undergoes any noticeable change.

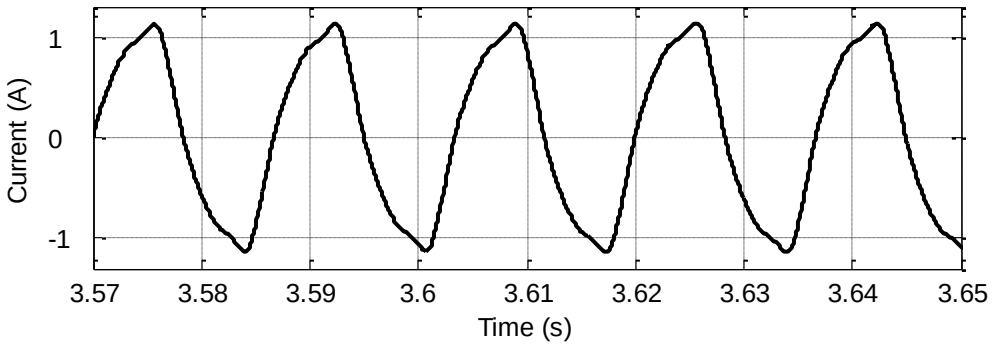

(a) Primary line current

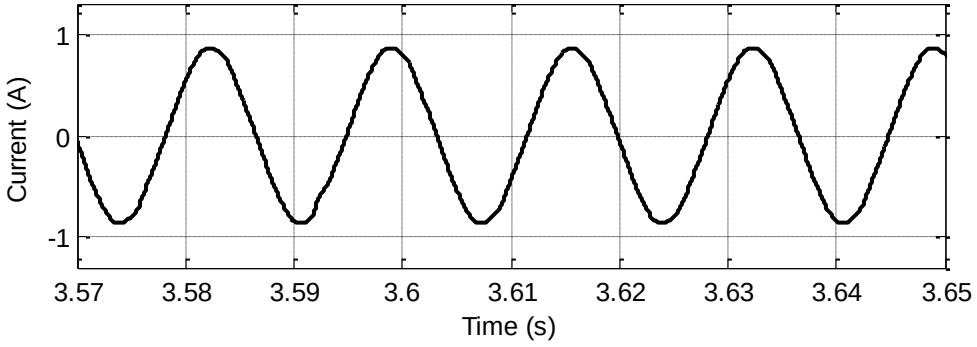

(b) Secondary line current

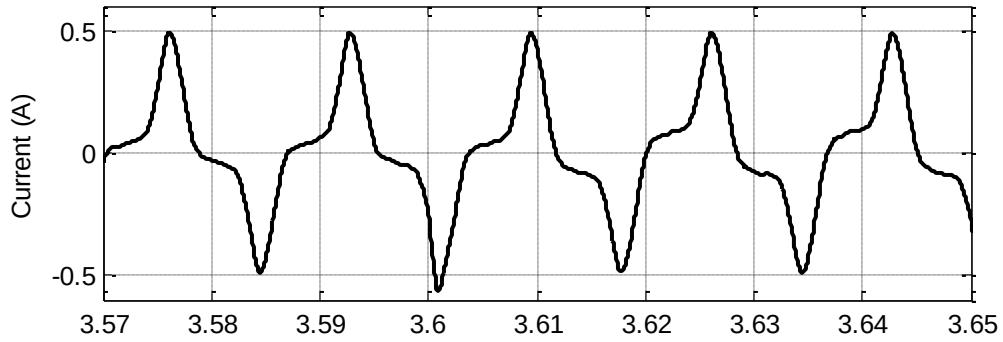

(c) Exciting current

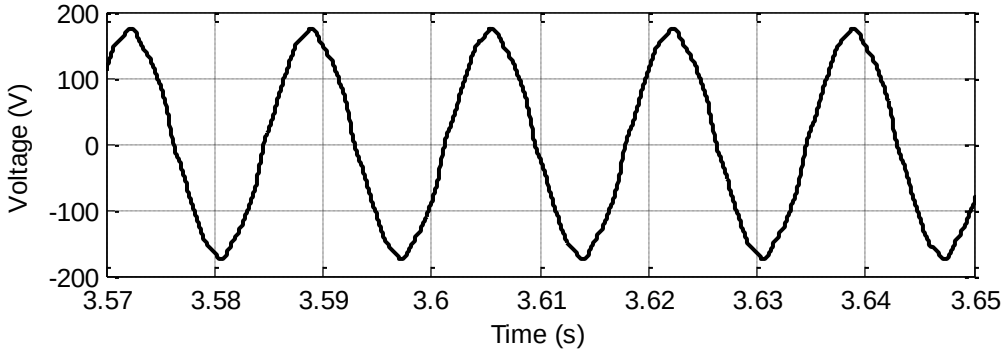

(d) Primary line voltage

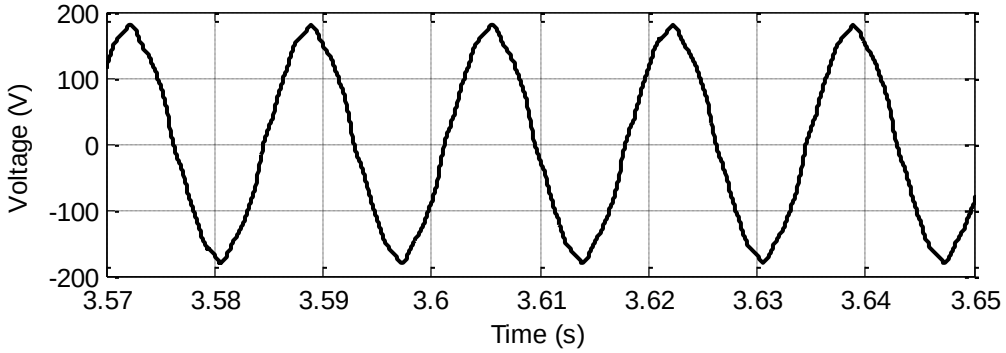

(e) Secondary line voltage

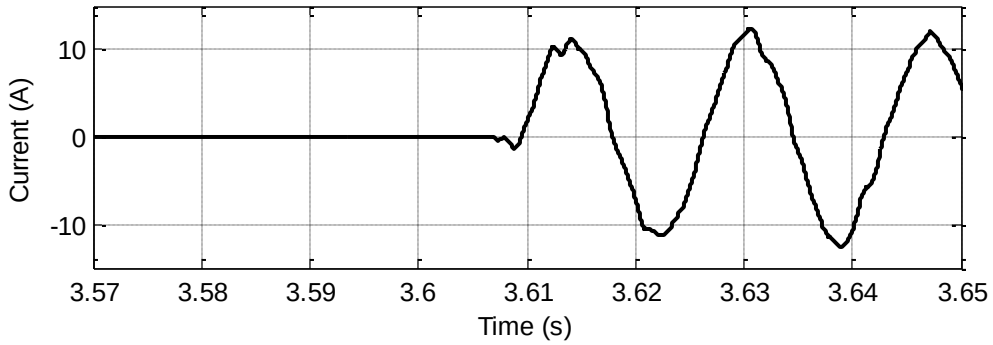

(f) Fault current

Figure 4.5 Experimentally acquired waveforms for single-turn fault on secondary side under RL type 50 % load (Fault occurs at t = 3.608s)

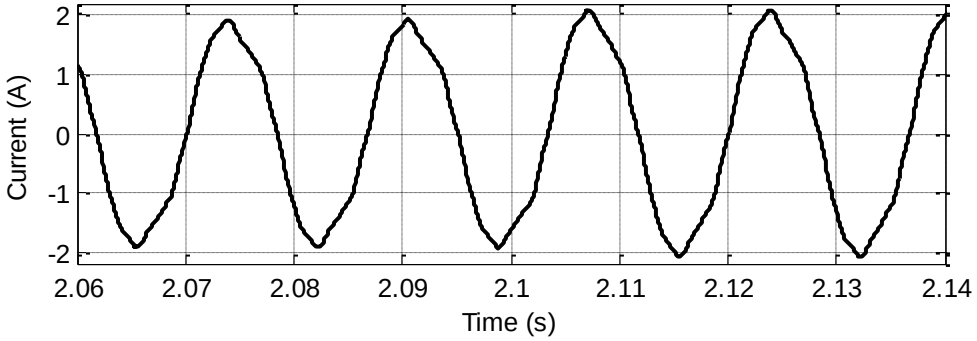

(a) Primary line current

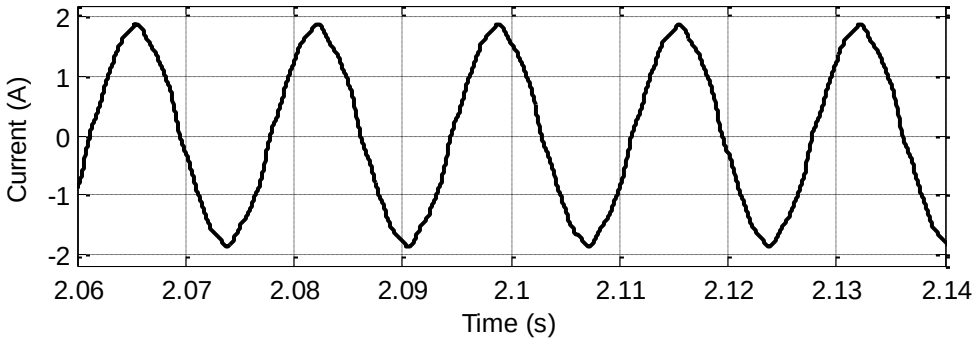

(b) Secondary line current

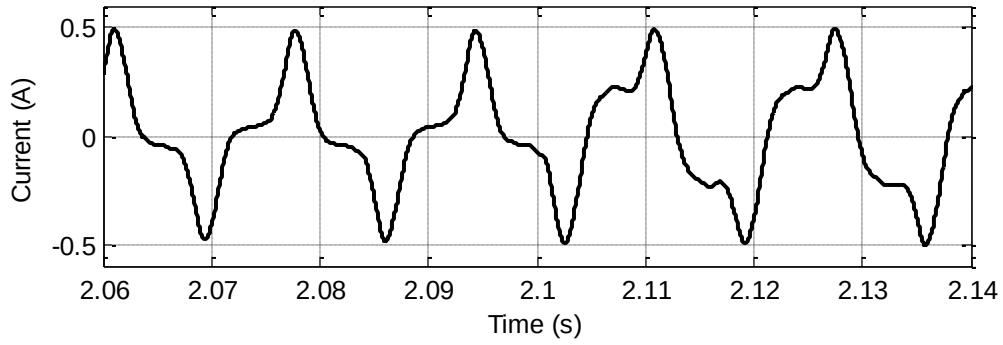

(c) Exciting current

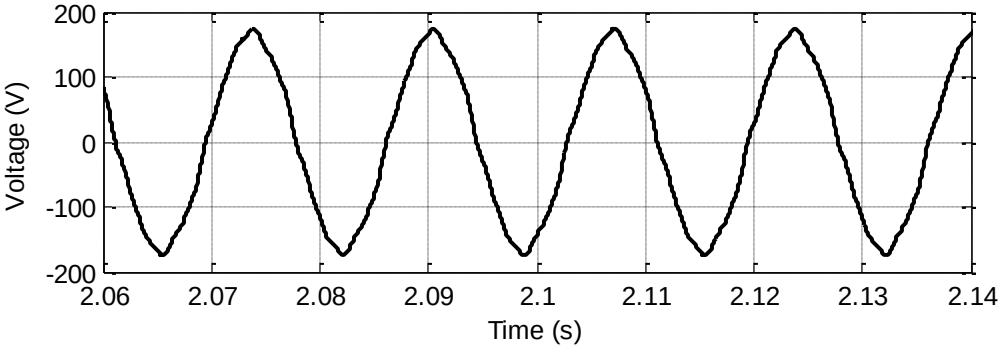

(d) Primary line voltage

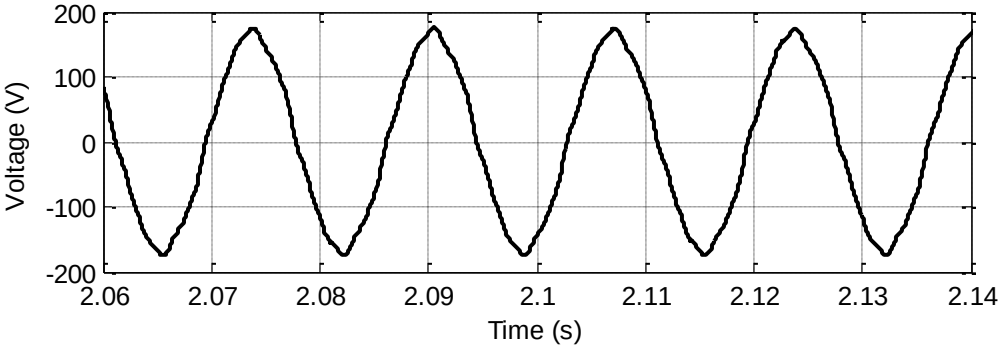

(e) Secondary line voltage

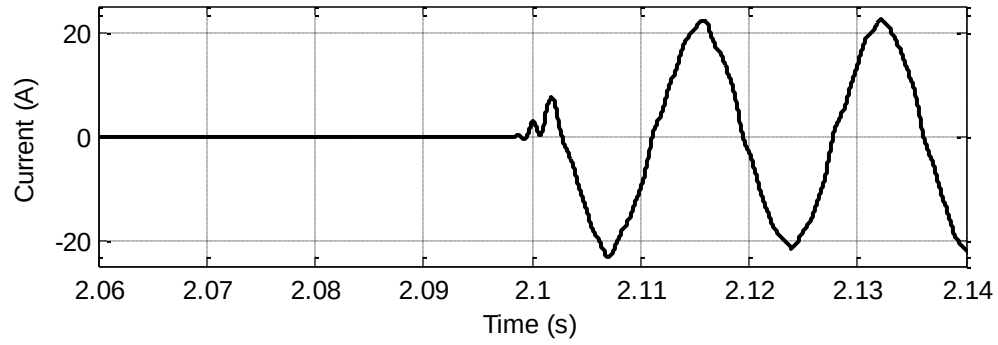

(f) Fault current

Figure 4.6 Experimentally acquired waveforms for 2-turn fault on secondary side under R type full-load (Fault occurs at t = 2.099s)

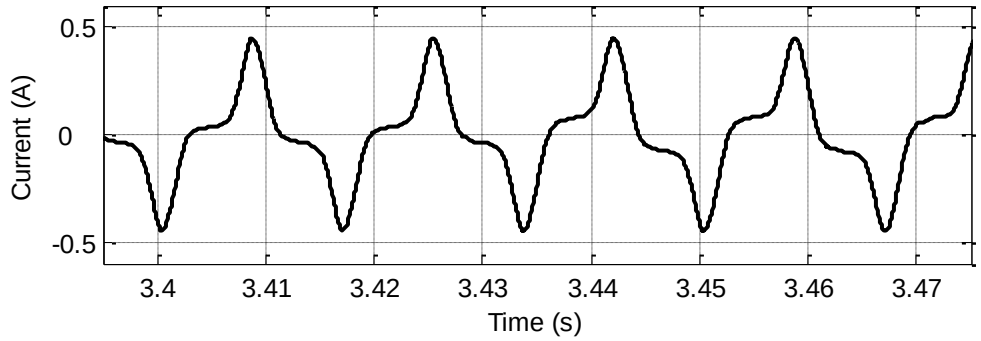

(a) Primary line current or no-load current (same as the exciting current in this case)

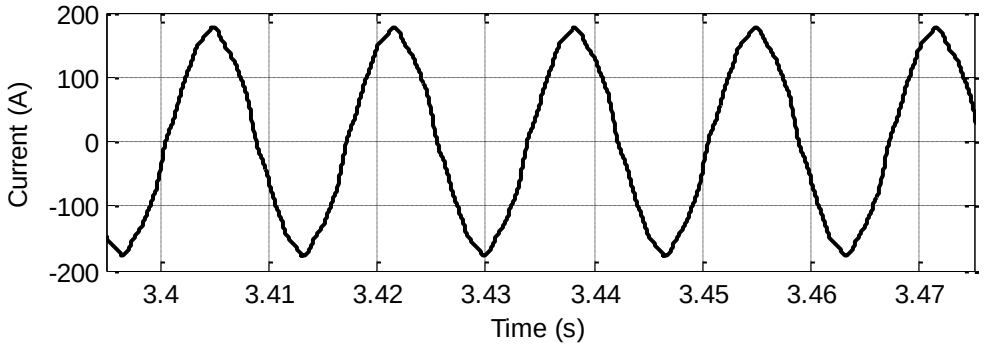

(b) Primary line voltage

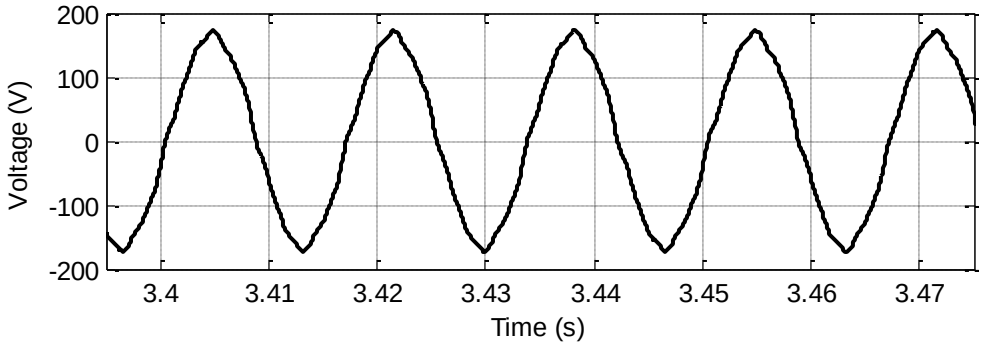

(c) Secondary line voltage

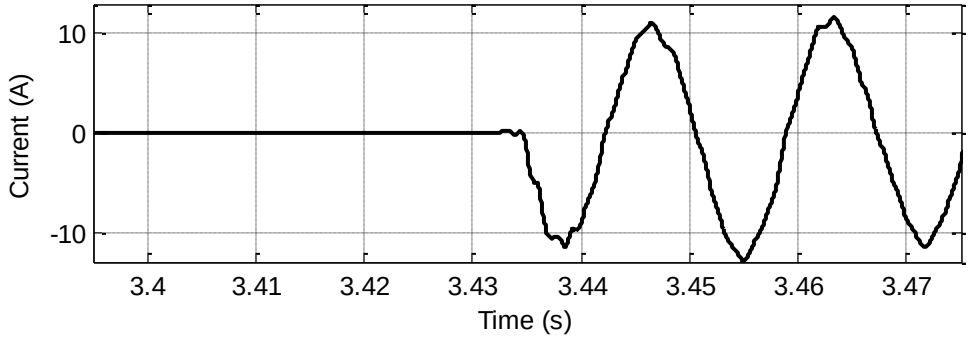

(d) Fault current

Figure 4.7 Experimentally acquired waveforms for single-turn fault on primary side under no-load (Fault occurs at t = 3.435s)

4.2.2 Detection of incipient fault

In this subsection, experimental results for the detection of incipient faults such as a single-turn fault (about 0.37% of the winding) in the single-phase transformer have been presented. Emphasis has been given in detecting such single-turn faults occurring at the extremities of a winding. It has already been explained in Chapter 3, that faults at the winding extremities are the most difficult to detect as they cause minimum rise in the primary line and exciting currents. The faults have been created by shorting the two terminals color coded as ‘RED’ and ‘BLU’ in winding 2 of Figure 4.2. These two terminals included only a single turn in between them.

4.2.2.1 Detection of single-turn fault on secondary side

For this set of experiments, windings 1 and 2 of Figure 4.2 were considered as the primary and secondary sides respectively. 120 V, 60 Hz supply available in the laboratory was fed to winding 1, while winding 2 was either connected to different types and levels of load or left open-circuited in case of no-load operation. All the experiments were conducted strictly following the four steps described earlier.

4.2.2.1.1 Fault detection under full-load operation

Experiments were conducted with the transformer operating under full-load condition (with different power factors) and the results have been presented below. For each experiment, ten different datasets were acquired; then the primary line voltages and exciting currents corresponding to healthy as well as faulty states were obtained from each dataset. FFTs were then performed on these current and voltage data to investigate their harmonic contents and compute their THDs. Finally the K_H and K_F values were calculated and compared for fault detection.

Figures 4.8-4.10 demonstrate the variation of the fault indicator K for inter-turn winding faults under full-load operation in case of R type (unity p.f.), RL type (0.8 p.f. lagging) and RC type (0.8 p.f. leading) loads respectively. It can be clearly seen, that the individual values of K_H are consistently greater than that of K_F as outlined by (4.6). The averages of K_H and K_F values are also shown for the three types of loads in these figures. The computation of these averages accounts for the undesired fluctuations in the individual K_H and K_F values obtained from the various datasets. As outlined in (4.9), the mean of the K_H values is consistently greater than that of the K_F values. Table 4.1 shows the K_H and K_F mean values and their differences which indicate the presence of an inter-turn winding fault.

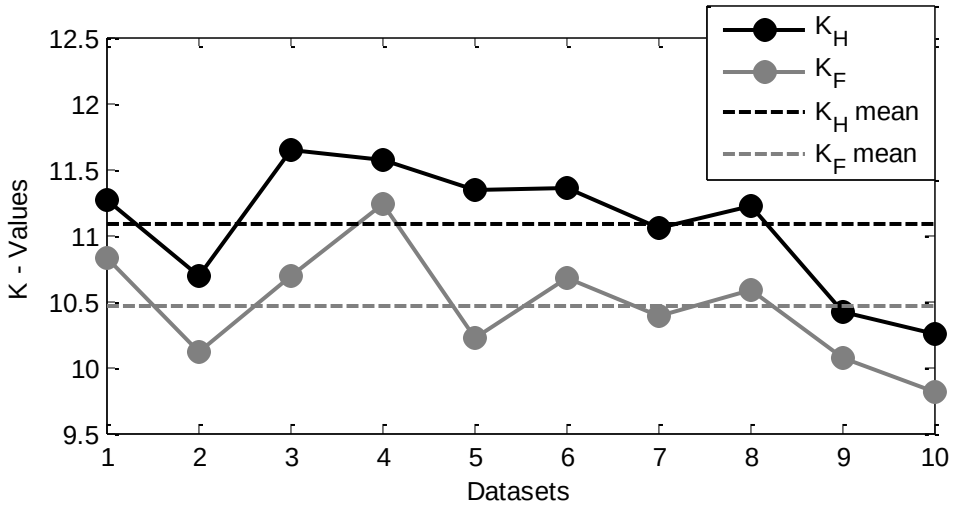

Figure 4.8 Variation of fault indicator for a single-turn fault on secondary side under R type full-load

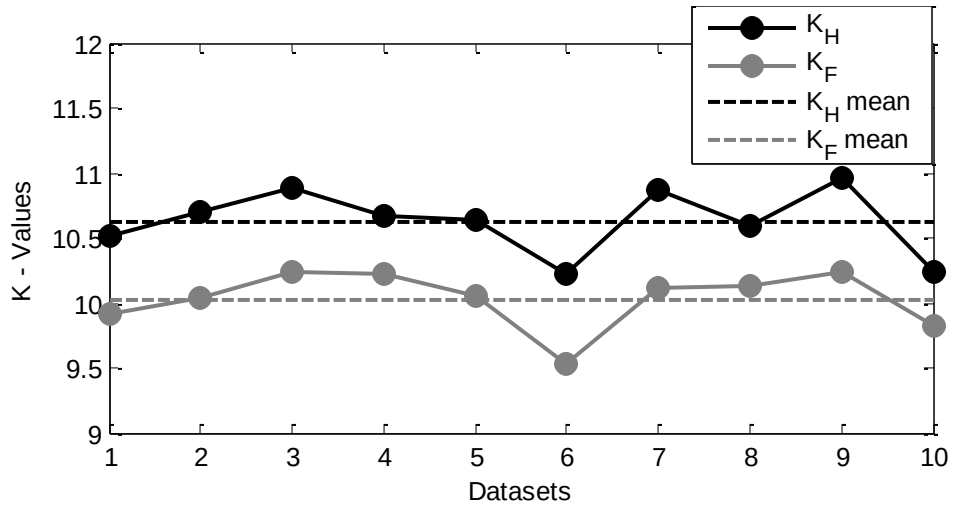

Figure 4.9 Variation of fault indicator for a single-turn fault on secondary side under RL type full-load

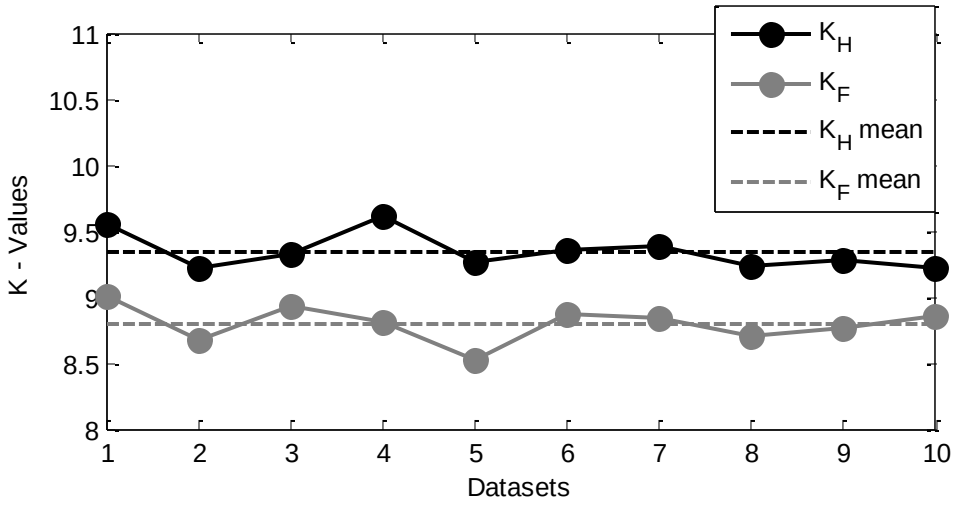

Figure 4.10 Variation of fault indicator for a single-turn fault on secondary side under RC type full-load

Type of load	$(K_H)_{mean}$	$(K_F)_{mean}$	Difference
R	11.08224	10.45769	0.62455
RL	10.62568	10.02899	0.59669
RC	9.34513	8.79693	0.54820

Table 4.1 Variation of the arithmetic mean values of the fault indicator for a single-turn fault on secondary side under full-load

4.2.2.1.2 Fault detection under 75 % load operation

Experiments were conducted following exactly the same procedure for 75 % load level and the variation of the fault indicator in case of R (unity p.f.), RL (0.8 p.f. lagging) and RC (0.8 p.f. leading) types of load are presented in Figures 4.11-4.13. This is followed by Table 4.2 which shows the average values of K_H and K_F and their differences for the 75 % load condition.

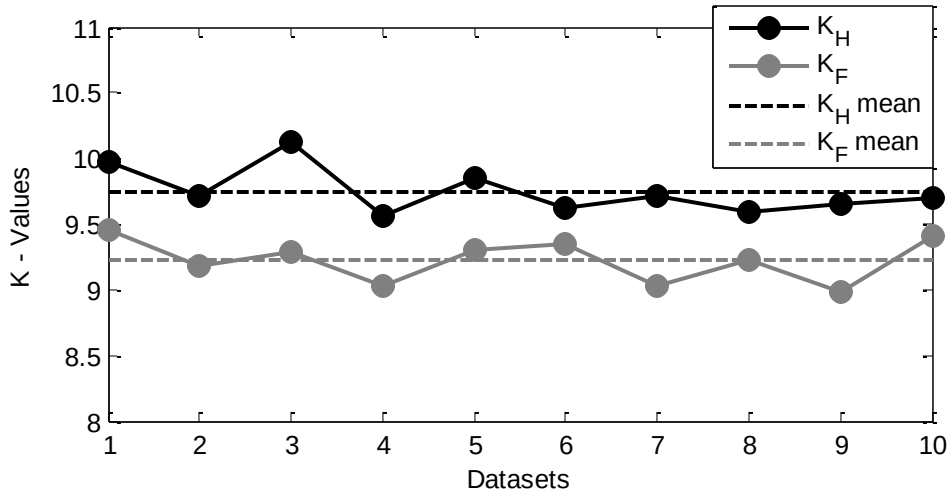

Figure 4.11 Variation of fault indicator for single-turn fault on secondary side under R type 75% load

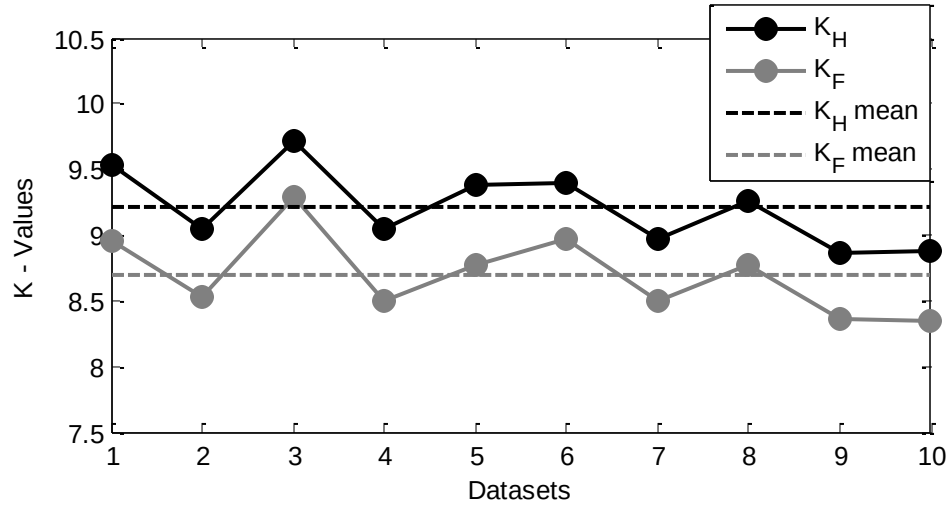

Figure 4.12 Variation of fault indicator for a single-turn fault on secondary side under RL type 75 % load

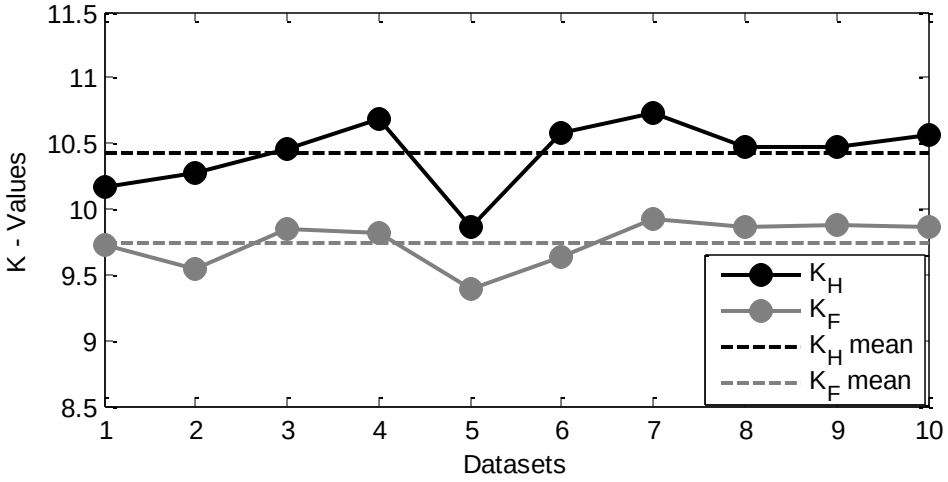

Figure 4.13 Variation of fault indicator for a single-turn fault on secondary side under RC type 75 % load

Type of load	$(K_H)_{mean}$	$(K_F)_{mean}$	Difference
R	9.74972	9.22615	0.52357
RL	9.20919	8.69879	0.51040
RC	10.42904	9.74688	0.68216

Table 4.2 Variation of the arithmetic mean values of the fault indicator for a single-turn fault on secondary side under 75 % load

4.2.2.1.3 Fault detection under 50 % load operation

Experiments were conducted following exactly the same procedure for 50 % load level and the variation of the fault indicator in case of R (unity p.f.), RL (0.8 p.f. lagging) and RC (0.8 p.f. leading) types of load are presented in Figures 4.14-4.16. This is followed by Table 4.3 which shows the average values of K_H and K_F and their differences for the 50 % load condition.

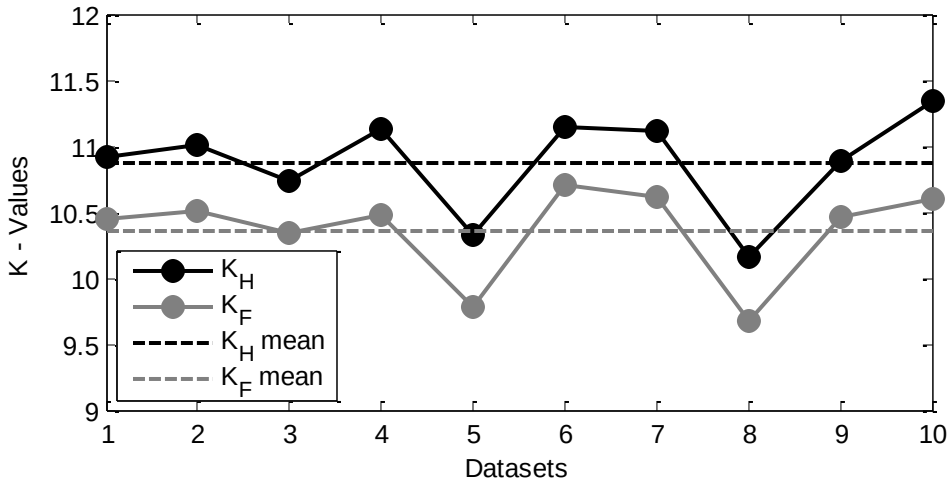

Figure 4.14 Variation of fault indicator for single-turn fault on secondary side under R type 50 % load

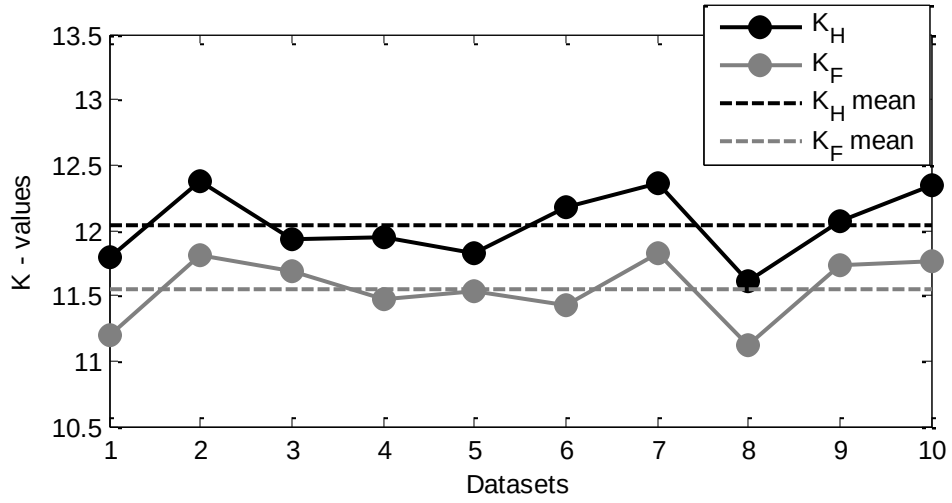

Figure 4.15 Variation of fault indicator for a single-turn fault on secondary side under RL type 50 % load

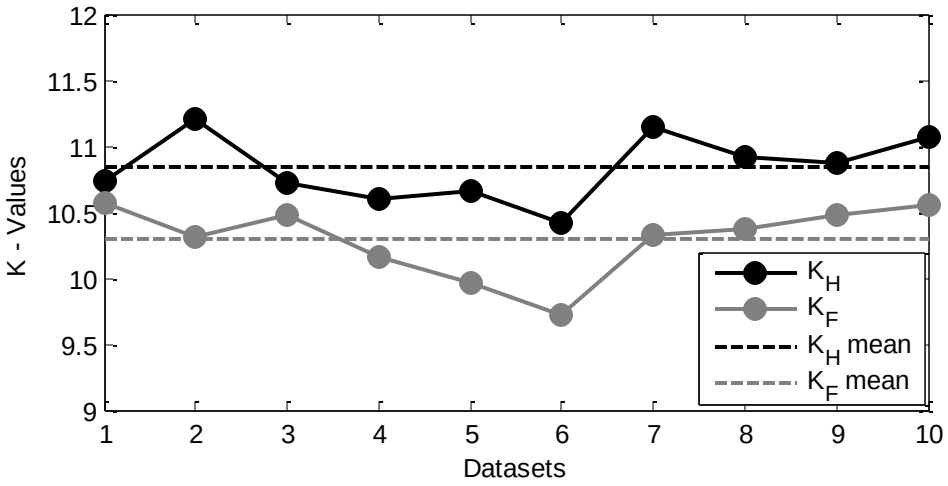

Figure 4.16 Variation of fault indicator for a single-turn fault on secondary side under RC type 50 % load

Type of load	$(K_H)_{mean}$	$(K_F)_{mean}$	Difference
R	10.87455	10.36178	0.51277
RL	12.04073	11.55462	0.48611
RC	10.83393	10.29115	0.54278

Table 4.3 Variation of the arithmetic mean values of the fault indicator for a single-turn fault on secondary side under 50 % load

4.2.2.1.4 Fault detection under 25 % load condition

Experiments were conducted following exactly the same procedure for 25 % load level and the variation of the fault indicator in case of R (unity p.f.), RL (0.8 p.f. lagging) and RC (0.8 p.f. leading) types of load are presented in Figures 4.17-4.19. This is followed by Table 4.4 which shows the average values of K_H and K_F and their differences for the 25 % load condition.

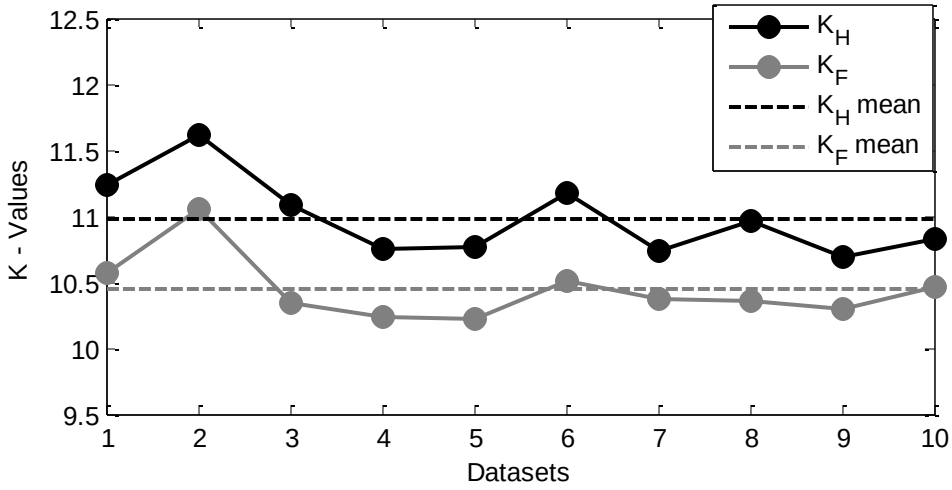

Figure 4.17 Variation of fault indicator for a single-turn fault on secondary side under R type 25 % load

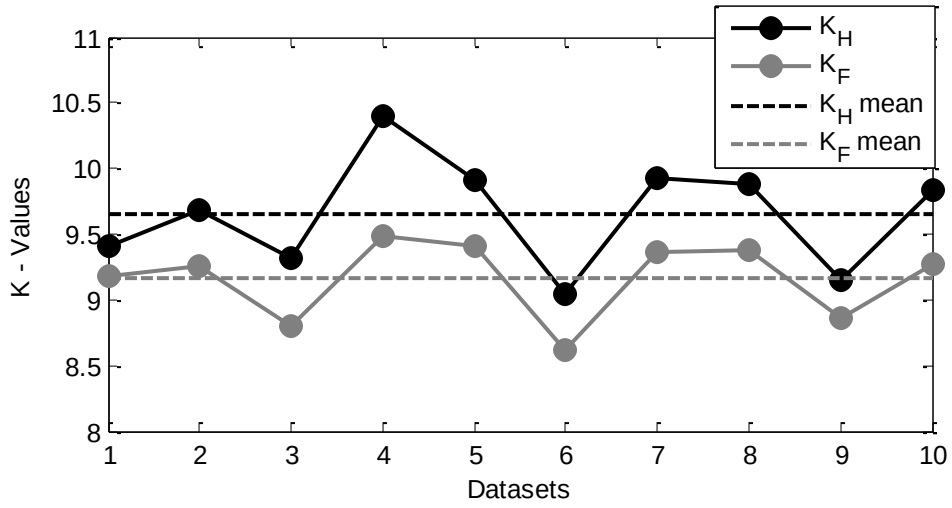

Figure 4.18 Variation of fault indicator for a single-turn fault on secondary side under RL type 25 % load

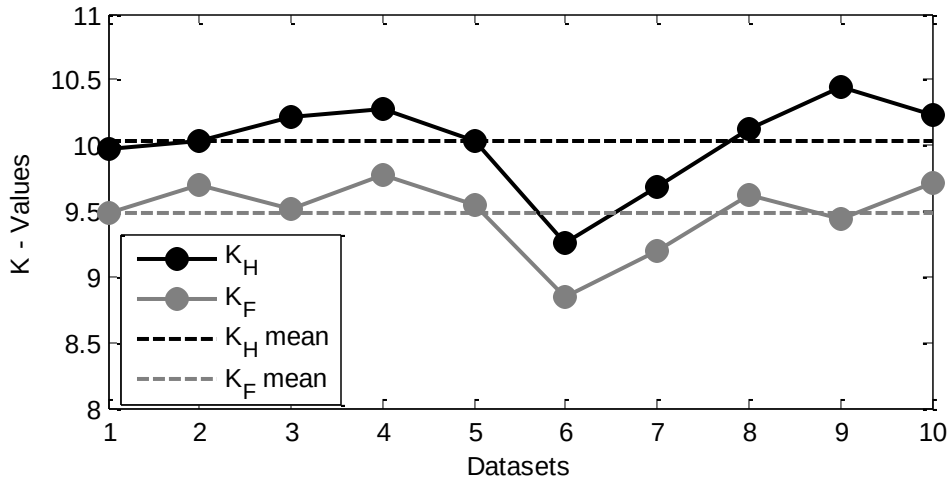

Figure 4.19 Variation of fault indicator for a single-turn fault on secondary side under RC type 25 % load

Type of load	$(K_H)_{mean}$	$(K_F)_{mean}$	Difference
R	10.98290	10.44237	0.54053
RL	9.65619	9.16045	0.49574
RC	10.02905	9.48316	0.54589

Table 4.4 Variation of the arithmetic mean values of the fault indicator for a single-turn fault on secondary side under 25 % load

4.2.2.1.5 Fault detection under no-load operation

An experiment was also conducted for no-load operation of the transformer and the variation of the fault indicator in this case is presented in Figures 4.20. This is followed by Table 4.5 which shows the average values of K_H and K_F and their difference for the no-load condition.

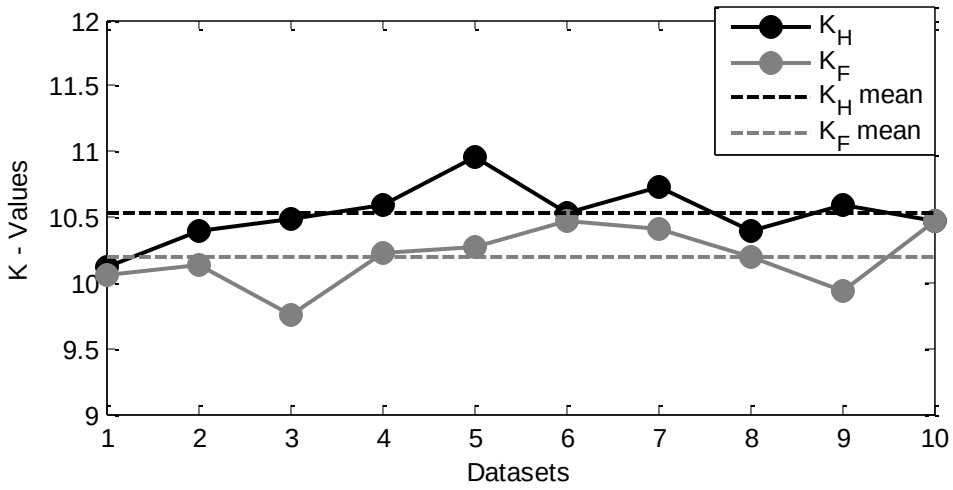

Figure 4.20 Variation of fault indicator for a single-turn fault on secondary side under no-load

$(K_H)_{mean}$	$(K_F)_{mean}$	Difference
10.52543	10.19357	0.33186

Table 4.5 Variation of the arithmetic mean values of the fault indicator for a single-turn fault on secondary side under no-load

4.2.2.2 Detection of single-turn fault on primary side

For this set of experiments, windings 1 and 2 of Figure 4.2 were considered as the secondary and primary sides respectively. 120 V, 60 Hz supply available in the laboratory was fed to winding 2, while winding 1 was either connected to different types and levels of load or left open-circuited in case of no-load operation. Here also, all the experiments were conducted strictly following the four steps described earlier.

4.2.2.2.1 Fault detection under on-load operation

An experiment was conducted for R type full-load operation of the transformer, with a single turn being shorted on the primary side. The variation of the fault indicator has been presented in Figure 4.21. The fault indicator value decreases in case of an inter-turn fault on the primary side as well. Similar trend in the fault indicator values is observed for faults on primary as well as

secondary windings. The second row of Table 4.6 shows the average values of K_H and K_F and their difference for this particular case. The trend in the fault indicator values remains consistent for single-turn faults on the primary side not only under RL and RC types of full-load; but also under any other levels or types of load.

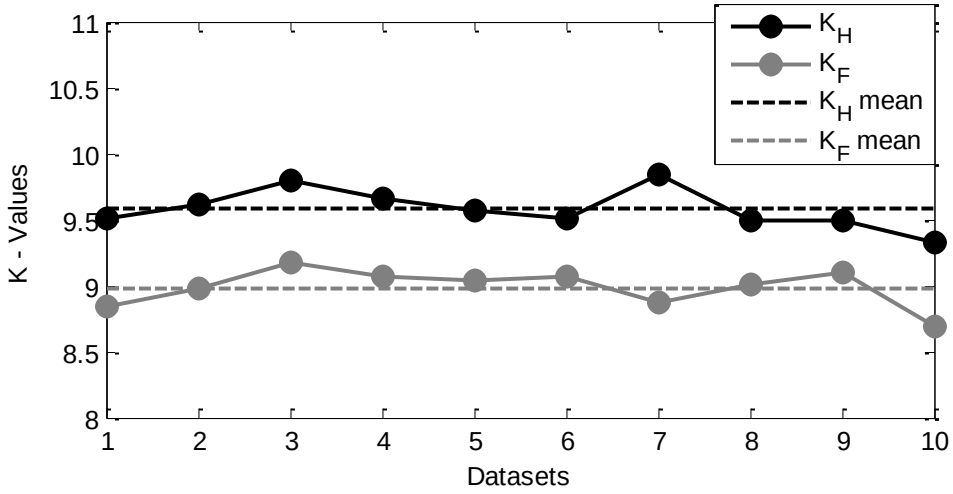

Figure 4.21 Variation of fault indicator for a single-turn fault on primary side under R type full-load

4.2.2.2.2 Fault detection under no-load operation

Variation in the fault indicator values and also their averages for this particular case has been presented in Figure 4.22 and Table 4.6 (third row) respectively, demonstrating similar trends as seen in the previous experimental results.

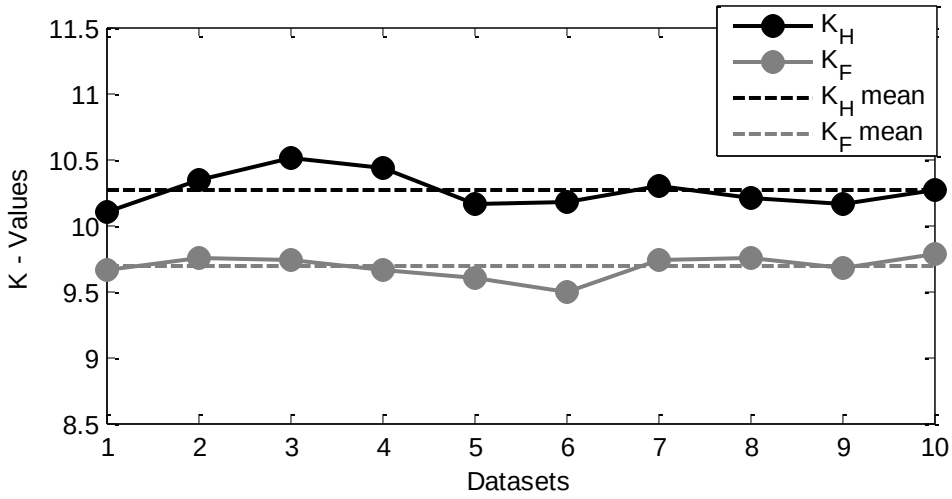

Figure 4.22 Variation of fault indicator for a single-turn fault on primary side under no-load

Type and level of load	$(K_H)_{mean}$	$(K_F)_{mean}$	Difference
R type full-load	9.58150	8.98331	0.59819
No-load	10.26212	9.68335	0.57877

Table 4.6 Variation of the arithmetic mean values of the fault indicator for a single-turn fault on primary side under R type full-load and no-load

4.2.3 Detection of fault severity

It has been already shown through experimental results in the previous subsection, that the modified fault detection scheme detects incipient faults such as a single-turn winding fault under all levels and types of load. Also, incipient faults occurring both on the primary and secondary windings are detected with similar sensitivity. In this subsection, the modified scheme has been extended to estimate fault severity by conducting the experiments with higher number of turns shorted on the primary and secondary windings. Then for each case, the fault indicator values have been computed under healthy and faulty states and comparisons have been made.

4.2.3.1 Detection of severity of fault on secondary side

Variation of the fault indicator in case of a single-turn fault on the secondary side under R type full-load operation has been already presented in Figure 4.8. However, the variations of the fault indicator for the same operating condition are much more significant in case of faults involving more turns. This is evident from Figures 4.23-4.26, which show the variations for 2-turn, 3-turn, 4-turn and 5-turn faults on the secondary side respectively.

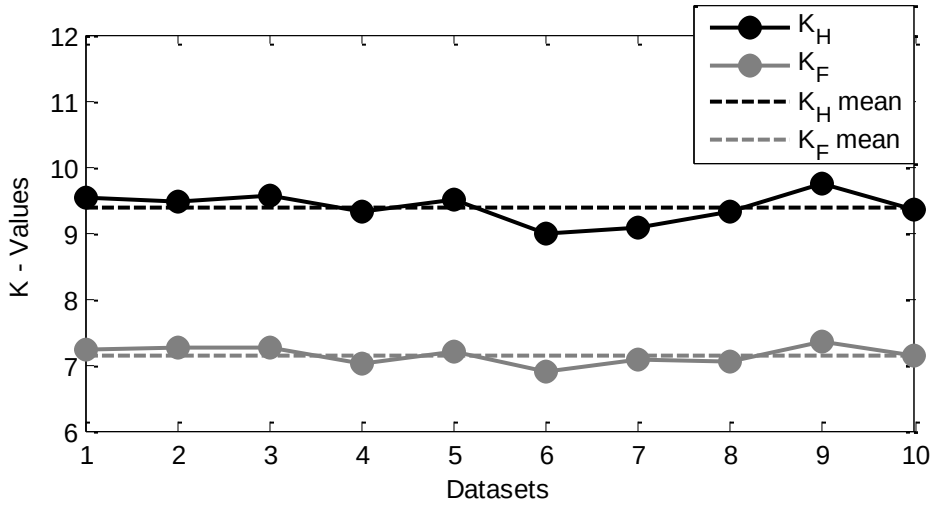

Figure 4.23 Variation of fault indicator for a 2-turn fault on secondary side under R type full-load

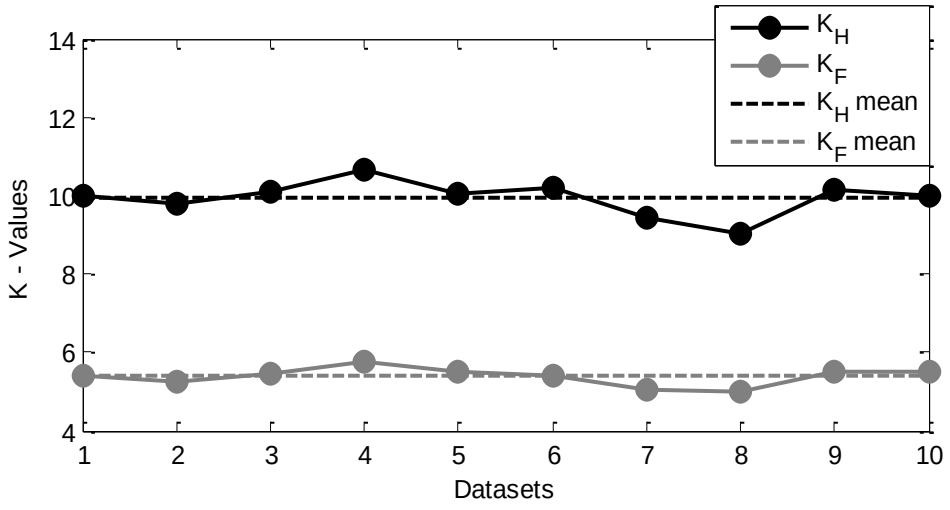

Figure 4.24 Variation of fault indicator for a 3-turn fault on secondary side under R type full-load

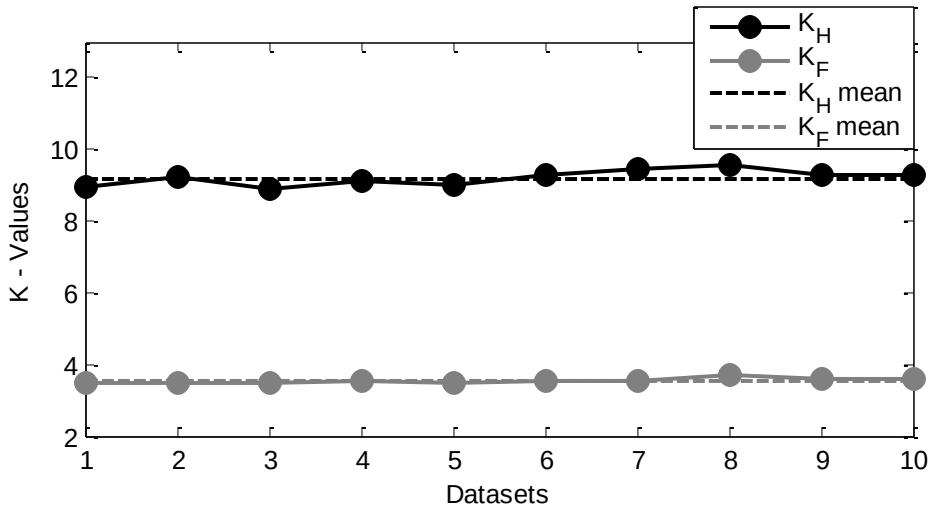

Figure 4.25 Variation of fault indicator for a 4-turn fault on secondary side under R type full-load

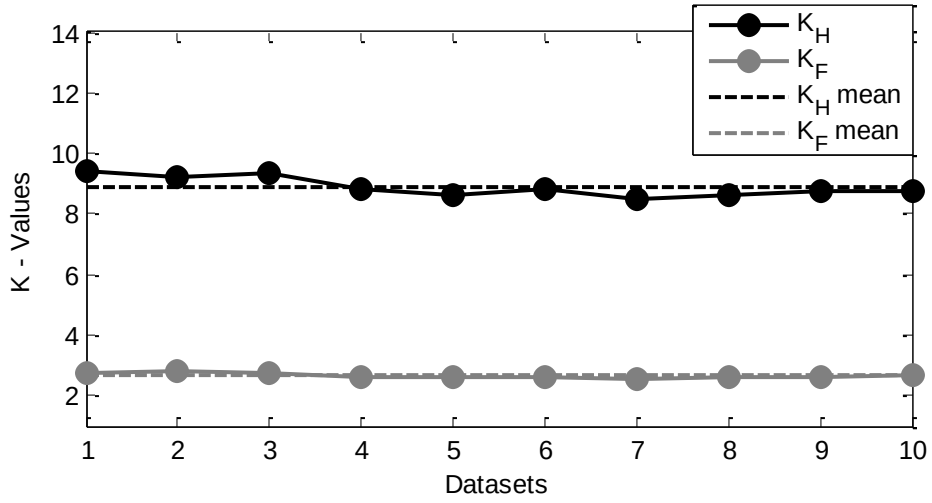

Figure 4.26 Variation of fault indicator for a 5-turn fault on secondary side under R type full-load

This is followed by Table 4.7 which shows the average values of K_H and K_F and their difference for these severe fault cases. The second row representing '0' turns shorted in the table corresponds to the healthy operation case. For this case in particular, two average values of K_H obtained from separate healthy datasets have been shown along with their difference. This has been done in order to show that the fluctuations in the fault indicator values under healthy

operation of the transformer are very close to zero. As expected, the difference between the K_H and K_F mean values increases, with increasing number of shorted turns.

Severity of fault	**$(K_H)_{mean}$**	**$(K_F)_{mean}$**	**Difference**
0 turn (Healthy)	$((K_H)_{mean})_1$ = 10.00926	$((K_H)_{mean})_2$ = 10.06656	0.05730
1 turn	11.08224	10.45769	0.62455
2 turn	9.38520	7.14707	2.23813
3 turn	9.94626	5.37928	4.56698
4 turn	9.20220	3.53888	5.66332
5 turn	8.87795	2.66180	6.21615

Table 4.7 Variation of the arithmetic mean values of the fault indicator for severe faults on secondary side under R type full-load

Similarly, the variation of the fault indicator values in case of a single-turn fault on the secondary side under no-load operation has been already presented in Figure 4.20. The fault indicator values for the same operating condition in case of faults with more number of turns have been presented in Figures 4.27-4.30. This is followed by Table 4.8 which shows the average values of K_H and K_F and their differences for these severe fault cases. Here as well, the second row representing '0' turns shorted in the table corresponds to the healthy operation case. For this case in particular, two average values of K_H obtained from separate healthy datasets have been shown along with their difference. This has been done to corroborate the fact that fluctuations in the fault indicator values under healthy operation of the transformer are very close to zero. From these results, it is evident that the difference between the K_H and K_F mean values increases monotonically, with increasing number of shorted turns even under no-load operation of the transformer.

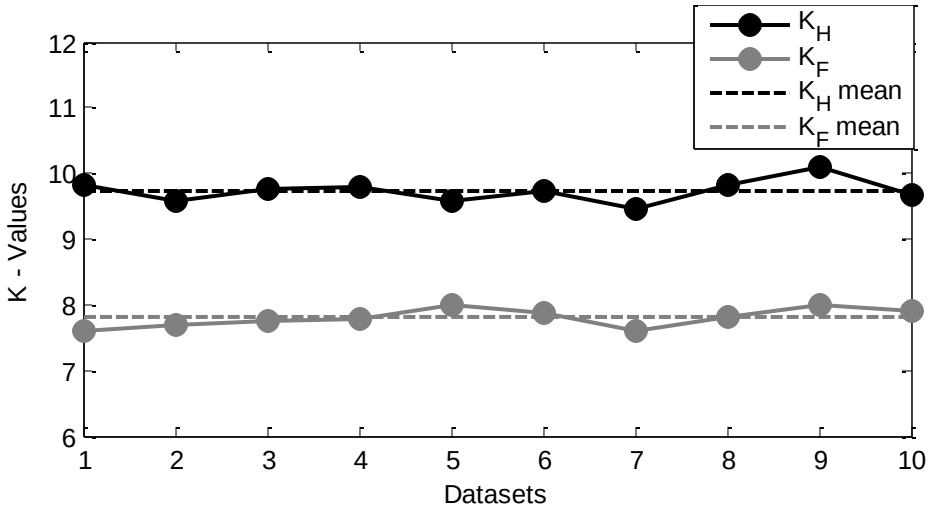

Figure 4.27 Variation of fault indicator for a 2-turn fault on secondary side under no-load

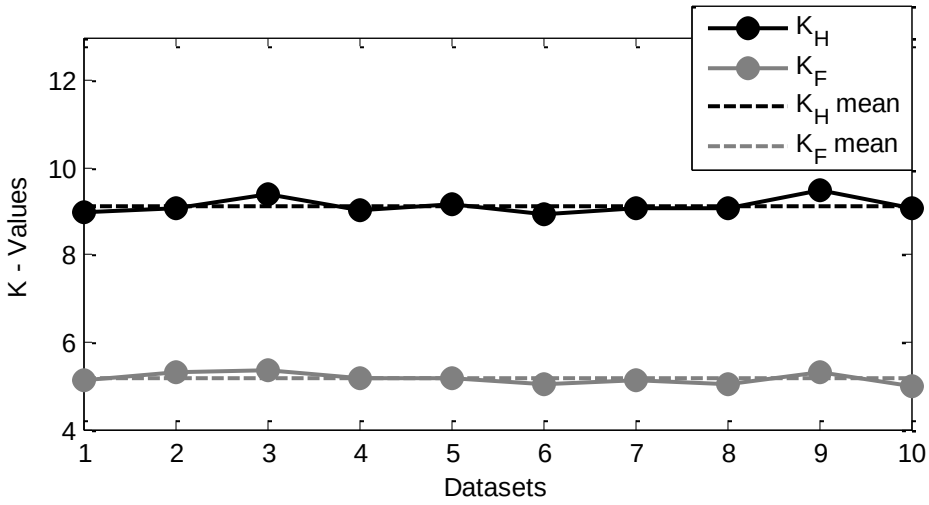

Figure 4.28 Variation of fault indicator for a 3-turn fault on secondary side under no-load

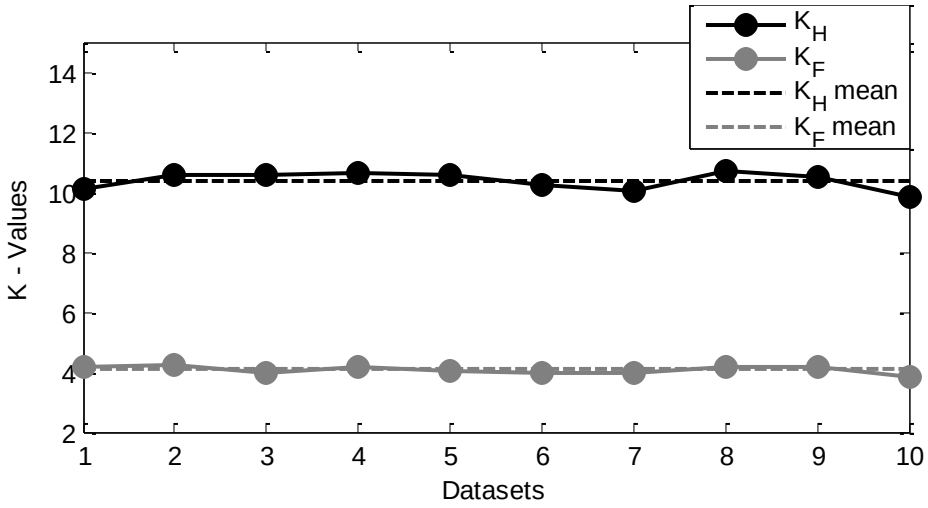

Figure 4.29 Variation of fault indicator for a 4-turn fault on secondary side under no-load

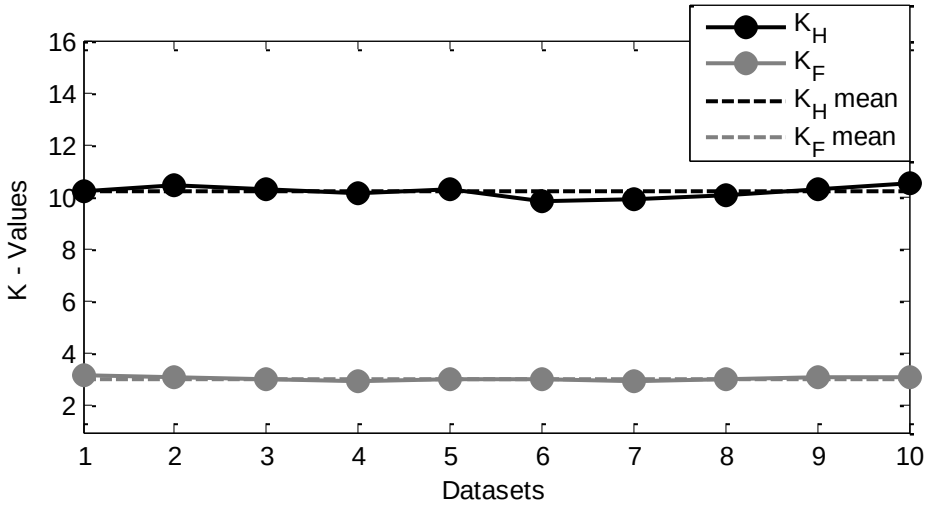

Figure 4.30 Variation of fault indicator for a 5-turn fault on secondary side under no-load

Severity of fault	$(K_H)_{mean}$	$(K_F)_{mean}$	Difference
0 turn (Healthy)	$((K_H)_{mean})_1 = 9.74959$	$((K_H)_{mean})_2 = 9.79885$	0.04926
1 turn	10.52543	10.19357	0.33186
2 turn	9.72792	7.80442	1.92350
3 turn	9.12831	5.16185	3.96646
4 turn	10.36948	4.07108	6.29840
5 turn	10.21314	3.05396	7.15918

Table 4.8 Variation of the arithmetic mean values of the fault indicator for severe faults on secondary side under no-load

4.2.3.2 Detection of severity of fault on primary side

Variation of the fault indicator values in case of single-turn faults on the primary side during the R type full-load and no-load operations of the transformer have been already shown in Figures 4.21 and 4.22 respectively. Under these two operating conditions, faults involving more turns were also created on the primary winding of the transformer and the modified fault detection scheme was tested for accurately detecting these faults. Here also winding 2 of Figure 4.2 was considered to be the primary side and was connected to the 120 V, 60 Hz laboratory power supply while winding 1 was connected to the load or left open-circuited.

Figures 4.31-4.34 show the variations in the fault indicator values for 2-turn, 3-turn, 4-turn and 5-turn faults on the primary side respectively, under R type full-load operation of the transformer. Then similar variations in the fault indicator values for the exact same fault levels under no-load operation of the transformer have been presented in Figures 4.35-4.38. From these figures, it is clearly seen that the variations in the fault indicator values increase, as the fault severity increases. This is corroborated in Tables 4.9 and 4.10, which show the average values of K_H and K_F and their differences for severe faults on the primary side, under R type full-load and no-load operations respectively. Thus, the modified fault detection scheme is highly efficient in estimating the severity of inter-turn faults on both primary and secondary windings of the transformer, under all types and levels of load. Here as well, the fluctuations in the fault indicator

values under healthy operation of the transformer have been shown to be very close to zero (second row of the tables).

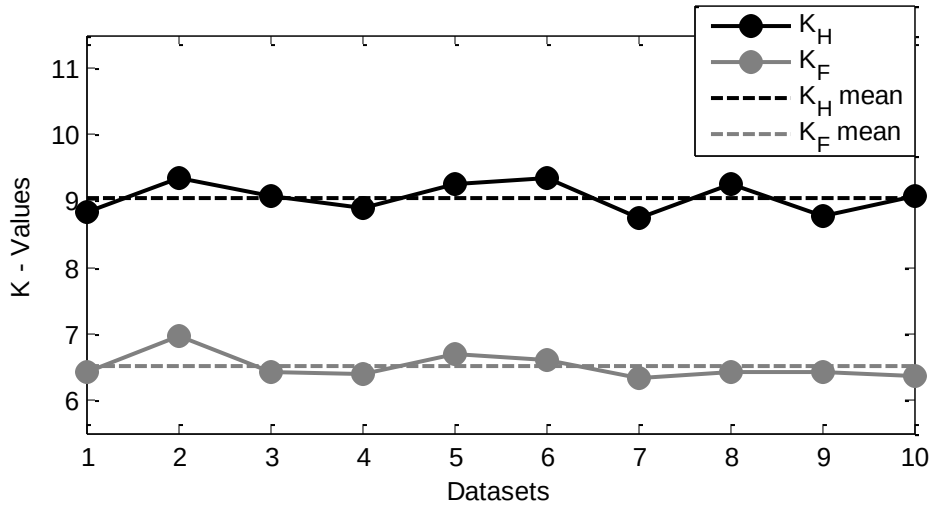

Figure 4.31 Variation of fault indicator for a 2-turn fault on primary side under R type full-load

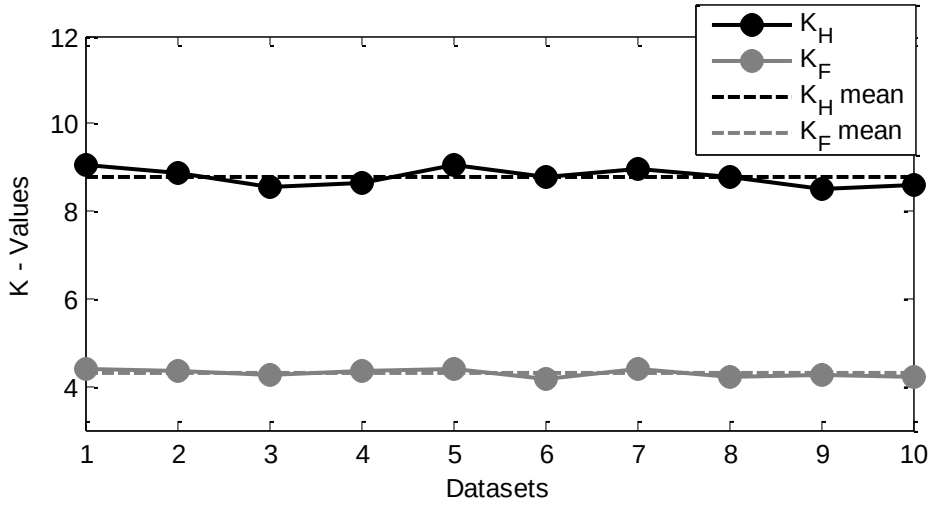

Figure 4.32 Variation of fault indicator for a 3-turn fault on primary side under R type full-load

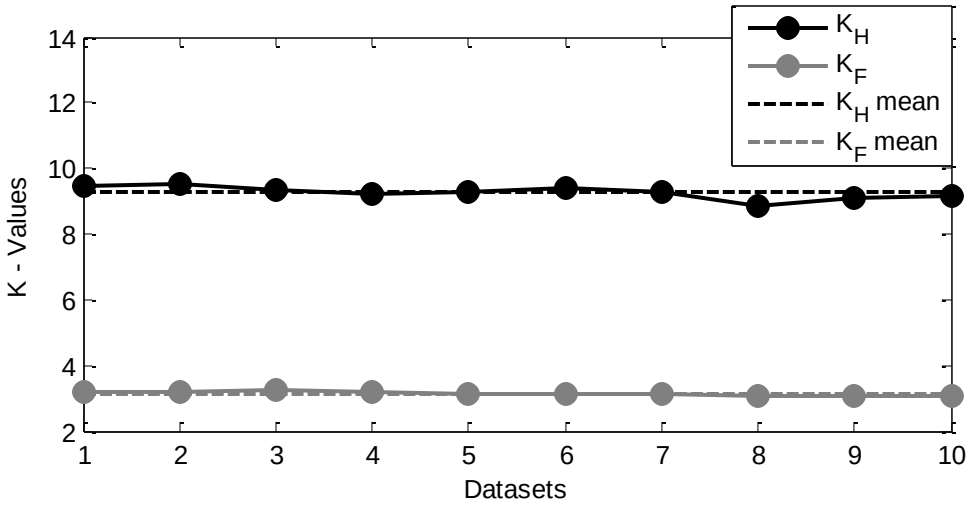

Figure 4.33 Variation of fault indicator for a 4-turn fault on primary side under R type full-load

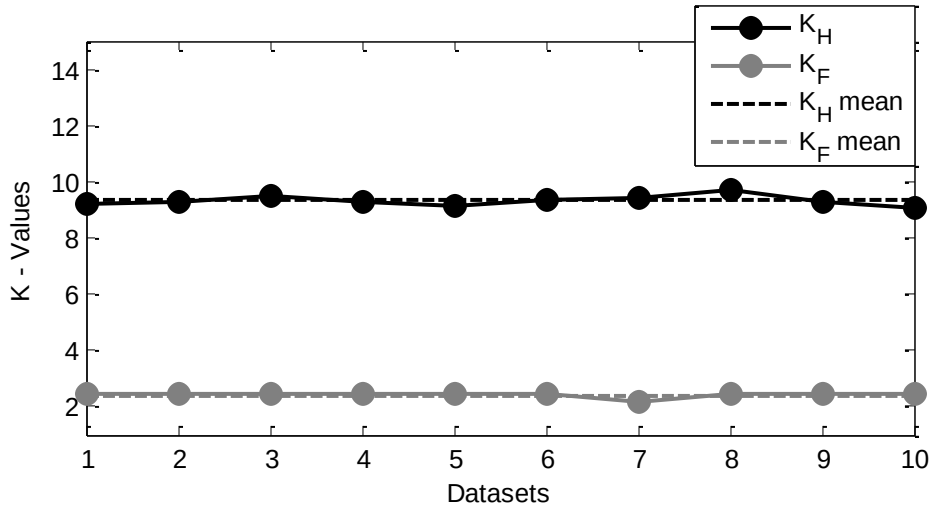

Figure 4.34 Variation of fault indicator for a 5-turn fault on primary side under R type full-load

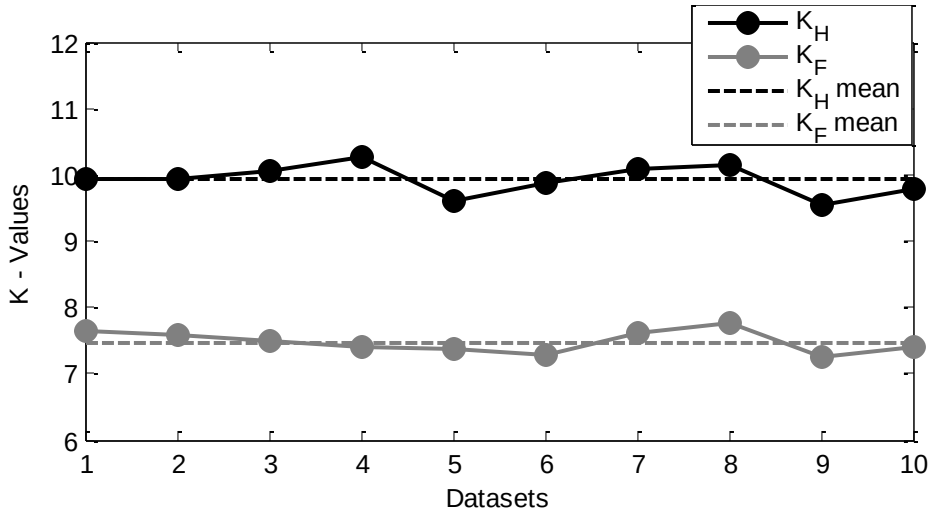

Figure 4.35 Variation of fault indicator for a 2-turn fault on primary side under no-load

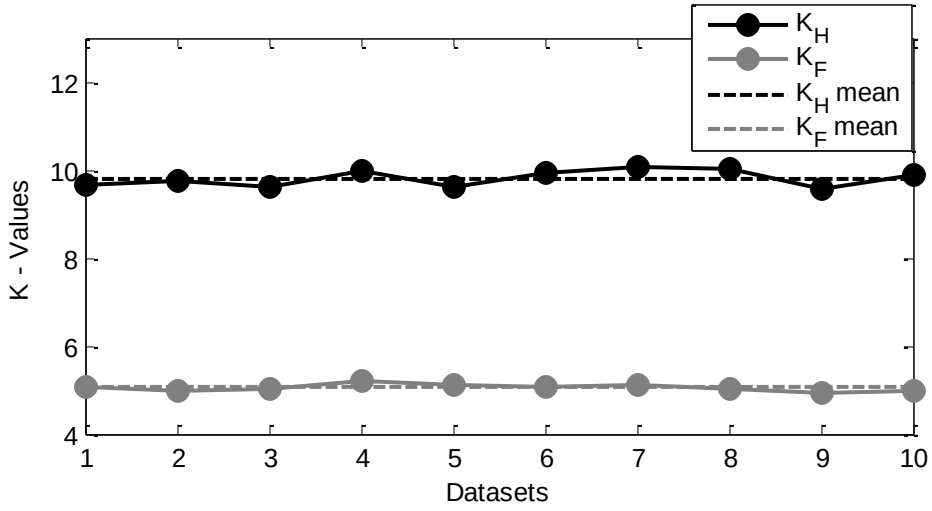

Figure 4.36 Variation of fault indicator for a 3-turn fault on primary side under no-load

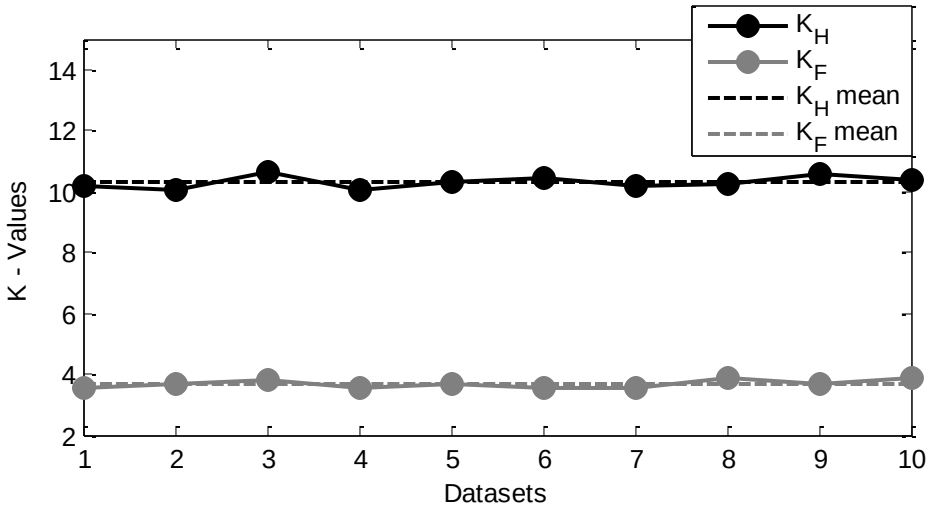

Figure 4.37 Variation of fault indicator for a 4-turn fault on primary side under no-load

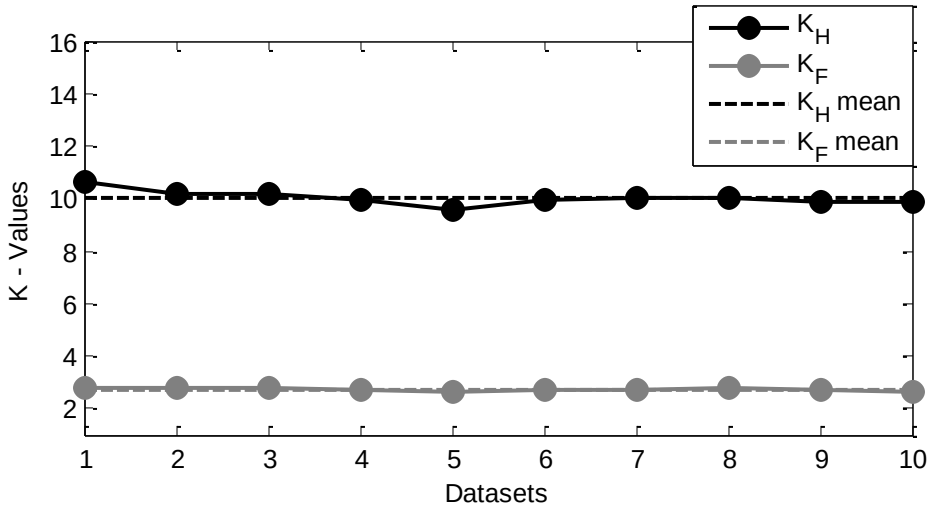

Figure 4.38 Variation of fault indicator for a 5-turn fault on primary side under no-load

Severity of fault	$(K_H)_{mean}$	$(K_F)_{mean}$	Difference
0 turn (Healthy)	$((K_H)_{mean})_1$ = 9.61757	$((K_H)_{mean})_2$ = 9.65365	0.03608
1 turn	9.58150	8.98331	0.59819
2 turn	9.05499	6.50182	2.55317
3 turn	8.77549	4.30628	4.46921
4 turn	9.26554	3.14433	6.12121
5 turn	9.31906	2.41984	6.89922

Table 4.9 Variation of the mean values of the fault indicator for severe faults on primary side under R type full-load

Severity of fault	$(K_H)_{mean}$	$(K_F)_{mean}$	Difference
0 turn (Healthy)	$((K_H)_{mean})_1$ = 9.67818	$((K_H)_{mean})_2$ = 9.61695	-0.06123
1 turn	10.26212	9.68335	0.57877
2 turn	9.92442	7.47630	2.44812
3 turn	9.80407	5.05442	4.74965
4 turn	10.30604	3.68330	6.62274
5 turn	10.01605	2.73917	7.27688

Table 4.10 Variation of the mean values of the fault indicator for severe faults on primary side under no-load

Figure 4.39 clearly demonstrates the increasing variations in the fault indicator mean values, with increase in the fault severity. The x-axis represents the fault severity i.e. number of turns shorted on the primary or secondary windings. The y-axis represents difference between the K_H and K_F mean values. The x-coordinate representing '0' turns shorted in this figure corresponds to the healthy operation case. The y-coordinate particularly corresponding to the healthy case represents the difference between two $(K_H)_{mean}$ values obtained from two separate healthy

datasets. This has been done in order to show that fluctuations in the $(K_H)_{mean}$ values under healthy operation of the transformer are very close to zero.

It is evident from the figure that the monotonically increasing trend of the fault indicator variations with fault severity are consistent for faults occurring on both the primary and secondary windings, under loaded as well as no-load operations of the transformer. Also these differences are not much affected by load variations and the side on which the fault has occurred.

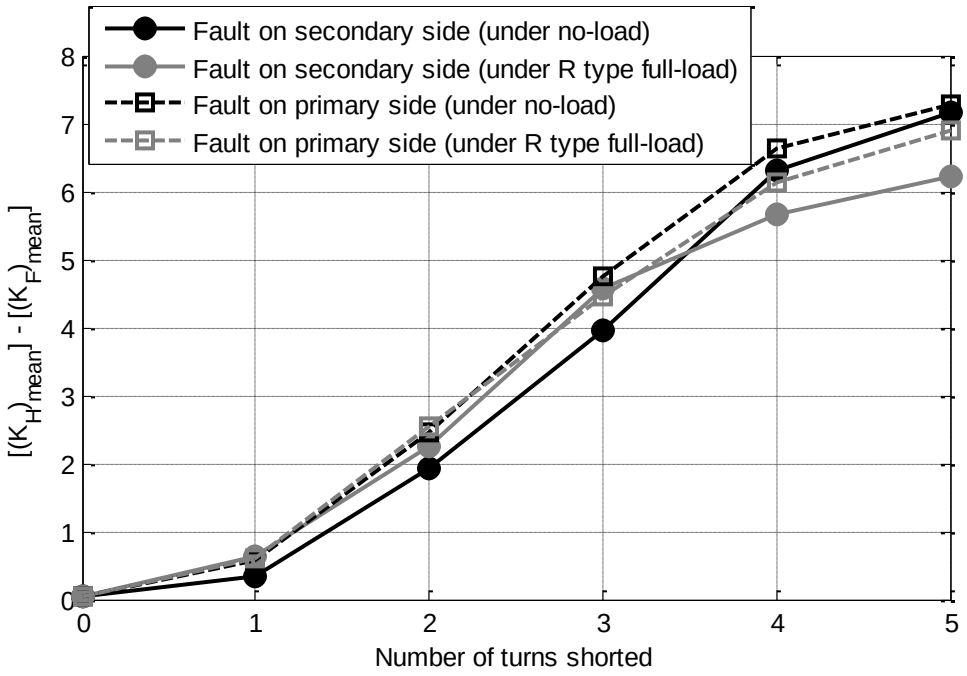

Figure 4.39 Plot of variations of fault indicator mean values with respect to the turns shorted on primary and secondary sides

4.2.4 Discussion of experimental results for fault detection

From the detailed experimental results presented in the previous subsection, it can be established that the modified fault detection scheme accurately detects incipient stages of inter-turn winding faults on both the primary and secondary sides of the transformer, under all types or levels of load. The fault detection technique has been extended to show that it can be used to estimate

fault severity as well. The variations in the fault indicator values have been shown to be directly proportional to the severity of the fault. In other words, higher the number of turns shorted on the primary or secondary winding, higher is the difference between the fault indicator values corresponding to the healthy and faulty states. The experimental results show similarity with the simulation results presented in the previous chapter; thus, establishing the fact that the proposed fault detection technique holds good promise.

Keeping these results in mind, it is worth discussing about the possible way in which the proposed technique can be implemented in a practical scenario for online, real-time and non-invasive condition monitoring and inter-turn winding fault diagnosis of single-phase distribution transformers. In the next chapter, one such implementation scheme has been described.

Chapter 5

Practical Implementation of the Modified Fault Detection Scheme

The modified fault detection scheme described in the previous chapter, has shown good promise in detecting inter-turn winding faults in single-phase transformers under any load condition. This has been verified through several experiments conducted under different levels and types of load while involving incipient as well as severe levels of fault. The scheme can be implemented in real-life for diagnosing inter-turn faults on a single-phase distribution transformer quite easily. The set-up needed for doing so is same as the one shown in Figure 4.1 in the previous chapter. The steps for the practical implementation of this scheme can be outlined as:

Step 1

Using necessary probes and a data acquisition system, the primary line voltage, primary and secondary line currents can be acquired and filtered for noise elimination. From the acquired line currents, the exciting current can be computed. Then, using the experimentally acquired voltage and exciting current, the experimental fault indicator value can be determined and stored for future comparison. On the other hand, the acquired primary line voltage needs to be analyzed further.

Step 2

By performing a single-sided complex FFT on the experimentally acquired primary line voltage data, the peak values and phase angles associated with its harmonic components can be obtained. Using this information, the experimentally acquired primary line voltage can be represented by an infinite series trigonometric expression as shown in (5.1), where ω is the angular frequency. It can incorporate any desired number of harmonics. Here, $(V_{IN})_1$, $(V_{IN})_3$, $(V_{IN})_5$ etc represent the peak values of the fundamental, 3rd, 5th and other harmonic components of the input voltage

respectively. Similarly, φ_1, φ_3, φ_5 etc represent the initial phase angles in radians associated with the fundamental, 3rd, 5th and other harmonic components of the input voltage respectively.

$$v_{IN}(t) = (V_{IN})_1 \cos(\omega t - \varphi_1) + (V_{IN})_3 \cos(3\omega t - \varphi_3) + (V_{IN})_5 \cos(5\omega t - \varphi_5) + \ldots. \quad (5.1)$$

Then, the voltage represented by (5.1) is substituted in the healthy models of the single-phase transformer for no-load or loaded conditions as per requirement. These models, which have already been derived in Chapter 2, can be simulated with the trigonometric representation of the acquired primary line voltage easily. From the simulated primary and secondary line currents, the healthy estimated exciting current can be obtained. Using the healthy estimated exciting current and the experimentally acquired primary line voltage, the healthy estimated fault indicator value (as defined by (4.2)) can be determined.

Step 3

The experimental fault indicator value of the single-phase transformer (already obtained and stored as part of step 1) is compared with the healthy estimated fault indicator value (obtained in step 2). The entire process involving the data acquisition, FFT of the acquired input voltage, simulation of the healthy transformer model using the acquired input voltage and comparison of the two fault indicator values can be automated and fully integrated; such that it is continuously repeated for every utility voltage cycle, provided the computation of the exciting current from the state space model is fast enough. One fully integrated process, starting from the data acquisition up to the comparison of fault indicator values, can be termed as a *health monitoring cycle* of the transformer. To save memory, the experimentally acquired data from Step 1 can be discarded at the end of a few *healthy monitoring cycles*. In this way, a quasi-real-time, online condition monitoring mechanism can be implemented.

If the transformer is in healthy state, then the two fault indicator values (experimental and healthy estimated ones) should be very close in case of all the *health monitoring cycles*. However, if the experimental fault indictor value is consistently lower than the healthy estimated fault indicator value for all of these consecutive *health monitoring cycles*; then it would be a clear indication of the presence of inter-turn winding fault(s).

5.1 Important considerations for the practical implementation of the scheme

Before the modified fault detection scheme can be extended for practical implementation following the three steps outlined earlier, some important factors need to be considered. These are described in this subsection.

5.1.1 Accuracy of healthy transformer model simulations with actual input voltages

In Chapter 2, it has been already shown that the healthy transformer model simulates the actual transformer quite accurately, with an arbitrary 120 V, 60 Hz purely sinusoidal supply voltage under no-load and loaded conditions. The simulated exciting current was very close in its RMS value and wave-shape to the actual/experimental exciting current. However, for practical implementation of the fault detection scheme, the healthy transformer model must be able to simulate the transformer's behaviour with similar level of accuracy, even when fed with an experimentally acquired primary line voltage data.

5.1.1.1 Accuracy of the healthy transformer models under on-load operation

To make sure that the healthy transformer models derived in Chapter 2 simulate accurately with actual voltage inputs, an experimentally acquired primary line voltage data has been considered. This data has been acquired using the data acquisition system [65] at a sampling frequency of 18 kHz under R type full-load operation of the transformer. Table 5.1 shows the complex representation of the odd harmonics in the supply voltage. This information has been obtained after performing single-sided FFT on a 1s sample of this voltage data. The supply voltage in the laboratory does not contain any even harmonics. Also, the peak values and initial phase angles of the voltage harmonics have been computed using rectangular to polar conversion. The 'abs' and 'angle' commands in MATLAB [66] have been used for the computations of the peak value and initial phase angle respectively.

Also, the initial phase angles associated with all the harmonic components have been normalized with respect to the initial phase angle of the fundamental voltage component, by using (5.2). In

(5.2), h represents the harmonic number; while (φ_h) and $[\varphi_h]_N$ represent the initial and normalized phase angles respectively, associated with any harmonic component.

$$[\varphi_h]_N = (\varphi_h) - h(\varphi_1) \tag{5.2}$$

Equation (5.1) gets modified to (5.3); where $[\varphi_1]_N$, $[\varphi_3]_N$, $[\varphi_5]_N$ etc represent the normalized phase angles associated with the fundamental, 3rd, 5th and other harmonics respectively. As the normalization is done with respect to the initial phase angle of the fundamental component itself, understandably $[\varphi_1]_N$ is equal to zero. Normalization of the initial phase angles is essential because the fundamental voltage is re-oriented such that the simulated exciting current always starts from zero. This is to ensure that any DC component as an initial condition does not exist in the simulated exciting current; which then can be compared with the experimentally acquired exciting current that has no DC component, with minimum possible simulation time.

$$v_{IN}(t) = (V_{IN})_1 \cos(\omega t - [\varphi_1]_N) + (V_{IN})_3 \cos(3\omega t - [\varphi_3]_N) + (V_{IN})_5 \cos(5\omega t - [\varphi_5]_N) + \ldots.$$

(5.3)

Harmonic number '*h*'	**Complex representation of voltage harmonics (V)**	**Peak values (V)**	**Initial phase angles (rad)**	**Normalized phase angles (rad)**
1 (Fundamental)	(89.48500) + j(141.04000)	167.0325	1.0054	0
3	(0.95633) + j(0.07342)	0.9591	0.0766	-2.9396
5	(2.90540) + j(-6.82110)	7.4141	-1.1681	-6.1951
7	(1.76590) + j(-2.44830)	3.0187	-0.9459	-7.9837
9	(0.24643) + j(-0.07169)	0.2566	-0.2831	-9.3317
11	(-0.33554) + j(1.53540)	1.5716	1.7859	-9.2735
13	(0.52589) + j(-0.00745)	0.5259	-0.0142	-13.0844
15	(0) + j(0)	0	0	-15.0810

Table 5.1 Representation of harmonics in experimentally acquired primary line voltage under R type full-load

The peak values and normalized phase angles of the voltage harmonics, obtained from columns 3 and 5 of Table 5.1 respectively, have been substituted in (5.3) in order to replicate the experimentally acquired primary line voltage under R type full-load operation of the transformer. Figure 5.1 provides a comparison of the experimentally acquired primary line voltage and its trigonometric representation given by (5.3) under R type full-load operation. The actual voltage had an RMS value of 118.42 V, while its trigonometric representation had that of 118.26 V. Thus the percentage error in the RMS value was only 0.135 %.

Subsequently, the healthy transformer model for R type full-load operation (already derived in Chapter 2) has been simulated using the trigonometric representation of the input voltage. The simulated primary line, secondary line and exciting currents have been compared with their experimentally acquired counter-parts in Figures 5.2-5.4 respectively. The corresponding currents are very close to each other in their respective wave-shapes and have extremely small percentage errors in their RMS values. Also, the fault indicator K_H values obtained from the experimental and simulation results are very close in magnitude, as shown in Table 5.3.

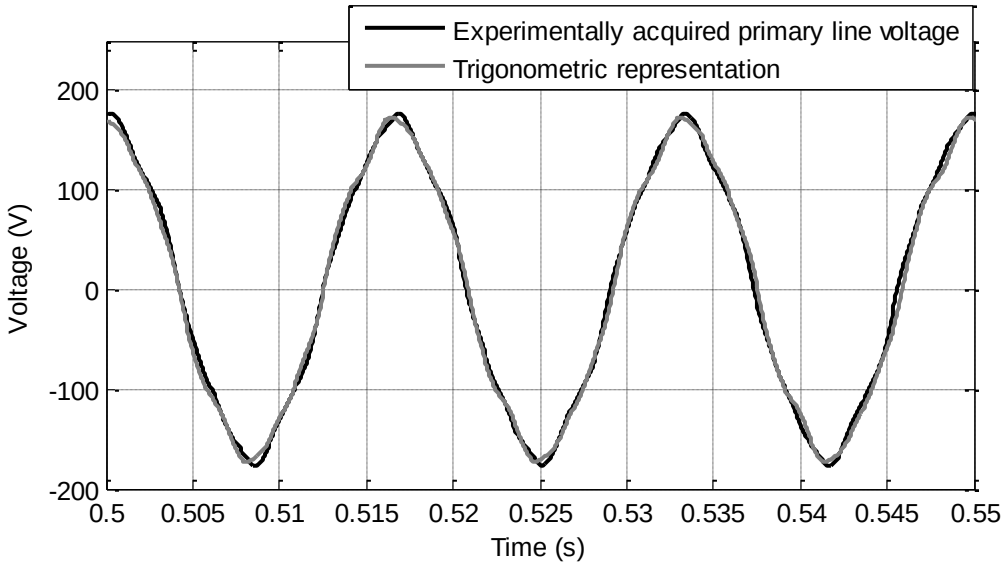

Figure 5.1 Comparison of the experimentally acquired primary line voltage and its trigonometric representation under R type full-load

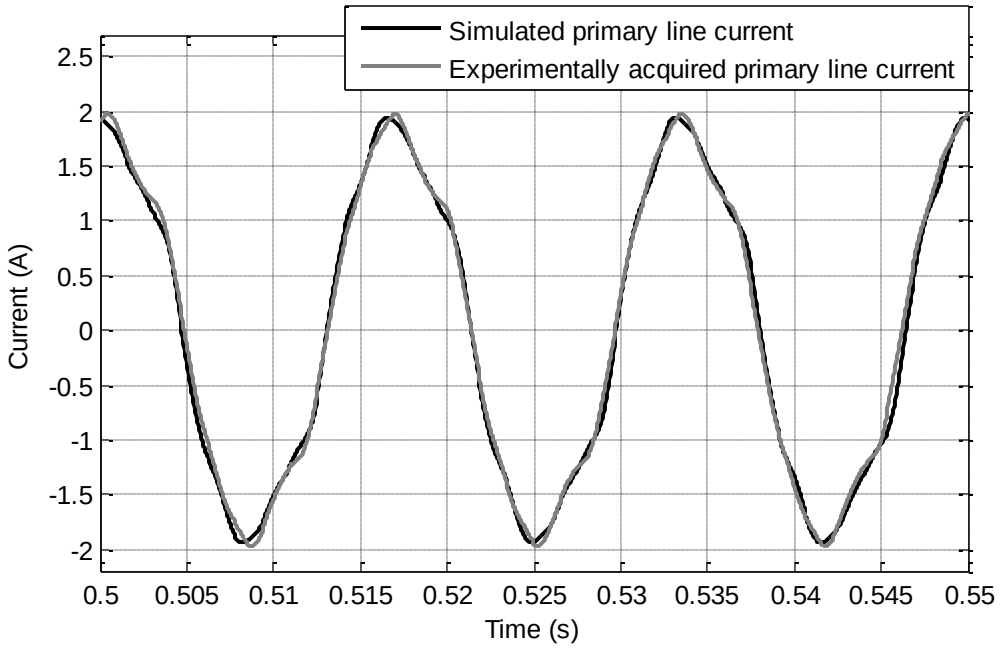

Figure 5.2 Comparison of the simulated (using the trigonometric representation of the acquired input voltage) and experimentally acquired primary line current under R type full-load

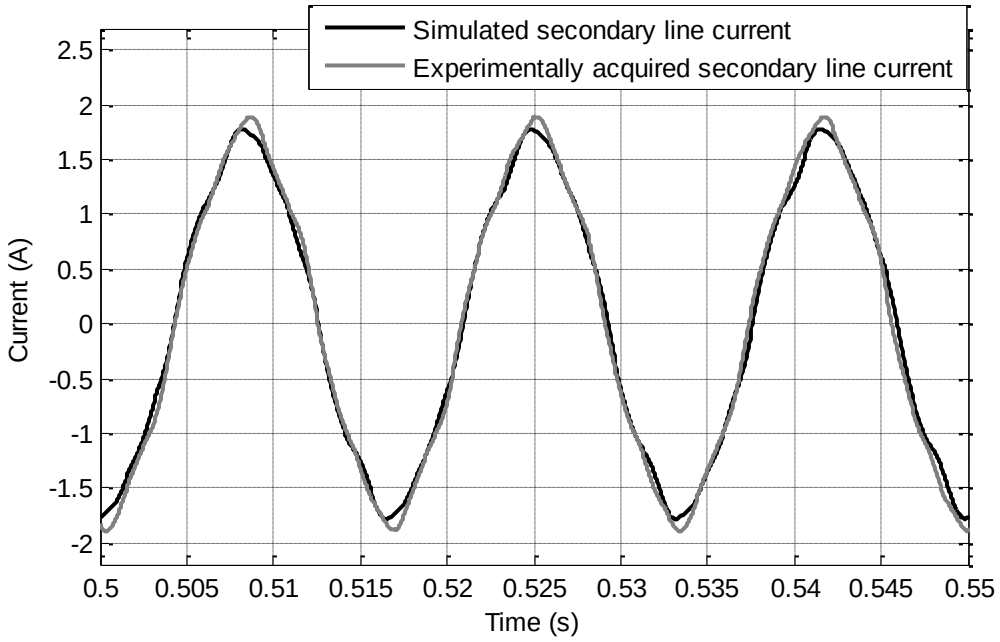

Figure 5.3 Comparison of the simulated (using the trigonometric representation of the acquired input voltage) and experimentally acquired secondary line current under R type full-load

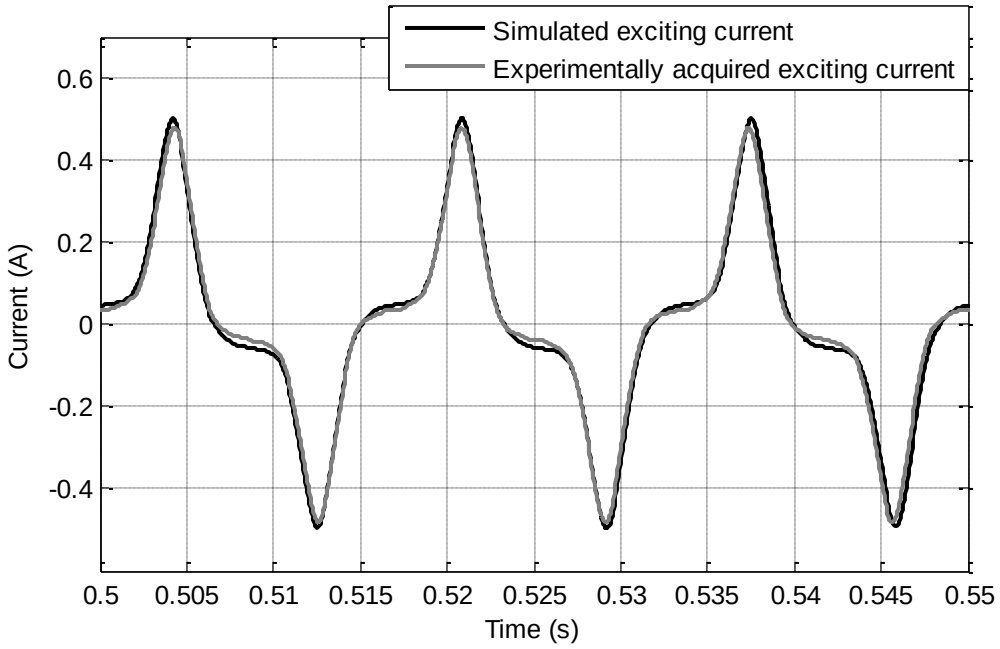

Figure 5.4 Comparison of the simulated (using the trigonometric representation of the acquired input voltage) and experimentally acquired exciting current under R type full-load

5.1.1.2 Accuracy of the healthy transformer model under no-load operation

Similarly, the primary line voltage data under no-load operation of the transformer has been acquired as well. Its harmonic content has also been investigated and shown in Table 5.2. Using the peak values and normalized phase angle information from Table 5.2, the primary line voltage under no-load operation has been replicated as well, using (5.3). Figure 5.5 provides a comparison of the experimentally acquired primary line voltage and its trigonometric representation given by (5.3). The actual voltage had an RMS value of 119.08 V, while its trigonometric representation had that of 118.30 V. The percentage error in the RMS value was only 0.66 %.

Thereafter, the healthy transformer model under no-load operation (already derived in Chapter 2) has been simulated using trigonometric representation of the input voltage. The simulated exciting current has been compared to its experimentally acquired counter-part in Figure 5.6. The corresponding currents are very close to each other in their wave-shapes and have extremely

small percentage errors in their RMS values. Also, the fault indicator K_H values obtained from the experimental and simulation results are very close in magnitude, as shown in Table 5.3.

Harmonic number '*h*'	**Complex representation of voltage harmonics (V)**	**Peak values (V)**	**Initial Phase angles (rad)**	**Normalized phase angles (rad)**
1 (Fundamental)	(-147.44000) + j(78.62400)	167.0936	2.6517	0
3	(0.81343) + j(0.92030)	1.2283	0.8470	-7.1081
5	(5.13040) + j(5.48370)	7.5095	0.8187	-12.4398
7	(-1.08790) + j(-2.51050)	2.7361	-1.9797	-20.5416
9	(-0.17965) + j(0.24172)	0.3012	2.2099	-21.6554
11	(0.87184) + j(1.46070)	1.7011	1.0327	-28.1360
13	(-0.48892) + j(0.30640)	0.5770	2.5818	-31.8903
15	(0) + j(0)	0	0	-39.7755

Table 5.2 Representation of harmonics in experimentally acquired primary line voltage under no-load

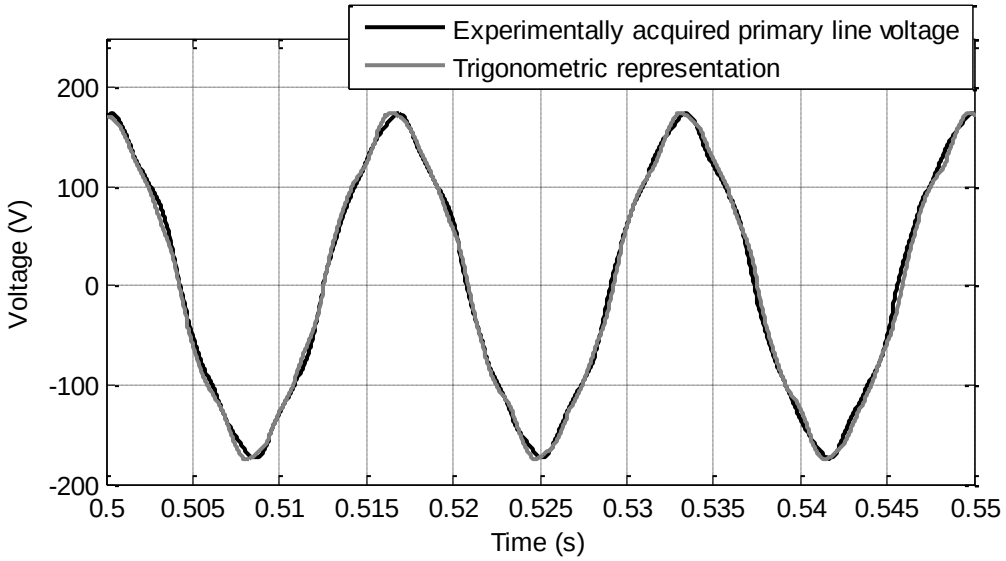

Figure 5.5 Comparison of the experimentally acquired primary line voltage and its trigonometric representation under no-load

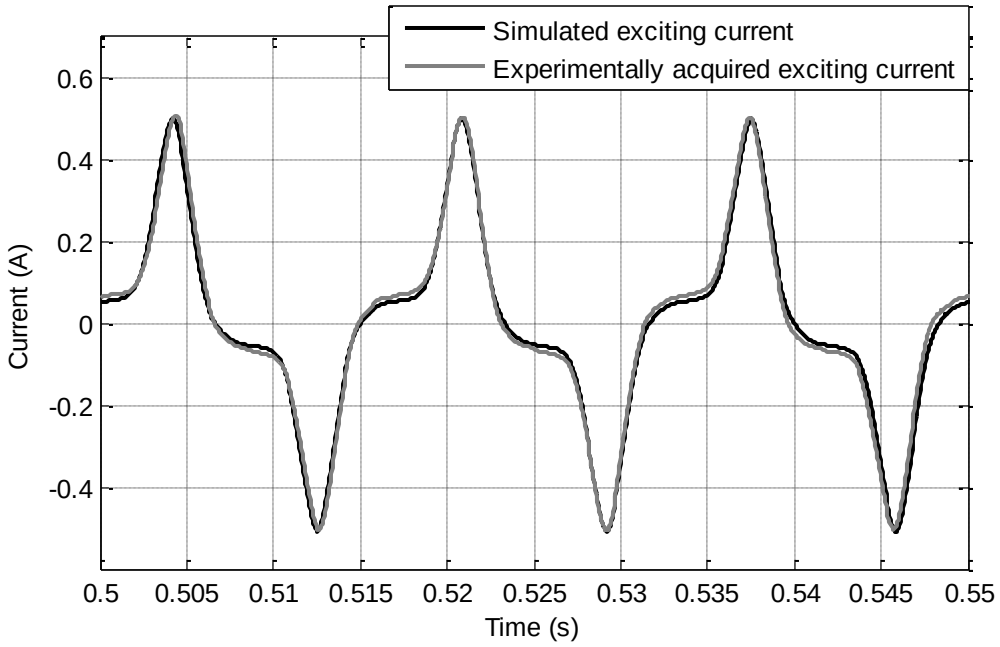

Figure 5.6 Comparison of the simulated (using the trigonometric representation of the acquired input voltage) and experimentally acquired exciting current under no-load

Operating condition	**Quantity**	**Simulated**	**Experimental**	**Percentage errors**
R type full-load	**Primary line current RMS**	1.31 A	1.34 A	2.24 %
	Secondary line current RMS	1.22 A	1.26 A	3.17 %
	Exciting current RMS	231.85 mA	228.40 mA	1.51 %
	K_H	11.05821	11.15335	0.85 %
No-load	**Exciting current RMS**	230.70 mA	234.56 mA	1.65 %
	K_H	10.99637	10.98206	0.13 %

Table 5.3 Comparison of simulation and experimental results

From the results summarized in Table 5.3, it can be easily concluded that the healthy single-phase transformer models simulates accurately under loaded as well as no-load conditions, when fed with the experimentally acquired primary line voltage data.

5.1.2 Program execution time of the healthy transformer models

For the practical implementation technique proposed in this chapter, it is essential that the healthy single-phase transformer models simulates as fast as possible for the real-time monitoring of the transformer health. This will also guarantee a much faster detection of an inter-turn winding fault and hence, will increase the reliability of the modified fault detection scheme. The program execution time of the transformer model depends greatly on the number of computations involved in solving the state space equations describing the transformer itself. In other words, the simulation time depends on the number of state variables involved in the model.

The healthy transformer models discussed so far are of three types:

- Type A model: Model for no-load (with one state variable)
- Type B model: Models for R and RL type loads (with two state variables)
- Type C model: Model for RC type load (with three state variables).

Simulations of these three types of healthy transformer models were run on a PC with a Pentium 4, 3 GHz processor and the program execution times were recorded. 'ode23tb' solver was used and the state space models were solved using a time-step of 1/3600 of a second. For maintaining consistency in the comparisons, all the models were simulated with a 120 V, 60 Hz sinusoidal input voltage supply. The results are presented in Table 5.4 and it is clear that the models simulate within very short time durations. It is understandable that on a faster computing platform, the healthy transformer models will have even lower program execution times. This makes the proposed scheme highly suitable for continuous online condition monitoring based applications.

Simulation time duration (s)	**Program execution time (s)**		
	Type A model (No-load)	**Type B model (R and RL type loads)**	**Type C model (RC type load)**
1	2.795	3.416	4.188
2	5.594	6.829	8.375

Table 5.4 Comparison of program execution times for the healthy transformer models

In Sub-sections 5.1.1 and 5.1.2, it has been shown that the healthy transformer models simulate with a very high degree of accuracy when fed with the experimentally acquired primary line voltage under any load conditions; that too with very low program execution times. However, one important issue still need to be addressed for enabling the real-time, online and automated implementation of the modified fault detection scheme. Based on the type and level of load connected to the secondary side, the appropriate healthy transformer model needs to be selected for running the simulation; and in order to perform this action an additional decision-making arrangement need to be incorporated in the fault detection scheme. Basically, there should be some means for determining the power factor and level of load; and then one amongst the no-load, R type, RL type or RC type models should be selected. Also, it is difficult to incorporate rectifier-type loads in these state space transformer models, thereby constraining the application of the fault detection scheme in case of such loads. In the next subsection, this important issue is addressed and an appropriate solution is discussed.

5.1.3 Use of only the no-load healthy transformer model for fault detection

The computation of the fault indictor values is based on the excitation current and the primary line voltage of the single-phase transformer; thus it is completely independent of the level and type of load. This indicates that the simulation of the healthy no-load transformer model can be deemed as sufficient in providing an accurate estimate of the exciting current under any load condition and therefore, can be used for computing the simulated K_H estimates.

The above statement is corroborated in Table 5.5 where the K_H values, obtained from simulation of the no-load and R type full-load transformer models fed with the same input voltage, have been compared. The input voltages represented by V_1 and V_2 in the 2nd and 3rd rows of Table 5.5 are nothing but the experimentally acquired voltages previously given in Tables 5.1 and 5.2 respectively. It is evident that the K_H values obtained from the two simulations are very close, as their percentage errors are well within 0.5 %. This emphasizes the fact that the healthy no-load transformer model can be used for providing an accurate estimate of the exciting current of the transformer under any load condition.

Primary line voltage samples fed to the models	K_H values		Percentage errors
	Simulation using no-load model	Simulation using R type full-load model	
V_1	11.08053	11.05821	0.20 %
V_2	10.99637	11.03447	0.34 %

Table 5.5 Comparison of fault indicator values for simulations using no-load and R type full-load healthy transformer models

Using only the no-load healthy transformer model for the computation of healthy estimated exciting current to detect faults under any load condition, has the following advantages:

- As the no-load healthy model is the simplest state space model with only one state variable (which is the magnetizing current of the transformer), the program execution time of the no-load model is much lower as compared to that of the other models incorporating R, RL and RC type loads (already shown in Table 5.4). The necessary computational power and memory requirements are comparatively less as well.

- With the advent of switching power supplies, distribution transformers today are required to supply power to an increasing number of rectifier loads. Incorporation of such loads in the state space transformer models (derived in the previous chapters) for fault detection purposes are complicated. However, use of the no-load healthy transformer model for computing the healthy estimated exciting current, helps to tackle this problem.

In Section 5.1, various important considerations for the practical implementation of the modified fault detection scheme have been discussed. Based on these considerations, the scheme can be easily implemented in most modern-day Real-Time High Performance Computing (RTHPC) platforms comprising of multi-core processors capable of parallel and distributed computing [79, 80]. This will enable real-time monitoring of the transformer's health on-site as well as from remote locations. In the next section some examples of practical implementation of the scheme, following the steps mentioned previously, have been provided.

5.2 Examples of practical implementation of fault detection scheme

To validate the effectiveness of the modified fault detection scheme for diagnosing single-turn short-circuit faults in single-phase transformers, six test conditions have been considered.

For each test condition, data acquisition under healthy and faulty states has been done followed by necessary data processing in order to compute the experimental fault indicator values. These values for the healthy and faulty states have been termed as $(K_H)_{EXPT}$ and $(K_F)_{EXPT}$ respectively. Then, the healthy no-load transformer model has been simulated using the acquired primary line voltage under healthy state; consequently computing the first estimated fault indicator value $(K_H)_{EST1}$. The difference D_1 between $(K_H)_{EST1}$ and $(K_H)_{EXPT}$ provides a measure of the simulation accuracy under healthy operation. The closer is the value of D_1 to zero, the more accurate is the transformer model. Finally, the transformer model has been simulated again, this time using the acquired voltage under faulty state; consequently computing the second estimated fault indicator value $(K_H)_{EST2}$. The difference D_2 between $(K_H)_{EST2}$ and $(K_F)_{EXPT}$ serves as an indication of the fault. The higher the value of D_2, the greater is the distinction between the experimental faulty state and its corresponding healthy estimate. The two difference terms D_1 and D_2 are shown explicitly in (5.4) and (5.5) respectively. As long as D_2 is higher than D_1, the inter-turn winding fault gets reliably detected.

$$D_1 = (K_H)_{EST1} - (K_H)_{EXPT} \tag{5.4}$$

$$D_2 = (K_H)_{EST2} - (K_F)_{EXPT} \tag{5.5}$$

Following the procedure mentioned above, the fault detection scheme has been implemented in six practical test conditions involving single-turn faults on secondary and primary sides under different types and levels of load. For each test condition, a table has been provided showing the corresponding values of $(K_H)_{EXPT}$, $(K_F)_{EXPT}$, $(K_H)_{EST1}$ and $(K_H)_{EST2}$. Also the values of D_1 and D_2 have been computed for each case using (5.4) and (5.5) respectively; and they have been also plotted for comparison.

Case 1 – Single-turn fault on secondary side under R type full-load

Datasets	Experimental values		Estimated values	
	$(K_H)_{EXPT}$	$(K_F)_{EXPT}$	$(K_H)_{EST1}$	$(K_H)_{EST2}$
1	10.69656	10.11898	10.62109	10.53053
2	11.56938	11.22961	11.36924	11.57943
3	11.35805	10.66839	11.25596	10.93811
4	11.22336	10.58828	10.97657	10.78507
5	10.25223	9.80190	10.30291	10.36733

Table 5.6 Comparison of experimental and estimated fault indicator values for fault detection in Case 1

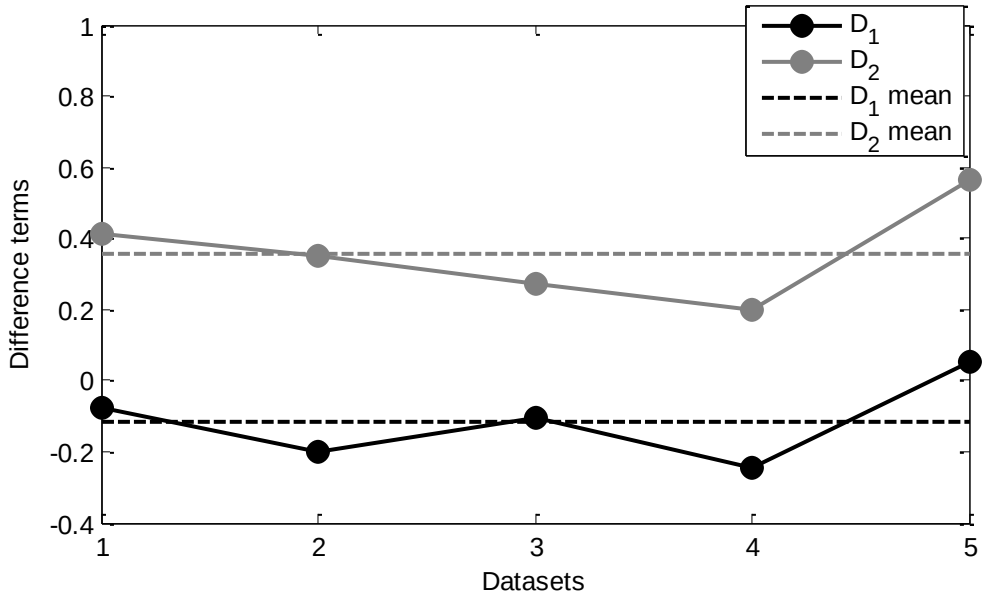

Figure 5.7 Comparison of difference terms for fault detection in Case 1 (Mean of D_1: -0.11476, Standard deviation of D_1: 0.11597; Mean of D_2: 0.35866, Standard deviation of D_2: 0.14119)

Case 2 – Single-turn fault on secondary side under RL type 50 % load

Datasets	Experimental values		Estimated values	
	$(K_H)_{EXPT}$	$(K_F)_{EXPT}$	$(K_H)_{EST1}$	$(K_H)_{EST2}$
1	11.79727	11.19288	11.81106	11.67843
2	12.37037	11.81009	12.32137	12.22465
3	11.93130	11.68201	11.91458	12.01040
4	11.60160	11.12657	11.42026	11.35858
5	12.06278	11.73013	12.08415	12.01173

Table 5.7 Comparison of experimental and estimated fault indicator values for fault detection in Case 2

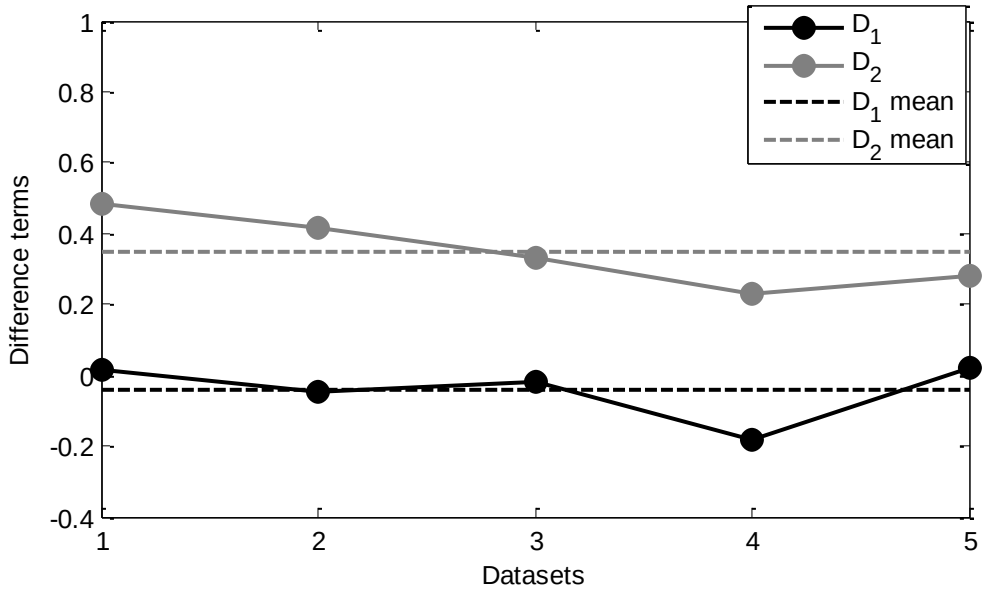

Figure 5.8 Comparison of difference terms for fault detection in Case 4 (Mean of D_1: -0.04238, Standard deviation of D_1: 0.08251; Mean of D_2: 0.34842, Standard deviation of D_2: 0.10198)

Case 3 – Single-turn fault on secondary side under RC type 25 % load

Datasets	Experimental values		Estimated values	
	$(K_H)_{EXPT}$	$(K_F)_{EXPT}$	$(K_H)_{EST1}$	$(K_H)_{EST2}$
1	9.96807	9.48931	9.96001	9.96460
2	10.04022	9.69374	10.10906	10.08316
3	10.27901	9.77393	10.26442	10.26403
4	10.02973	9.54650	10.19542	10.15980
5	10.23018	9.71785	10.22120	10.17994

Table 5.8 Comparison of experimental and estimated fault indicator values for fault detection in Case 3

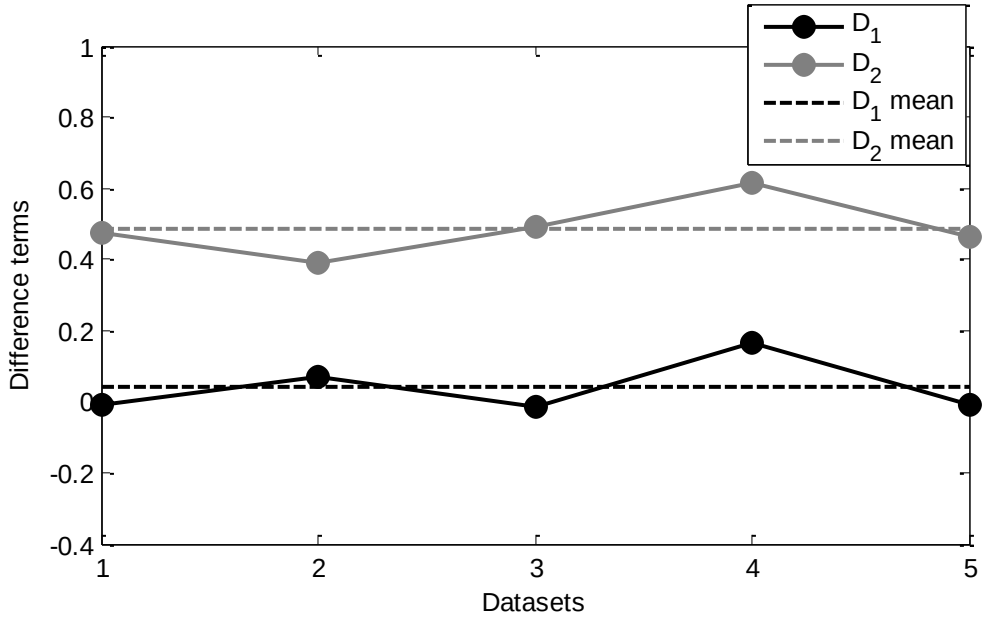

Figure 5.9 Comparison of difference terms for fault detection in Case 3 (Mean of D_1: 0.04058, Standard deviation of D_1: 0.07803; Mean of D_2: 0.48604, Standard deviation of D_2: 0.08099)

Case 4 – Single-turn fault on secondary side under no-load

Datasets	Experimental values		Estimated values	
	$(K_H)_{EXPT}$	$(K_F)_{EXPT}$	$(K_H)_{EST1}$	$(K_H)_{EST2}$
1	10.11835	10.05995	9.96270	10.18319
2	10.39132	10.13555	10.37102	10.41898
3	10.58942	10.23263	10.78401	10.69259
4	10.95718	10.26869	11.02859	10.81299
5	10.40011	10.19930	10.23891	10.38130

Table 5.9 Comparison of experimental and estimated fault indicator values for fault detection in Case 4

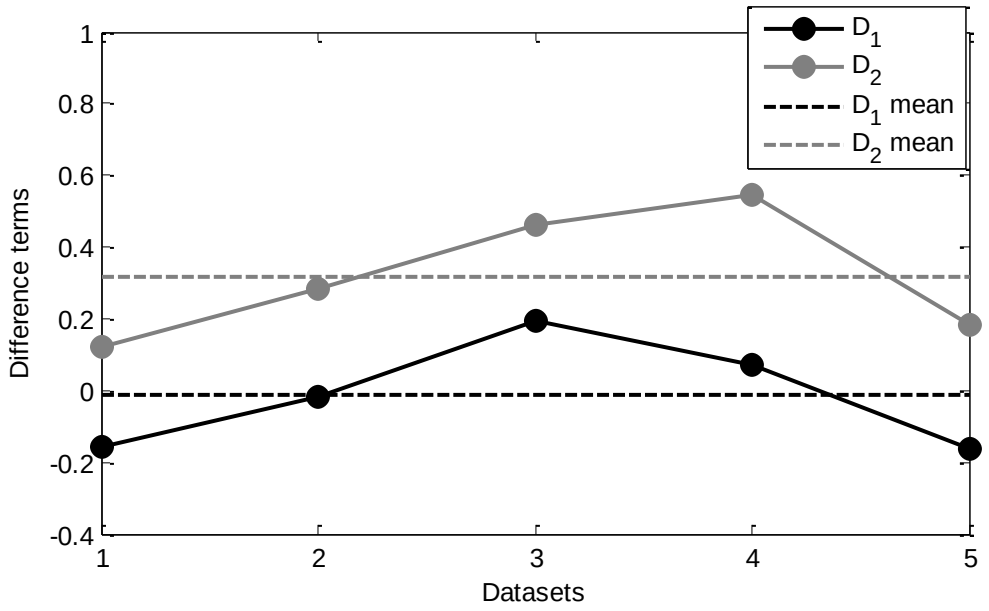

Figure 5.10 Comparison of difference terms for fault detection in Case 4 (Mean of D_1: -0.01423, Standard deviation of D_1: 0.15213; Mean of D_2: 0.31859, Standard deviation of D_2: 0.17957)

Case 5 – Single-turn fault on primary side under no-load

Datasets	Experimental values		Estimated values	
	$(K_H)_{EXPT}$	$(K_F)_{EXPT}$	$(K_H)_{EST1}$	$(K_H)_{EST2}$
1	10.10541	9.66080	10.00608	10.20801
2	10.42873	9.65885	10.33828	10.20696
3	10.16446	9.60150	10.18330	10.09189
4	10.17170	9.49187	10.18143	10.08751
5	10.20100	9.74689	10.08285	10.20188

Table 5.10 Comparison of experimental and estimated fault indicator values for fault detection in Case 5

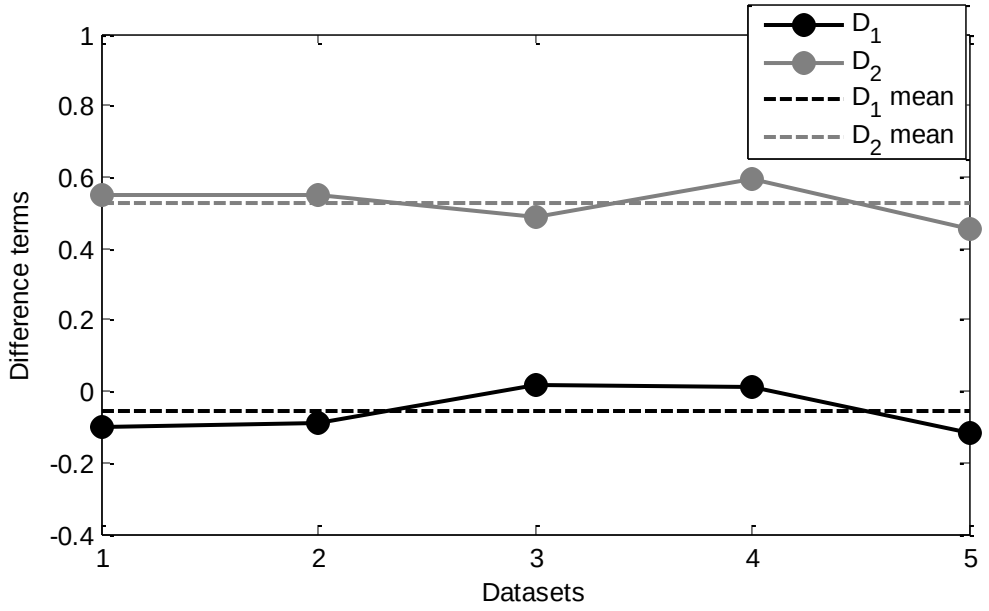

Figure 5.11 Comparison of difference terms for fault detection in Case 5 (Mean of D_1: -0.05587, Standard deviation of D_1: 0.06490; Mean of D_2: 0.52727, Standard deviation of D_2: 0.05498)

Case 6 – Single-turn fault on secondary side under rectifier-connected load

For conducting this test, a full-bridge uncontrolled rectifier was connected to the secondary side of the single-phase transformer followed by a filter capacitor in parallel for smoothing out the

rectified DC output; ultimately supplying power to an R-type load. The load resistance was so selected that the RMS value of the transformer current under healthy condition was close to the rated current. Even while the transformer supplies power to such rectifier loads, the modified fault detection scheme works effectively, as evident from Table 5.11 and Figure 5.12.

Datasets	**Experimental values**		**Estimated values**	
	$(K_H)_{EXPT}$	$(K_F)_{EXPT}$	$(K_H)_{EST1}$	$(K_H)_{EST2}$
1	10.53952	10.31645	10.73448	10.73963
2	10.43080	10.17610	10.41249	10.43136
3	10.47762	9.90655	10.60000	10.56774
4	10.38656	9.99455	10.49071	10.52610
5	10.74444	10.29755	10.63950	10.66318

Table 5.11 Comparison of experimental and estimated fault indicator values for fault detection in Case 6

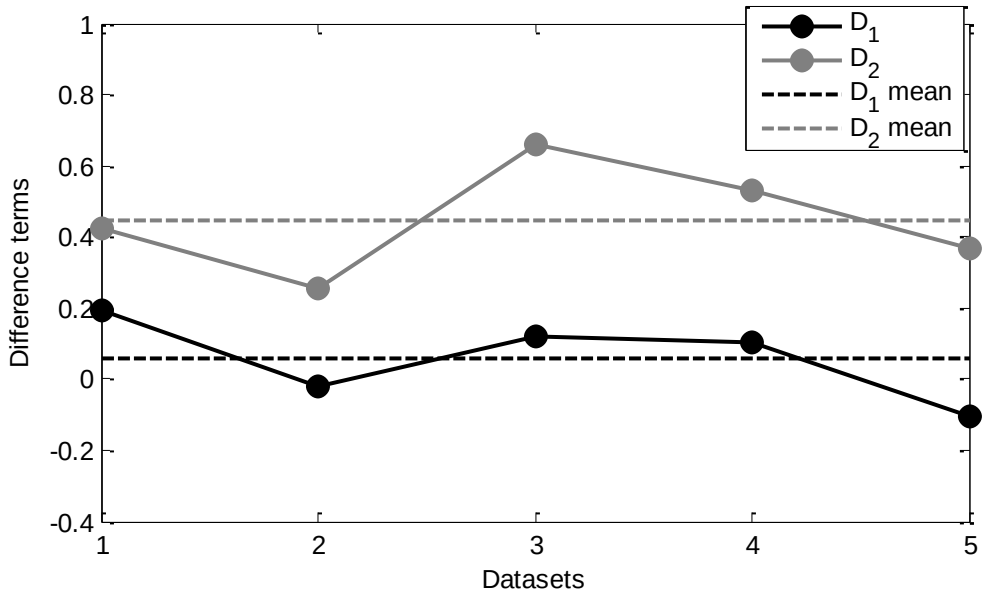

Figure 5.12 Comparison of difference terms for fault detection in Case 6 (Mean of D_1: 0.05965, Standard deviation of D_1: 0.11978; Mean of D_2: 0.44736, Standard deviation of D_2: 0.15571)

5.2.1 Determination of tripping threshold

After computation of the mean and standard deviation values of D_1 and D_2 for all the six test conditions, their confidence intervals (corresponding to 0.975 percentile) have been determined assuming normal distribution. Equation (5.6) shows the statistical formulae used for computing the upper limit (UL) and lower limit (LL) of the 0.975 confidence interval (CI), where $\bar{x}$, σ and m represents the mean, standard deviation and number of samples corresponding to a particular set of D_1 or D_2 values. Also, $z_{0.975}$ represents the value of the 0.975 percentile of standard normal density and it is equal to 1.967 [82]. The 0.975 confidence interval refers to the interval within which 97.5 % of the values in a particular set of D_1 or D_2 are present. Table 5.12 shows the confidence intervals for the D_1 and D_2 values corresponding to the six test conditions.

$$(Limits)_{0.975\,CI} = \bar{x} \pm \left[z_{0.975} \left(\sigma / \sqrt{m} \right) \right] \tag{5.6}$$

Cases	$(\boldsymbol{D_1})_{\mathbf{0.975\,CI}}$	$(\boldsymbol{D_2})_{\mathbf{0.975\,CI}}$	**UL of** $(\boldsymbol{D_1})_{\mathbf{0.975\,CI}}$	**LL of** $(\boldsymbol{D_2})_{\mathbf{0.975\,CI}}$
1	-0.11476 ± 0.10201	0.35866 ± 0.12420	-0.01275	0.23446
2	-0.04238 ± 0.07258	0.34842 ± 0.08971	0.03020	0.25871
3	0.04058 ± 0.06864	0.48604 ± 0.07124	0.10922	0.41480
4	-0.01423 ± 0.13382	0.31859 ± 0.15796	0.11959	0.16063
5	-0.05587 ± 0.05709	0.52727 ± 0.04836	0.00122	0.47891
6	0.05965 ± 0.10537	0.44736 ± 0.13697	0.16502	0.31039

Table 5.12 Confidence intervals (corresponding to 0.975 percentile) for the difference terms

Table 5.12 also shows the upper limits of the confidence interval for D_1 (column 4) and lower limits of the confidence interval for D_2 (column 5) corresponding to all the six test cases. The

mean and standard deviation of the values in Column 4 are 0.06870 and 0.07240 respectively, while the mean and standard deviation of the values in Column 5 are 0.30960 and 0.11850 respectively. Applying (5.6) again to column 4 and column 5 of Table 5.12 gives 0.12680 and 0.21440 as the upper limit (UL) for column 4 and lower limit (LL) for column 5 respectively. The mean of 0.12680 and 0.21440, which is equal to 0.17060, can be taken as a threshold level for tripping. Such a threshold level will make the fault detection very robust minimizing false negatives and positives. Considering more test cases and higher number of datasets for each test case will further fine tune this threshold level.

5.3 Discussion of results and feasibility for industrial implementation

Several important challenges which need to be met before implementing any transformer fault diagnostic system in industry are:

- Repeatability and reliability
- Response time
- Cost of installation, implementation and maintenance
- Unambiguity

For each test condition, five datasets have been considered to demonstrate the repeatability of the fault detection scheme. Based on the results presented in section 5.2, the modified fault detection scheme is found to reliably detect single-turn short circuit faults on primary and secondary windings under different load conditions, even in case of rectifier loads. The values of D_1 are consistently higher than that of D_2 for all the test conditions; and this indicates the presence of inter-turn winding faults as previously mentioned. Thus, the mean values of D_1 and D_2 computed over a few *health monitoring cycles* can be compared to detect the fault. As evident from Table 5.12 the maximum confidence intervals of the difference terms for fault detection were found to occur in Case 4 (Single-turn fault on secondary side under no-load); while the minimum confidence intervals were found to occur in Case 5 (Single-turn fault on primary side under no-load). Also, the confidence intervals for D_1 and D_2 for all the test conditions never overlap one another i.e. the upper limit of D_1 interval is never higher than the lower limit of D_2 interval. The lower sensitivity of detecting single-turn faults is due to the fact that the shorting lead impedance

reduces the short-circuit current drastically when a single turn is shorted. This was verified by measuring the short-circuit current for different number of turns shorted as shown in Figure 5.13. In an actual fault situation, the short-circuit current for a single-turn fault will be more and hence, sensitivity will be more as well.

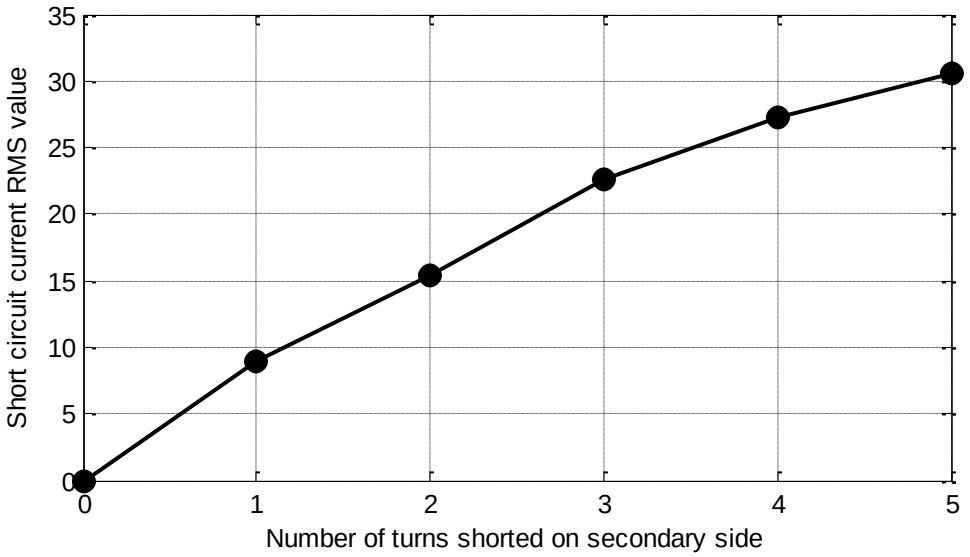

Figure 5.13 RMS value of short circuit current with respect to number of turns shorted

Additionally, the use of only the healthy no-load transformer model for the fault detection greatly decreases the simulation program's execution time, hence improving the response time of the scheme. Finally, it is necessary to mention that with minimum hardware, computational power and memory requirements, the proposed fault detection scheme involves low installation and implementation costs. Thus, it is definitely feasible to implement the proposed scheme practically in industrial settings. In the next chapter, the relevant conclusions and contributions of this thesis work has been outlined in view of the proposed scheme, followed by some recommendations for its improvement under future scope.

Chapter 6

Conclusion and Future Scope

6.1 Conclusion

In this work, the condition monitoring of single-phase transformers is addressed for inter-turn winding short-circuit faults. These faults often start from an incipient stage such as a single-turn fault and quickly manifest themselves into more severe faults involving a larger number of turns, ultimately leading to catastrophic consequences. Thus, in this work an emphasis has been given on the detection of these faults at the incipient stages.

A terminal voltage and current measurement based approach to model single-phase transformers has been proposed in order to simulate the performance of the transformers using a coupled inductive circuit model. The effects of transformer core saturation, non-linearity, hysteresis are incorporated in the model by considering a time-varying magnetizing inductance comprising of any desired number of harmonic components. The model is found to replicate the behaviour of the single-phase transformer with an extremely high level of accuracy, under any load conditions for healthy as well as faulty operations.

For practical implementation of the fault detection scheme, the experimentally acquired primary line voltage is fed to the healthy transformer model in order to compute an estimated value of the fault indicator. Simultaneously, from the experimental voltage and currents, the actual value of the fault indicator is determined. Comparison between the estimated and actual fault indicator values provides a good indication of the presence of an inter-turn winding fault. Detailed simulation and experiment based studies have been performed for corroborating the effectiveness of the proposed terminal measurement based modeling technique not only in detecting incipient stages of inter-turn winding faults (involving less than 1% of the turns) but also in estimating fault severity.

6.2 Contributions

The important contributions of this thesis work can be outlined as follows:

- A new methodology for modeling single-phase transformers has been proposed, which is solely based on the terminal measurements of voltage and currents. The technique is unambiguous, computationally simple and involves minimum hardware and memory requirements.

- Detailed simulation and experimental results have been presented for studying the behaviour of single-phase transformers under healthy and faulty states using the terminal measurement based modeling technique.

- A novel inter-turn winding fault detection technique has been proposed, which is primarily based on the changes in the harmonic components of the exciting current and primary line voltage under the influence of inter-turn faults. The effectiveness of the technique is largely dependent on the simulation of the transformers under healthy state using the terminal measurement based model.

- Finally, through several examples the technique has been practically implemented for reliably detecting single-turn short circuit faults under various operating conditions.

6.3 Future Scope

On-line diagnosis has the potential to become an integral part of any transformer protection system. Selection of such a diagnostic method depends on essential factors such as cost, unambiguity, response time, reliability and sensitivity. The proposed fault detection technique shows good promise to meet all the above requirements. Currently, more research is going on for

extending the proposed inter-turn winding fault detection scheme in three-phase transformers. Following are some of the ways for improving the performance of the technique:

- The terminal measurement based transformer modeling technique, which involves computation of the coefficients of magnetizing inductance from the flux linkage and magnetizing current, is central to the proposed inter-turn fault detection scheme. With the passage of time, the core-loss resistance, winding resistance and leakage inductance of single-phase transformers change due to core degradation, loosening of laminations etc; and such changes can affect the accuracy of the simulation model consequently reducing the effectiveness of the fault detecting scheme. Thus, computing these coefficients while performing scheduled maintenance on the transformers will help to overcome this problem.

- For large-scale implementation of the fault detection technique especially in industrial settings, a two-level threshold comprising of the fault indicator values for healthy and faulty states under different operating conditions is necessary for easy and quick detection of faults at their incipient stages. The two threshold levels can be determined as follows:
  - **First threshold level:** A warning signal can be generated when the difference between the estimated and experimental fault indicator values reach this point; thereby indicating the possibility of a fault.

  - **Second threshold level:** A trip signal can be generated for operating the circuit breaker to isolate the transformer, when the difference between the estimated and experimental fault indicator values reach this point; thereby confirming the presence of a fault.

  This will prevent nuisance trips arising out of false positives and high impedance faults. If fault currents are below a certain threshold, it will not propagate to immediate catastrophic failures. Thus, a warning is sufficient to alert the person(s) in charge of the maintenance of the transformer.

List of references

1. Homepage for EE/Econ 458 – Economic Systems for Electric Power Planning, Iowa State University, USA, http://www2.econ.iastate.edu/classes/econ458/tesfatsion/Home458team.htm

2. W. H. Bartley, "Analysis of transformer failures," *36th Annual Conference of the International Association of Engineering Insurers*, 2003

3. Power Systems Relay Committee of the IEEE Power Engineering Society, "IEEE Guide for Protective Relay Applications to Power Transformers," 8 March, 2000

4. L. M. R. Oliveira; A. J. M. Cardoso, "On-line diagnostics of transformer winding insulation failures, by Park's Vector Approach," *Proceedings of the 9th International Electrical Insulation Conference*, pp. 16-21, 18-20 June, 2002

5. K. L. Butler-Purry; A. Kuforiji, "Experimental results from short-circuit faults on a distribution transformer*," IEEE Transmission and Distribution Conference and Exposition*, vol. 1, pp. 299-306, 2001

6. K. L. Butler-Purry; M. Bagriyanik; M. J. Mousavi; P. Palmer-Buckle, "Experimental investigation of internal short circuit faults leading to advanced incipient behavior and failure of a distribution transformer," *IEEE Power Systems Conference and Exposition*, vol. 3, pp. 1407-1416, 10-13 October, 2004

7. V. Behjat; A. Vahedi, "An experimental approach for investigating low-level interturn winding faults in power transformers," *Electrical Engineering*, 2012

8. B. Ravindranath; M. Chander, "Power Systems Protection and Switchgear," New Age International (P) Limited, 1977

9. Y. G. Paithankar; S. R. Bhide, "Fundamentals of Power System Protection," PHI Learning Pvt. Ltd., 2004

10. A. Vahedi; V. Behjat, "Online monitoring of power transformers for detection of internal winding short circuit faults using negative sequence analysis," *European Transactions on Electrical Power*, vol. 21, issue 1, pp. 196-211, January, 2011

11. S. V. Kulkarni; S. A. Kharpade, "Transformer Engineering: Design, Technology and Diagnostics," CRC Press, 2012

12. M. J. Heathcote, "The J&P Transformer Book," Elsevier Ltd., 11th edition ,2007

13. R. S. Bhide; M. S. S. Srinivas; A. Banerjee; R. Somakumar, "Analysis of winding inter-turn fault in transformer: A review and transformer models," *IEEE International Conference on Sustainable Energy Technologies*, pp. 1-7, 6-9 December, 2010

14. N. C. Joshi; Y. R. Sood; R. K. Jarial; R. Thapliyal, "Transformer internal winding faults diagnosis methods: A review," *MIT International Journal of Electrical and Instrumentation Engineering*, vol. 2, issue 2, pp. 77-81, August, 2012

15. J. H. McWhirter; T. R. Specht; W. D. Albright, "Effect of impulse testing on transformer iron loss," *Transactions of the American Institute of Electrical Engineers – Part III: Power Apparatus and Systems*, vol. 75, issue 3, pp. 1275-1279, January, 1956

16. S. Nandi, "A novel frequency domain based technique to detect transformer inter-turn faults," *IEEE International Electric Machines and Drives Conference*, vol. 1, pp. 569-574, 3-5 May, 2007

17. L. M. R. Oliveira; A. J. M. Cardoso; S. M. A. Cruz, "Transformers On-load exciting current Park's Vector Approach as a tool for winding fault diagnostics," *15th International Conference on Electrical Machines*, 25-28 August, 2002

18. L. M. R. Oliveira; A. J. M. Cardoso, "A permeance based transformer model and its application to winding interturn arcing fault studies," *IEEE Transactions on Power Delivery*, vol. 25, issue 3, pp. 1589-1598, July, 2010

19. P. Sridhar; B. P. Singh; P. V. K. Rao, "Neutral current wave-shape analysis using wavelet for diagnosis of winding insulation of a transformer," *Turkish Journal of Electrical Engineering and Computer Science*, vol. 20, issue 6, 2012

20. A. Bhoomaiah; P. K. Reddy; K. S. L. Murthy; P. A. Naidu; B. Singh, "Measurement of neutral currents in a power transformer and fault detection using wavelet techniques," *Annual Report Conference on Electrical Insulation and Dielectric Phenomena*, pp. 170-173, 17-20 October, 2004

21. H. Monsef; S. Lotfifard, "A new Wavelet-based Approach for internal fault current identification in power transformers," *Scientia Iranica*, vol. 15, issue 2, pp. 160-169, April, 2008

22. M. Faridi; E. Rahimpour; M. Kharezi; H. R. Mirzaei; A. Akbari, "Localization of turn-to-turn fault in transformers using Artificial Neural Networks and winding transfer function," *10th IEEE International Conference on Solid Dielectrics*, pp. 1-4, 4-9 July, 2010

23. H. Firoozi; M. Kharezi; H. Bakhshi, "Turn-to-turn fault localization of power transformers using neural network techniques," *IEEE 9th International Conference on the Properties and Applications of Dielectric Materials*, pp. 249-252, 19-23 July, 2009

24. F. Zakaria; D. Johari; I. Musirin, "Artificial neural network (ANN) application in dissolved gas analysis (DGA) methods for the detection of incipient faults in oil-filled power transformers," *IEEE International Conference on Control Systems, Computing and Engineering*, pp. 328-332, 23-25 November, 2012

25. S. Wei; G. Wang; M. Guan; Y. Su; R. Zhao, "Power Transformer on-line detection and fault diagnosis system based on neural network and embedded internet," *Proceedings of the Sixth International Conference of Information Fusion*, vol. 1, pp. 372-378, 8-11 July, 2003

26. Y. C. Huang, "Power transformer fault detection using intelligent neural networks," *IEEE Region 10 Conference on Computers, Communications, Control and Power Engineering*, vol. 3, pp. 1761-1764, 28-31 October, 2002

27. E. P. Dick; C. C. Erven, “Transformer diagnostic testing by frequency response analysis,” *IEEE Transactions on Power Apparatus and Systems*, vol. PAS-97, issue 6, pp. 2144-2153, November, 1978

28. M. Vikash; K. Sharlinprija; M. K. Ilampoornan, “Transformer fault detection by frequency response analysis,” *International Journal of Computer Science and Electrical Engineering*, vol. 1, issue 2, 2012

29. A. Wilk; D. Adamcyzk, “Investigations on the sensitivity of FRA method in diagnosis of interturn faults in transformer winding,” *IEEE International Symposium on Industrial Electronics*, pp. 631-636, 27-30 June, 2011

30. G. D. Gonzales; J. G. A. Fernandez; P. A. Arboleya, “Diagnosis of a turn-to-turn short circuit in power transformers by means of zero sequence current analysis,” *Electric Power Systems Research*, vol. 69, issue 2, pp. 321-329, May, 2004

31. A. H. Almasoud, “Differential voltage relay for inter-turn winding protection,” *Umm Al-Qura University Journal of Science - Medicine - Engineering*, vol. 15, issue 1, pp. 13-19, 2003

32. M. F. Cabanas; F. P. Gonzales; M. G. Melero; C. H. Rojas; G. A. Orcajo; J. M. Cano; J. G. Norniella, “Insulation fault diagnosis in high voltage power transformers by means of leakage flux analysis,” *Progress in Electromagnetic Research*, vol. 114, pp. 211-234, 2011

33. M. F. Cabanas; M. G. Melero; C. H. Rojas; G. A. Orcajo; J. M. Cano; F. P. Gonzales; J. G. Norniella; S. D. Rozada, “Detection of insulation faults on disc-type winding transformers by means of leakage flux analysis,” *IEEE International Symposium on Diagnostics for Electric Machines, Power Electronics and Drives*, pp. 1-6, 31 August – 3 September, 2009

34. Y. C. Kang; B. E. Lee; S. H. Kang; P. A. Crossley, “Transformer protection based on the increment of flux linkages,” *IEE Proceedings – Generation, Transmission and Distribution*, vol. 151, issue 4, pp. 548-554, 11 July, 2004

35. Y. C. Kang; B. E. Lee; T. Y. Zheng; Y. H. Kim; P. A. Crossley, "Protection, faulted phase and winding identification for the three-winding transformer using the increments of flux linkages," *IET Generation, Transmission and Distribution*, vol. 4, issue 9, pp. 1060-1068, September, 2010

36. A. Abu-Siada; S. Islam, "A novel online technique to detect power transformer winding faults," *IEEE Transactions on Power Delivery*, vol. 27, issue 2, pp. 849-857, April, 2012

37. A. Wiszniewski; W. Rebizant; L. Schiei, "New algorithms for power transformer inter-turns fault protection," *Electric Power Systems Research*, vol. 79, issue 10, pp. 1454-1461, October, 2009

38. R. R. Desai; A. N. Patel; V. R. Gupta, "Identification of various internal faults of transformer based on no-load current analysis," *International Journal of Emerging Technology and Advanced Engineering*, vol. 2, issue 2, February, 2012

39. I. Daut; S. Hasan; S. Taib; R. Chan; M. Irwanto, "Harmonic content as the indicator of transformer core saturation," *4th International Power Engineering and Optimization Conference*, pp. 382-385, 23-24 June, 2010

40. J. A. Martinez; B. A. Mork, "Transformer modeling for low- and mid-frequency transients – a review," *IEEE Transactions on Power Delivery*, vol. 20, issue 2, pp. 1625-1632, April, 2005

41. S. Javadi; B. Vahidi; S. H. Hosseinian, "Three phase transformer modeling with consideration the core effects," *International Conference on Electrical Machines and Systems*, pp. 4375-4378, 17-30 October, 2008

42. P. Bastard; P. Bertrand; M. Meunier, "A transformer model for winding fault studies," *IEEE Transactions on Power Delivery*, vol. 9, issue 2, pp. 690-699, April, 1994

43. F. De Leon; A. Semlyen, "Complete transformer model for electromagnetic transients," *IEEE Transactions on Power Delivery*, vol. 9, issue 1, pp. 231-239, January, 1994

44. N. D. Hatziargyriou; J. M. Prousalidis; B. C. Papadias, "Generalised transformer model based on the analysis of its magnetic core circuit," *IEE Proceedings on Generation, Transmission and Distribution*, vol. 140, issue 4, pp. 269-278, July, 1993

45. X. S. Chen; P. Neudorfer, "Digital model for transient studies of a three-phase five-legged transformer," *IEE Proceedings on Generation, Transmission and Distribution*, vol. 139, issue 4, pp. 351-358, July, 1992

46. H. B. Elrefaie; A. I. Megahed, "Modeling transformer internal faults using Matlab," *11th Mediterranean Electrotechnical Conference*, pp. 226-230, 2002

47. A. F. Witulski, "Introduction to modeling of transformers and coupled inductors," *IEEE Transactions on Power Electronics*, vol. 10, issue 3, pp. 349-357, May, 1995

48. R. Yacamini; H. Bronzeado, "Transformer inrush calculations using a coupled electromagnetic model," *IEE Proceedings on Science, Measurement and Technology*, vol. 141, issue 6, pp. 491-498, November, 1994

49. E. F. Fuchs; Y. You; D. J. Roesler, "Modeling and simulation, and their validation of three-phase transformers with three legs under DC bias," *IEEE Transactions on Power Delivery*, vol. 14, issue 2, pp. 443-449, April, 1999

50. D. W. P. Thomas; J. Paul; O. Ozgonenel; C. Christopoulos, "Time domain simulation of nonlinear transformers displaying hysteresis," *IEEE Transactions on Magnetics*, vol. 42, issue 7, pp. 1820-1827, July, 2006

51. R. Allcock; R. McClelland; S. A. Holland; A. Roue, "Transformer design and analysis using finite element methods," *IEE Colloquium on Computation in Electrostatics*, pp. 8/1-8/3, 26 January, 1995

52. O. A. Mohammed; Z. Liu; S. Liu; N. Y. Abed, "Finite-element-based nonlinear physical model of iron-core transformers for dynamic simulations," *IEEE Transactions on Magnetics*, vol. 42, issue 4, pp. 1027-1030, April, 2006

53. A. F. Hoke; C. R. Sullivan, "An improved two-dimensional numerical modeling method for E-core transformers," *17th Annual IEEE Applied Power Electronics Conference and Exposition*, vol. 1, pp. 151-157, 2002

54. M. Khelil; M. Elleuch, "Finite Element Method analysis of three phase transformer core accounting for anisotropy and air gaps," *7th International Multi-Conference on Systems, Signals and Devices*, pp. 1-6, 27-30 June, 2010

55. C. C. Adalja; M. L. Jain, "Analysis of stray losses in power transformers by 3D magnetic field simulation," *15th National Power Systems Conference - India*, December, 2008

56. L. Susnjic; Z. Haznadar; Z. Valkovic, "Stray losses computation in power transformer," *12th Biennial IEEE Conference on Electromagnetic Field Computation*, pp. 490, 30 April-3 May, 2006

57. L. Kralj; D. Miljavec, "Stray losses in power transformer tank walls and construction parts," *19th International Conference on Electrical Machines*, pp. 1-4, 6-8 September, 2010

58. M. V. F. da Luz; J. V. Leite; A. Benabou; N. Sadowski, "Three-phase transformer modeling using a vector hysteresis model and including the eddy current and the anomalous losses," *IEEE Transactions on Magnetics*, vol. 46, issue 8, pp. 3201-3204, August, 2010

59. T. H. Fawzi; A. A. Elkhalek, "New approaches for the applications of FEM in the routine design of power transformers using PC's," *18th International Conference and Exhibition on Electricity Distribution*, pp. 1-5, 6-9 June, 2005

60. R. Mayuri; N. R. Sinnou; K. Ilango, "Eddy current loss modelling in transformer iron losses operated by PWM inverter," *Joint International Conference on Power Electronics, Drives and Energy Systems (PEDES) & Power India*, pp. 1-5, 20-23 December, 2010

61. E. Schmidt; P. Hamberger; W. Seitlinger, "Finite element calculation of eddy current losses in the tank wall of power transformers," *IEEE International Electric Machines and Drives Conference*, vol. 2, pp. 1167-1173, 1-4 June, 2003

62. A. Damnjanovic; A. Islam; A. Domijan, "Harmonic domain modeling of transformer nonlinear characteristic with piece-wise approximation," *14th International Conference on Harmonics and Quality of Power*, pp. 1-6, 26-29 September, 2010

63. J. D. Greene; C. A. Gross, "Nonlinear modeling of transformers," *IEEE Transactions on Industry Applications*, vol. 24, issue 3, pp. 434-438, May/June, 1988

64. J. C. Moreira, T. A. Lipo, "Modeling of saturated AC machines including air gap flux harmonic components," *IEEE Transactions on Industry Applications*, vol. 28, issue 2, pp. 343-349, March/April, 1992

65. DAQPad – 6020E, 16/8 Inputs, 100 kS/s, 12-bit multifunction I/O; National Instruments Corp., Vaudreuil-Dorion, Quebec, Canada

66. MATLAB R2012a, The Mathworks Ltd, Ntaick, MA, USA

67. M. G. Say, "The performance and design of alternating current machines," CBS Publishers and Distributors, 3rd edition, New Delhi, 2002

68. D. Murthy-Bellur; N. Kondrath; M. K. Kazimierczuk, "Transformer winding loss caused by skin and proximity effects including harmonics in pulse-width modulated DC-DC flyback converters for the continuous conduction mode," *IET Power Electronics*, vol. 4, issue 4, pp. 363-373, April, 2011

69. S. C. Wang; G. W. Huang; S. D. Wu; K. M. Chen, "Temperature effects on the performance of 4-port transformers," *International Semiconductor Device Research Symposium*, pp. 190-191, 10-12 December, 2003

70. S. Bhowmick; S. Nandi, "Terminal measurement based modeling of single phase transformer for condition monitoring," *20th International Conference on Electric Machines*, pp. 1854-1859, 2-5 September, 2012

71. Datasheet for single-phase transformer, Hammond Power Solutions, Guelph, Ontario, Canada

72. Filtfilt – Zero phase digital filtering, MATLAB R2013a Documentation, The MathWorks Ltd. (http://www.mathworks.com/help/signal/ref/filtfilt.html)

73. V. Behjat; A. Vahedi, "Numerical modeling of transformers interturn faults and characterising the faulty transformer behaviour under various faults and operating conditions," *IET Electric Power Applications*, vol. 5, issue 5, pp. 415-431, May, 2011

74. F. Zhalefar; M. Sanaye-Pasand, "Studying effect of location and resistance of inter-turn faults on fault current in power transformers," *42nd International Universities Power Engineering Conference*, pp. 138-142, 4-6 September, 2007

75. Power Fist Infrared Digital Thermometer, Model no. 8223570

76. "IEEE Standard Test Code for Dry-Type Distribution and Power Transformers," *IEEE Power Engineering Society*, 1979

77. "IEEE Standard Test Code for Liquid-Immersed Distribution, Power, and Regulating Transformers," *IEEE Power & Energy Society*, October, 2010

78. Intermatic Digital Auto Turn-Off Timer, Model EI 400 Series (www.intermatic.com)

79. NI PXIe – 1062Q 8 Slot, 3U PXI Express Chassis with AC-Up to 3 GB/s hardware platform; National Instruments Corp., Vaudreuil-Dorion, Quebec, Canada

80. "Using NI Hardware and Software to Build Real-Time High Performance Computing (RTHPC) Systems," National Instruments Corp., Vaudreuil-Dorion, Quebec, Canada, 3 February, 2012 (http://www.ni.com/white-paper/12435/en/)

81. "Going Parallel with LabVIEW Delivers Test Throughput Gains," National Instruments Corp., Vaudreuil-Dorion, Quebec, Canada, 13 February, 2012 (http://www.ni.com/white-paper/7424/en/)

82. A. Papoulis; S. Unnikrishna Pillai, "Probability, Random Variables and Stochastic Processes," McGraw-Hill, 4th edition, 2002

Appendix – A: Equivalent circuit parameters of single-phase transformer

The equivalent circuit parameters of the single-phase 150VA, 120/120V (RMS), shell-type transformers, as obtained from the open-circuit and short-circuit test results and considering 60Hz as the fundamental frequency, are given in Table A.1.

Equivalent parameters	**Value**
Core-loss resistance R_C	3356.56 Ω
Magnetizing reactance X_M	513.59 Ω
Equivalent winding resistance R_{EQ}	4.72 Ω
Equivalent leakage reactance $X_{l_{EQ}}$	2.53 Ω

Table A.1 Equivalent circuit parameters of single-phase transformer